DESIGN AND DEVELOPMENT OF VARIABLE PITCH QUADCOPTER FOR LONG ENDURANCE FLIGHT

By

XIAONAN WU

Bachelor of Science in Mechanical and Aerospace Engineering

Oklahoma State University

Stillwater, OK

2018

Submitted to the Faculty of the
Graduate College of the
Oklahoma State University
in partial fulfillment of
the requirements for
the Degree of
MASTER OF SCIENCE
May, 2018

DESIGN AND DEVELOPMENT OF VARIABLE PITCH
QUADCOPTER FOR LONG ENDURANCE FLIGHT

Thesis Approved:

Dr. Jamey Jacob

Thesis Adviser

Dr. Ronald D. Delahoussaye

Dr. James Kidd

Name: Xiaonan Wu

Date of Degree: MAY, 2018

Title of Study: DESIGN AND DEVELOPMENT OF VARIABLE PITCH
QUADROTOR FOR LONG ENDURANCE FLIGHT

Major Field: MECHANICAL AND AEROSPACE ENGINEERING

ABSTRACT:

The variable pitch quadrotor is not a new concept but has been largely ignored in small unmanned aircraft, unlike the fixed pitch quadcopter which is controlled only by changing the RPM of the motors and only has about 30 minutes of total flight time. The variable pitch quadrotor can be controlled either by the change of the motor RPM or rotor blade pitch angle or by the combination of both. This gives the variable pitch quadrotor potential advantages in payload, maneuverability and long endurance flight. This research is focused on the design methodology for a variable pitch quadrotor using a single motor with potential applications for a long endurance flight. This variable pitch quadcopter uses a single power plant to power all four rotors through a power transmission system. All four rotors have the same rpm but vary the blade pitch angle to control its attitude in the air. A proof of concept variable pitch quadcopter is developed for testing the drivetrain mechanism on the vehicle and evaluating performance of the vehicle through numbers of testing.

TABLE OF CONTENTS

Chapter Page

LIST OF TABLES

LIST OF FIGURES

Figure Page

Figure Page

Figure Page

CHAPTER I

INTRODUCTION

1.1 Motivation

In recent years, a growing interest has been observed in quadcopter unmanned aerial vehicles (UAVs). Civilians have found an interest in the capabilities of quadrotor UAVs in the fields of aerial photography and shipping small packages [1]. Research institutes have been conducting research with quadrotor UAVs on engineering topics such as UAV swarming, aerial mapping, and sense-and avoid [2]. Most quadcopters in the civilian market today are fixed pitch propellers and only have about 30 minutes of total flight endurance. This constraint greatly reduces the applications of the quadcopter.

A typical quadcopter controls its attitude by changing the thrust among the propellers. With a fixed pitch quadcopter, the propeller is directly mounted onto the electric motor. The thrust produced by each propeller directly depends on the rpm of the electric motor [4][3]. This has made the fixed pitch quadcopter very robust due to the simplistic design of having no moving parts beside the rotating motors and propellers. However, the simplicity of this design places fundamental limitations on the performance and the size of the vehicle [6].

To understand this limitation, first of all, one must consider the effects of scaling up the quadcopter system. As one increases the size of the system, the size of the propeller must likewise will also increase.

From the control's standpoint, controlling the rpm of this larger propeller becomes more difficult, because the electric motor cannot change the rpm quick enough to stabilize the vehicle.

A solution to this stability limitation can be a variable pitch quadcopter. Fig. 1.1 shows an example of a variable pitch quadcopter. The variable pitch quadcopter has one more degree of freedom compared to the fixed pitch quadrotor. It can be controlled by changing the rpm of the motor or blade pitch angle or the combination of both. Because of that, it can overcome the limitations of the fixed pitch quadrotor and has many advantages over the fixed pitch quadrotor such as long endurance flight as well as more payload and higher maneuverability.

Figure 1. 1: Example of a RC variable pitch quadcopter from HobbyKing.[10]

1.2 Goal and Objectives

The goal of this research project was to design and develop a gas-powered variable pitch quadrotor which would be capable of long-endurance flight. The main focus of this thesis paper is on designing the methodology applicable for building a variable pitch quadrotor. The challenge in the design of a long-endurance flight variable pitch quadrotor is utilizing a single electric motor to power all four rotors and a power transmission system to keep the rotors counter-rotating. The main objectives to be solved in this connection are the following ones:

- Determining the lift and torque that are created by the rotor and power consumption of the rotor
- Selecting the electrical motor that meets the power requirement of all four rotors
- Designing a power transmission system to distribute the power from single motor to four rotors
- Designing and analyzing structural components using lightweight materials
- Conducting tethered flight tests of the vehicle
- Testing the thrust of the vehicle at different blade pitch angles
- Conducting the endurance test of the power transmission system
- Analyzing performance of the vehicle.

1.3 Thesis Outline

Variable pitch quadrotor is currently a new subject in the UAS field. There are only a few groups of researchers and hobbyists [8] [7] that have successfully designed and developed a variable pitch quadrotor. However, none of those quadrotors have been proved for capability of conducting a long endurance flight. This research project is focused on the methodology of designing and developing a large-scale variable pitch quadrotor for long endurance flight purposes. The paper can be divided into 6 sections. Section 2 includes previous work and literature review which help to understand the basic dynamic of quadrotor and the difference between a variable pitch quadrotor and fixed pitch quadrotor. Section 3 discusses the initial system design considerations of the total system, such as the configuration design, variable pitch mechanism design, and power transmission system design. Section 4 provides calculations and analysis of the aerodynamics for the rotor blades, power transmission system, body frame, and landing gear. Section 5 describes the process of manufacturing and assembling different parts of the system, such as the fabrication of the carbon fiber drive shaft and landing gear. Section 6 develops a test procedure for the quadrotor and then discusses the results. This thesis finishes with conclusions and the ideas about possible directions of future work related to the subject of this project.

CHAPTER II

LITERATURE REVIEW AND PREVIOUS WORK

2.1 Overview of Quadcopter

The quadcopter gained more attention during the last decade. This is primarily due to the simplicity of its design, low cost and small size that make them safe to operate when located at a reasonable distance from people. Many small quadcopters have become very popular on the market, including DJI Phantom, Parrot AR Drone and 3DR Iris. These new quadcopters are cheap, lightweight, and use advanced electronics for performing flight control. These advantages provided a variety of applications for the quadcopter such as aerial photography, package delivery, search and rescue, precision agriculture, etc. [12]. A common quadcopter is a multirotor that consists of two pairs of propellers rotating in CW and CCW direction and providing the lift and control for the quadcopter in the air. The basic components of a quadcopter consist of a flight controller, four ESCs (electrical speed controllers), and four brushless electrical motors with fixed pitch propellers directly attached to the motor. Figure 2.1 shows an example of a common quadcopter. However, most of the quadcopters today can only have about 25 minutes of total flight time, which greatly reduces their range and endurance. This happens because they are powered by the battery packs. Batteries are heavy and have much lower energy density, compared to the gas-powered engine. This greatly reduces the practical applications of the quadcopter usage.

Figure 2. 1: Example of common quadcopter from DJI [13]

This is a very robust system because there is no mechanical control links and a swashplate between a propeller and motor, which makes it similar to a helicopter. The only moving parts are the rotating brushless motors and propellers. So having fewer moving parts means reducing the chance that system will fail. However, there are many limitations associated with conventional quadcopters. The conventional quadcopter stabilizes and controls its attitude by changing the RPM (Revolution Per Minute) of the four motors and cause the thrust change on each propeller. Since the motor is controlled by the ESC which can only make motor to spin in one direction, the thrust that is generated by the fixed pitch propeller can only be positive. Therefore, it’s impossible to generate negative thrust during the flight. This greatly-reduced agile and aerobatic maneuverability of the quadcopter limits the options for the intense maneuver type of mission such as search and rescue or disaster relief [7]. Besides, a fixed pitch propeller is designed to have its maximum efficiency when being operated at a certain RPM. For a quadcopter with fixed pitch propeller, it is almost impossible to fly at its best efficiency of the propeller because in order for the quadcopter to stabilize itself, the RPM of the propeller needs to be constantly changed by the motor. Thus, the fixed-pitch quadcopter consumes more power due to the low efficient of the fixed pitch propeller, which results in reducing the overall flight time [4]. In addition, when developing a large-sized quadcopter, the flight control can be a problem. When the size of the quadcopter increases, the size of the motor and propeller also needs to increase. This leads to increasing the rotational inertia from the motor and propeller, which acts against the electrical motor changing the rotational speed instantaneously and thus delaying the response time. If the propeller and motor keep increasing, eventually the rate of rotational inertia becomes so high that the quadcopter can no longer stabilize itself by changing the RPM due to the instant torque that needs to change the rotational speed that cannot be overcome by the rotational inertia [6]. Most of the quadcopters on the market today are pretty small because the size of the motor and propeller is too small to have any effect on their flight control.

2.2 Development of Variable Pitch Quadcopter

The first quadcopter was built and flown in 1922 by Etienne Oehmichen [14], as shown in Figure 2.2. It consisted of four large propellers and was capable of carrying one person. This one broke the new record at its time for flying the distance of 360 meters. However, due to the stability issues, the project was cancelled by the United State Army. Later on, another quadcopter named Convertawings Model A [14] was built and flown in 1956; it was designed by Dr. George de Bothezat and Ivan Jerome. This is the first quadcopter which used a variable pitch rotor to the varying thrust of each rotor to control pitch, roll and yaw. Figure 2.3 shows that he quadcopter is controlled by one pilot. Nonetheless, this one also faced the control problem, and the pilot was overwhelmed by controlling all four rotor thrusts at the same time. So the project was also cancelled by the United State Army [14].

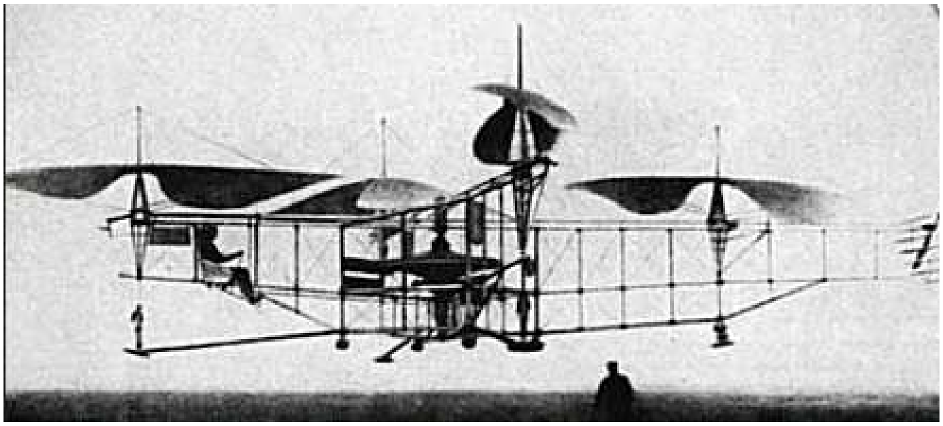

Figure 2. 2: First quadcopter developed by Etienne Oehmichen in 1922 [14]

Figure 2. 3: Convertawings Model “A” Quadcopter [14]

Today there are a few research groups and hobbyists who have designed and explored the potential of the variable pitch quadcopter. These researchers and hobbyists demonstrated a variety of configurations of the variable pitch quadcopter. Some of them were designed in X configuration, and some of them – in H configuration. They can be powered with a single electrical motor or gas-powered engine with complex drivetrains. Some of them have four small electrical motors that are attached directly to the variable pitch rotor.

The variable pitch quadcopter is a new research topic in the modern multirotor technology utilizing the variable pitch rotor to provide an increased degree of freedom for controlling the thrust generated by the rotor. The variable pitch quadcopter is able to change the thrust by varying the blade pitch angle of the rotor or increasing the motor RPM, – or by the combination of both [7]. This gives variable pitch quadcopter advantages in terms of overcoming the limitations of the fixed pitch quadcopter. The variable pitch can provide negative thrust for the quadcopter which can help the quadcopter to do an aggressive maneuver [5]. Also, to scale up the size of quadcopter is no longer an issue because the variable pitch quadcopter flight control does not totally depend on the RPM of the motor anymore. The thrust can be varied by changing the blade pitch of each rotor and allowing the rotor to increase thrust instantaneously. A research group from Massachusetts Institute of Technology Aerospace Controls Laboratory by Cutler [6][5][7] has demonstrated the full potential of what variable pitch quadcopter can actually do. In order to keep the design simple, Cutler modified a regular fixed-pitch quadcopter to a variable pitch quadcopter by replacing the fixed-pitch propeller to a variable pitch rotor that was initially made for helicopter tail rotor and adding a servo for controlling the pitch. His research demonstrates that the time responses to thrust change of variable-pitch rotor have a significant advantage over the fix-pitch propeller, as shown in Fig. 2.4a and 2.4b. The rate of change of thrust for the variable-pitch rotor is much faster, compared to that of the fixed-pitch propeller. This allows the variable-pitch quadcopter to perform an aggrieve maneuver and show a faster response to the input command. Cutler [6] also demonstrated that the variable pitch quadcopter can fly upside down by producing the negative thrust. This allows the quadcopter to perform inverted flight and aerobic maneuvers.

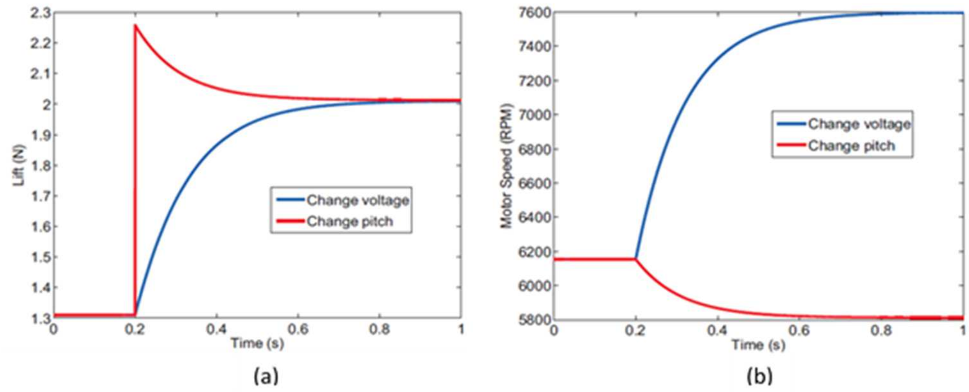

Figure 2. 4a and 2.4b: (a) Time response for changing the thrust between the variable-pitch and fixed-pitch propeller. (b) Time response for changing the RPM between the variable-pitch and fixed-pitch propeller.

Another research group from the National University of Singapore designed and built a gas-powered variable pitch quadcopter for a long-endurance flight. This quadcopter is in X configuration, and it uses a single two-stroke nitro engine to power all four variable-pitch rotors. The prototype can be seen below in Fig. 2.5. [9] Although it had a successful take off, the quadcopter suffered serious vibration due to the gas-powered engine and complex drivetrain. The flight lasted only a few minutes.

Figure 2. 5: A fully assembled gas-powered quadcopter prototype from the National University of Singapore. [9]

In the past two years, the first commercial RC variable-pitch quadcopter was developed and sold by Hobbyking Company [19]. This quadcopter used a single electrical motor to power four variable-pitch propellers. This quadcopter was able to stabilize itself during its hover, and it could perform aerobic maneuvers and an inverted flight. However, it could only fly for 10 minutes due to the small size and the necessity to be powered by battery. Figure 2.6 shows the RC-variable-pitch quadcopter.

Figure 2. 6: RC variable pitch quadcopter made by Hobbyking. [19]

Also, there are some hobbyists who are currently developing variable-pitch quadcopters with a variety of quadcopter configurations and power transmission systems such as HG3 made by Roberto [15] and Gas-Powered Single Engine Variable-Pitch Quadcopter made by Silas. [16] Some of them claimed to be able to fly and some of them are still in the developing phase. But none of them has shown that their quadcopter was able to achieve a long endurance flight.

2.3 Quadcopter Flight Dynamics

A common fixed-pitch quadcopter consists of four motors. Each motor is controlled independently by the flight controller. By varying the RPM amount for four motors, the flight controller can regulate the quadcopter's direction. By design, a quadcopter must balance the torques created by the motors and propellers to prevent asymmetric torque. This is accomplished by having counter-rotating propellers. Luukkonen [10] portrays his definition of a quadcopter in X configuration in Fig. 2.7 [10]. The motors 1 and 3 are located in the counter-clockwise (CCW) direction, and motor 2 and motor 4 – in the clockwise (CW) direction. To obtain an intuitive understanding of the flight dynamics of a quadcopter, one can describe how the flight controller can be used to obtain a forward motion. A forward motion can be obtained by increasing the RPM for motors 2 and 3 and by decreasing the RPM for motors 1 and 4, respectively. To move left, the flight controller must increase the RPM for motors 1 and 2 and decrease the RPM for motors 3 and 4. To yaw in the clockwise direction, the flight controller must increase the RPM to motors 1 and 3 and decrease the RPM to motors 2 and 4.

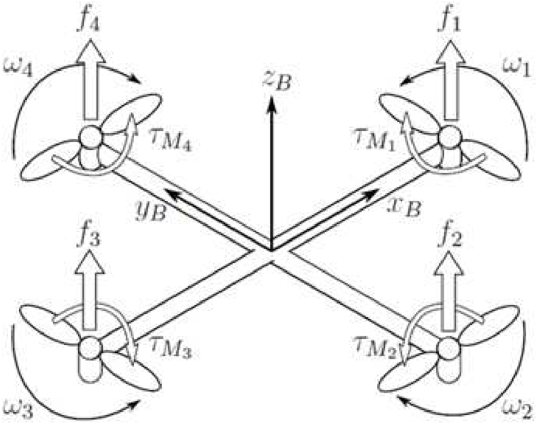

Figure 2. 7: Free body diagram of quadcopter in X-configuration. The coordinate system (x_B , y_B , z_B) is in the body frame of the quadcopter. [10]

Equations of Motion

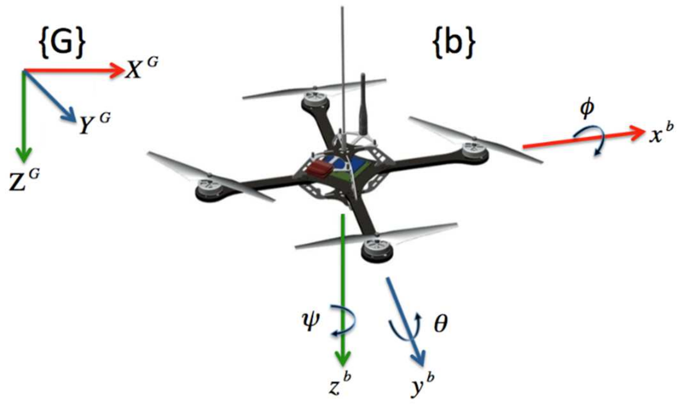

Figure 2. 8: A diagram of a quadcopter, where {G} is the global coordinate system and {b} is the body frame system. [17]

There are two coordinate systems to describe the dynamic motion of quadcopter. One is the body coordinate frame, and the other one is the global coordinate frame, as shown in Figure 2.8. The body frame will be used for the attitude control, since the flight controller inertial measurement unit (IMU) only measures the movement in the body frame. The global frame is used for calculating the position of the quadcopter, since the global positioning system (GPS) is measured in the global system. According to William Selby [17], the quadcopter equations of motion can be expressed as:

$$\begin{bmatrix} \dot{X}^G \\ \dot{Y}^G \\ \dot{Z}^G \end{bmatrix} = R_b^G \begin{bmatrix} \dot{x}^b \\ \dot{y}^b \\ \dot{z}^b \end{bmatrix} \qquad (2.1),$$

where $\dot{X}^{\mathrm{G}}$ is the velocity of quadcopter in X direction in the global frame, and $\dot{Y}^{\mathrm{G}}$ is the velocity of quadcopter in Y direction in the global frame.

$\dot{Z}^{\mathrm{G}}$ is the velocity of quadcopter in Z direction in the global frame.

$\dot{x}^{\mathrm{b}}$ is the velocity of quadcopter in X direction in the body frame.

$\dot{y}^{\mathrm{b}}$ is the velocity of quadcopter in Y direction in the body frame.

$\dot{z}^{\mathrm{b}}$ is the velocity of quadcopter in Z direction in the body frame.

R_b^G is the is the rotation matrix that transfers the body frame to the global frame

θ is the pitch angle of the quadcopter in X direction in the body frame.

Ψ is the yaw angle of the quadcopter in Z direction in the body frame.

ϕ is the roll angle of the quadcopter in Y direction in the body frame.

The linear velocity of the quadcopter in the global frame is expressed by (2.1). R_b^G is the rotation matrix that transfers the body frame to the global frame, and it can be derived by Euler angles. The R_ϕ, R_θ, R_ψ is the rotational matrix with Z axis, Y axis and X axes, which represent the vehicle yaw, pitch and roll motion, respectively. A complete rotational matrix from the global frame to the body frame can be obtained by (2.4a). A complete rotational matrix from the body frame to the global frame can be obtained by taking a transpose of

$$R_G^b = R_{(\phi)} R_{(\theta)}\, R_{(\psi)} \tag{2.2a}$$

$$R_b^G = (R_G^b)^T \tag{2.2b},$$

where

$$R_\phi = \begin{bmatrix} 1 & 0 & 0 \\ 0 & cos(\phi) & -sin(\phi) \\ 0 & sin(\phi) & cos(\phi) \end{bmatrix} \quad R_\theta = \begin{bmatrix} cos(\theta) & 0 & sin(\theta) \\ 0 & 1 & 0 \\ -sin(\theta) & 0 & cos(\theta) \end{bmatrix} \quad R_\psi = \begin{bmatrix} cos(\psi) & -sin(\psi) & 0 \\ sin(\psi) & cos(\psi) & 0 \\ 0 & 0 & 1 \end{bmatrix}$$

(2.3)

$$R_b^G = \begin{bmatrix} cos(\psi)cos(\theta) & cos(\psi)sin(\phi)sin(\theta) - cos(\phi)sin(\psi) & cos(\phi)cos(\psi)sin(\theta) + sin(\phi)sin(\psi) \\ sin(\psi)cos(\theta) & sin(\phi)sin(\psi)sin(\theta) + cos(\phi)cos(\psi) & cos(\phi)sin(\psi)sin(\theta) - cos(\psi)sin(\phi) \\ -sin(\theta) & cos(\theta)sin(\phi) & cos(\phi)cos(\theta) \end{bmatrix}$$

(2.4)

The linear acceleration of the quadcopter in the global frame is expressed by equation 2.10 which is derived from Newton's second law, F = ma. For the quadcopter, this can be simplified, as demonstrated in Equation 2.5. Assume that quadcopter is a rigid and symmetrical body where the forces acting upon the quadcopter are the gravitational force (F_g,), the thrust produced by the rotors (F_T), and the drag force generated by the linear motion of the quadcopter (F_d).

$$m\ddot{X}^G = F_g - F_T^G - F_d \tag{2.5}$$

$$F_T^G = R_b^G F_T^b \tag{2.6}$$

The thrust force vectors, F_T^G, can be transformed from the body frame to the global frame by using the rotation matrix R_b^G multiplied by F_T^b, which is the thrust force that is generated by four rotors located in the body frame.

$$F_T^b = \sum_{i=1}^{4} F_i \tag{2.7}$$

The thrust produced by each rotor can be expressed as $K_T * \omega^2$, where K_T is the thrust constant and ω is the rotor angular velocity.

$$F_T^G = R_b^G \sum_{i=1}^{4} F_i = \begin{bmatrix} 0 \\ 0 \\ K_T \ \sum_{i=1}^{4} \omega_i^2 \end{bmatrix} \tag{2.8}$$

F_d is the drag force that is produced by the air friction of the body moving in X, Y, and Z directions, where K_{dx} , K_{dy} , K_{dZ} is the drag constant of quadcopter in X, Y, and Z directions of the body frame.

$$F_d = \begin{bmatrix} K_{dx} & 0 & 0 \\ 0 & K_{dy} & 0 \\ 0 & 0 & K_{dz} \end{bmatrix} \begin{bmatrix} \dot{X}^G \\ \dot{Y}^G \\ \dot{Z}^G \end{bmatrix} \tag{2.9}$$

As a result, in the global frame, the linear acceleration motion of quadcopter moving in X, Y, and Z direction can be expressed as:

$$\begin{bmatrix} \ddot{X}^G \\ \ddot{Y}^G \\ \ddot{Z}^G \end{bmatrix} = \begin{bmatrix} \frac{1}{\mathrm{m}}(-\left[cos(\phi)cos(\psi)sin(\theta) + sin(\phi)sin(\psi)\right] F_T^b - K_{dx}\dot{X}^G \\ \frac{1}{\mathrm{m}}(-\left[cos(\phi)sin(\psi)sin(\theta) + cos(\psi)sin(\phi)\right] F_T^b - K_{dy}\dot{Y}^G \\ \frac{1}{m}(-\left[cos(\phi)cos(\theta)\right] F_T^b - K_{dx}\dot{Z}^G) + g \end{bmatrix} \tag{2.10}$$

The angular velocity of the quadcopter in the global frame is expressed by Equation 2.13, which is derived from Equation 2.11. The p, q, r is the roll, pitch and yaw rates, respectively, along with the X, Y, and Z directions in the body frame.

$$\omega = \begin{bmatrix} p \\ q \\ r \end{bmatrix} = R_\phi R_\theta \begin{bmatrix} 0 \\ 0 \\ \dot{\psi} \end{bmatrix} + R_\phi \begin{bmatrix} 0 \\ \dot{\theta} \\ 0 \end{bmatrix} + \begin{bmatrix} 0 \\ 0 \\ \dot{\phi} \end{bmatrix} = \begin{bmatrix} 1 & 0 & -sin(\theta) \\ 0 & cos(\phi) & sin(\phi)cos(\theta) \\ 0 & -sin(\phi) & cos(\phi)cos(\theta) \end{bmatrix} \begin{bmatrix} \dot{\phi} \\ \dot{\theta} \\ \dot{\psi} \end{bmatrix} = S \begin{bmatrix} \dot{\phi} \\ \dot{\theta} \\ \dot{\psi} \end{bmatrix}$$

(2.11),

where S is the transformation matrix that converts the quadcopter's angular velocity from the global frame to the body frame. Similarly, by taking the inverse of S matrix, we can transform from the body frame back to the global frame.

$$S^{-1} = \begin{bmatrix} 1 & sin(\phi)tan(\theta) & cos(\phi)tan(\theta) \\ 0 & cos(\phi) & -sin(\phi) \\ 0 & \frac{sin(\phi)}{cos(\theta)} & \frac{cos(\phi)}{cos(\theta)} \end{bmatrix} \tag{2.12}$$

Substituting the S^{-1} matrix to the equation 2.11 and rearranging ω, we can obtain the angular velocity of the quadcopter in the global frame.

$$\begin{bmatrix} \dot{\phi} \\ \dot{\theta} \\ \dot{\psi} \end{bmatrix} = \begin{bmatrix} 1 & sin(\phi)tan(\theta) & cos(\phi)tan(\theta) \\ 0 & cos(\phi) & -sin(\phi) \\ 0 & \frac{sin(\phi)}{cos(\theta)} & \frac{cos(\phi)}{cos(\theta)} \end{bmatrix} \begin{bmatrix} p \\ q \\ r \end{bmatrix} \quad (2.13)$$

The rotational motion of the quadcopter is defined in the body frame, since the quadcopter is assumed to be a rigid and symmetrical structure; this makes it much easier to sum up all torques in the center of the quadcopter body instead of summing up all torques in the center of the global frame. If we sum up all the torques that are acting on the quadcopter, we can express the angular acceleration of inertia equation by using the Euler's equations of rigid body dynamics.

$$J_b\dot{\omega} + (\omega \ \times J_b\omega) = T_r - T_g \quad (2.14),$$

where J_b is the moment of inertia of quadcopter body

$$J_b = \begin{bmatrix} J_x & 0 & 0 \\ 0 & J_y & 0 \\ 0 & 0 & J_z \end{bmatrix} \quad (2.15)$$

T_r is the torque created by the rotor along the x, y, z of the body frame, which corresponds to the pitch (τ_ϕ), roll (τ_θ), and yaw (τ_ψ) motions. This is demonstrated in Equation 2.16, where l is the moment arm moving from the center of the rotor to the center of the quadcopter. K_T and K_d are the thrust coefficient and drag coefficient of the rotor, respectively. W_{1-4} is the angular velocity of the four rotors.

$$T_r = \begin{bmatrix} \tau_\phi \\ \tau_\theta \\ \tau_\psi \end{bmatrix} = \begin{bmatrix} lK_T(W_4^2 - W_2^2) \\ lK_T(W_1^2 - W_3^2) \\ K_d(W_1^2 - W_2^2 + W_3^2 - W_4^2) \end{bmatrix} \quad (2.16)$$

T_g is the gyroscopic effect from the rotating rotor that is coupled with the rotating body of the quadcopter. The rotor's axis is fixed on the quadcopter's body frame; therefore, the rotor's axis is moving with the rotation of the body frame.

$$T_g = \omega \times \begin{bmatrix} 0 \\ 0 \\ J_r \end{bmatrix} (W_1 - W_2 + W_3 - W_4) \qquad (2.17),$$

where $\omega = [p, q, r]^T$, J_r is the rotor moment of inertia in Z axis; as a result, we get the following cross product :

$$T_g = \begin{bmatrix} J_r q(W_1 - W_2 + W_3 - W_4) \\ -J_r p(W_1 - W_2 + W_3 - W_4) \\ 0 \end{bmatrix} \qquad (2.18)$$

The cross product of $(\omega\ \times J_b\omega)$ which we get then is this one:

$$(\omega \times J_b\omega) = \begin{bmatrix} (J_z - J_y)qr \\ (J_x - J_z)pr \\ (J_y - J_x)pq \end{bmatrix} \qquad (2.19)$$

After substituting T_g, T_r and $\omega\ \times J_b\omega$ back to Equation 2.14, we get:

$$J_b\dot{\omega} = \begin{bmatrix} (J_y - J_z)qr - J_r q(W_1 - W_2 + W_3 - W_4) + lK_T(W_4^2 - W_2^2) \\ (J_z - J_x)pr - J_r p(W_1 - W_2 + W_3 - W_4) + lK_T(W_1^2 - W_3^2) \\ (J_x - J_y)pq + K_d(W_1^2 - W_2^2 + W_3^2 - W_4^2) \end{bmatrix} \qquad (2.20)$$

After dividing J_b on both sides, we get:

$$\dot{\omega} = J_b^{-1} \begin{bmatrix} (J_y - J_z)qr - J_r q(W_1 - W_2 + W_3 - W_4) + lK_T(W_4^2 - W_2^2) \\ (J_z - J_x)pr - J_r p(W_1 - W_2 + W_3 - W_4) + lK_T(W_1^2 - W_3^2) \\ (J_x - J_y)pq + K_d(W_1^2 - W_2^2 + W_3^2 - W_4^2) \end{bmatrix} \qquad (2.21),$$

where

$$J_b^{-1} = \begin{bmatrix} 1/J_x & 0 & 0 \\ 0 & 1/J_y & 0 \\ 0 & 0 & 1/J_z \end{bmatrix} \tag{2.22}$$

Substituting J_b^{-1} with the final angular acceleration in the body frame can be expressed as

$$\dot{\omega} = \begin{bmatrix} \frac{1}{J_x}[(J_y - J_z)qr - J_r q(W_1 - W_2 + W_3 - W_4) + lK_T(W_4^2 - W_2^2)] \\ \frac{1}{J_y}[(J_z - J_x)pr - J_r p(W_1 - W_2 + W_3 - W_4) + lK_T(W_1^2 - W_3^2)] \\ \frac{1}{J_z}[(J_x - J_y)pq + K_d(W_1^2 - W_2^2 + W_3^2 - W_4^2)] \end{bmatrix} \tag{2.23}$$

The flight dynamic of the variable pitch quadcopter is the same as that of the fixed pitch quadcopter, except the lift and drag equations for the variable pitch rotor, which are different from the fixed pitch propeller. Since the variable pitch rotor can generate the lift by changing the blade pitch angle or RPM, this gives the variable pitch quadcopter one more degree of freedom, compared to the fixed pitch quadcopter. The lift and drag equations of a variable pitch rotor can be expressed as

$$L = b_L \omega^2 \alpha \tag{2.24}$$

$$T_r = b_{D1}\omega^2 + b_{D2}\omega^2\alpha + b_{D3}\omega^2\alpha^2 \qquad (2.25),$$

where L is the thrust generated by the rotor, T_r is the torque or drag generated by the rotor, ω is the RPM of the rotor, α is the blade pitch angle, and, b_L , b_{D1} , b_{D2} and b_{D3} are the aerodynamic constants. A least-squared regression plot generated by Qprop is used to obtain the values of b_L , b_{D1} , b_{D2} and b_{D3} [6].

2.4 Previous Work of Variable Pitch Quadcopter

The first variable-pitch gas-powered quadcopter project started in 2013. It was a senior design project for the class of MAE 4344 at OSU. The first group of OSU MAE undergraduate students designed the variable-pitch quadcopter. Their goal was to develop a long endurance-flight quadcopter. Because of time constraints, they did not complete the project. However, they were able to complete the overall design of the variable-pitch quadcopter and manufacture the major parts of this quadcopter. In 2014, the second group of undergraduate students took over this project. They were able to complete the final assembly and conduct a flight test for the platform. Figure 2.9 shows the completed gas-powered variable-pitch quadcopter [18].

Figure 2. 9: A gas-powered variable-pitch quadcopter that was built by OSU senior design students in 2016. [18]

This vehicle used a 61SX-Hring WC Nitro engine to power the system. This is due to the energy density of glow fuel that is much higher than the LiPo battery. This means that for the same amount of takeoff weight, a gas-powered quadcopter can carry more fuel and has longer endurance compared to the electricity-powered quadcopter.

During the conceptual design stage, an evaluation was made between X-shape body frame and H-shape body frame, as shown in Fig. 2.10a and Fig. 2.10b. The evaluation was based on the following design factors: the weight of the structure, the ease in manufacturing the frame, the vehicle stability, the cost of the material, and the mechanical layout of the system. The results of the configuration comparison showed that the H-configuration is better, as shown in Table 2.1 [20].

(a) (b)

Figure 2. 10a and 2.10b: (a) X- Shape body frame. (b) is H-shape body frame.[20]

Table 2. 1: A Comparison between "X" and "H" configuration [20]

CRITERIA	WEIGHT	"X"	"H"
Less Weight	.3	7	4
Ease of build	.2	3	7
Stability	.1	5	5
Cost	.15	3	6
Mechanical layout	.25	2	9
Final Score		4.15	6.25

The main reason that the H-Design was chosen over the X-Design was the fact that the H-Design has more working space in-between the upper and lower panels of the body frame. This could make the project much easier on drivetrain design and easier to assemble, – unlike the X-Design which has a smaller working space because in this case, everything clusters in the center of the body frame. This could make the drivetrain much harder to design and give less room to work with.

Power Transmission

This vehicle used a belt-driven system to transfer the power from the main engine to four rotors, as shown in Fig. 2.11.

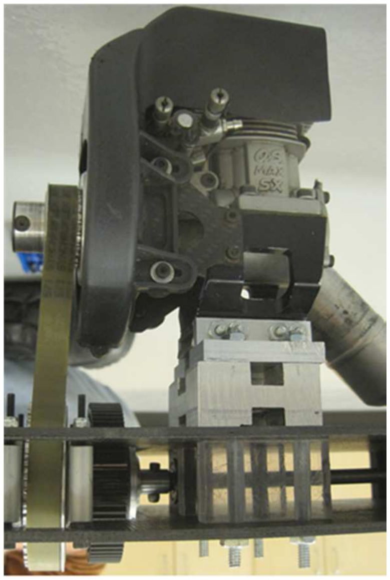

Figure 2. 11: A single gas-powered engine used to power four rotors [18]

The gas-powered engine drove the main shaft by a set of belt and pulley. Four rotors were driven by a set of two smaller pulleys that were driven by the main shaft. The advantage of using a belt-driven system over a gear-driven system is that when the vehicle experiences excessive vibrations, gear-driven systems tend to have a lower tolerance to vibration than a belt-driven system [20]. Additionally, quadcopters must have each rotor rotate opposite one other. With a belt-driven system, this is done simply by twisting the belt 90 degree from the main shaft to the rotor. The direction of rotor's rotation is dependent on the direction of belt twist. To simplify the assembly process, power transmission components such as the rotor assembly and gear reduction assembly were borrowed from the Compass Helicopters 7hv V2 power system, which is a RC gas-powered helicopter. This particular RC helicopter was chosen due to the fact that it has the largest and toughest tail rotor design on the market [20].

The gear reduction system from the engine to the main drive shaft has the gear ratio 9.3:1, whereas from the main drive shaft to the rotor shaft the gear ratio is 1:1.75. The combined gear ratio from the engine to the rotor shaft gave the rotor a maximum RPM of 3010 [20]. Figure 2.12 shows the process of the rotor assembly. The arms for supporting the rotors were made of aluminum square tubing. This square tubing could easily fit into the body frame and switch between the upper and low panel.

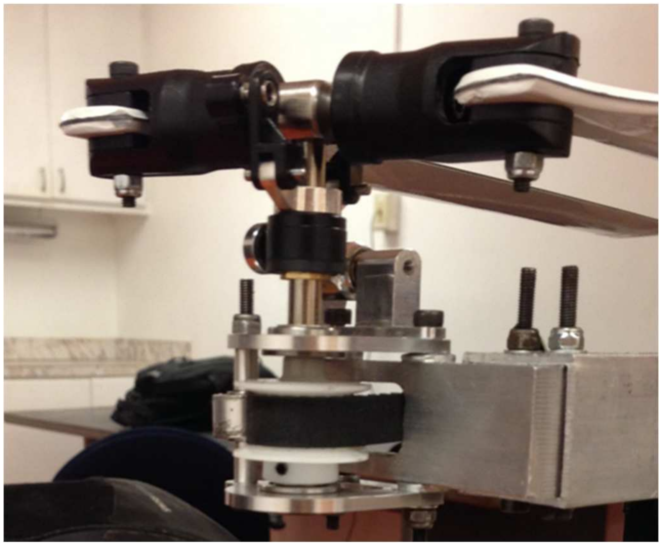

Figure 2. 12: An example of the completed rotor assembly [18].

Blade Analysis

This vehicle was designed to achieve liftoff at a minimum of 10 pounds of payload. The 61SX-Hring WC gas-powered engine is rated at a maximum output power of 2.2 hp, which could provide maximum power of 0.5 hp per each rotor. After using the Xfoil and Qprop programs to calculate the maximum thrust that can be generated by providing 0.5 hp to the rotor, the Qprop gave about 8.4 pounds of thrust per each rotor. The rotor blade used on this vehicle is SAB 13.5 inch blade (tip to hub center) and 1.3 inch of chord length, as shown in Fig. 2.13. The maximum chord thickness was about 17% of its chord length, which is similar to the NACA 0017 airfoil. The aerodynamic properties of the airfoil can be read off from Fig. 2.15 and thrust calculations by Qprop shown in Fig. 2.14.

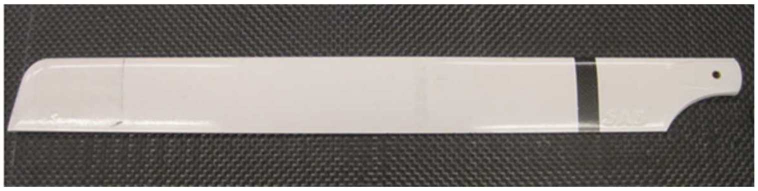

Figure 2. 13: This is a 325 mm length of helicopter rotor blade. It is made of carbon fiber composite material and commonly used on Trex-450 RC Helicopter. [20]

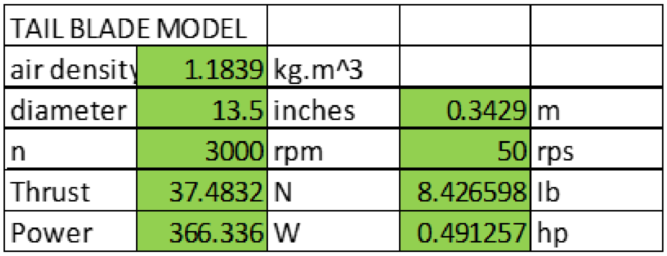

TAIL BLADE MODEL				
air density	1.1839	kg.m^3		
diameter	13.5	inches	0.3429	m
n	3000	rpm	50	rps
Thrust	37.4832	N	8.426598	lb
Power	366.336	W	0.491257	hp

Figure 2. 14: Thrust and power consumption can be calculated using Qprop program

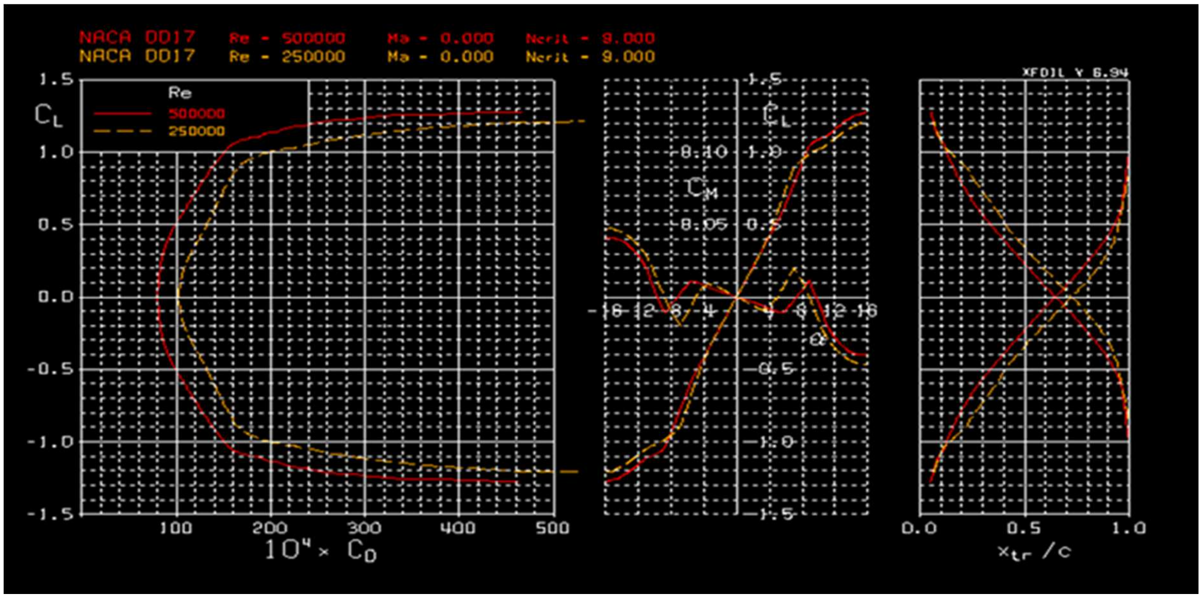

Figure 2. 15: The graph illustrates the CL/CD curve, CL/α curve and X_{tr}/C, based on Reynolds number of 250,000 and 500,000. CL_{Max} , and CL_{min} values can be read off from the CL/CD curve and used for the Qprop input value [20]

Final Design

The final design of the variable pitch quadcopter weighted about 13 pounds, and its MTOW was about 30 pounds. It replaced the 61SX-Hring WC Nitro engine with the new EVOE15GX engine. This new engine had the same hp, compared to the old one, but it runs off gasoline instead of glow fuel, which proved more fuel-efficient. According to the last team flight testing record, this quadcopter was able to lift off and stay in the air for a short period of time. The vibration caused by the reciprocating engine and rotating belts have major effects on the flight controller, which makes it difficult to stable the quadcopter. Also, the gas-powered engine experienced engine surging when the air and fuel mixture were incorrect and caused RPM to suddenly drop. Although this quadcopter did not hover for a long period of time, it proved that this variable pitch quadcopter concept worked and that the vehicle was able to lift off and stay in airborne for a short period of time. This indicated that their design and calculations were not too far off and that it could be used as a reference for developing a variable pitch quadcopter in the future.

Logan’s Variable Pitch, Variable Tilt Quadcopter Conceptual Design

After the previous variable pitch gas-powered quadcopter project was finished, Logan Kunya took over the project and made a variable pitch, variable tilt quadcopter conceptual design based on the previous variable pitch gas-powered quadcopter design. The variable pitch led to developing the variable tilt quadcopter conceptual design, as shown in Fig. 2.16. The idea behind his design was to use a variable pitch, variable tilt rotor on a quadcopter that gave the quadcopter the ability of having a vertical takeoff and landing, increasing hovering efficiency and achieving a high cruising speed by tilting the rotors forward during the flight.

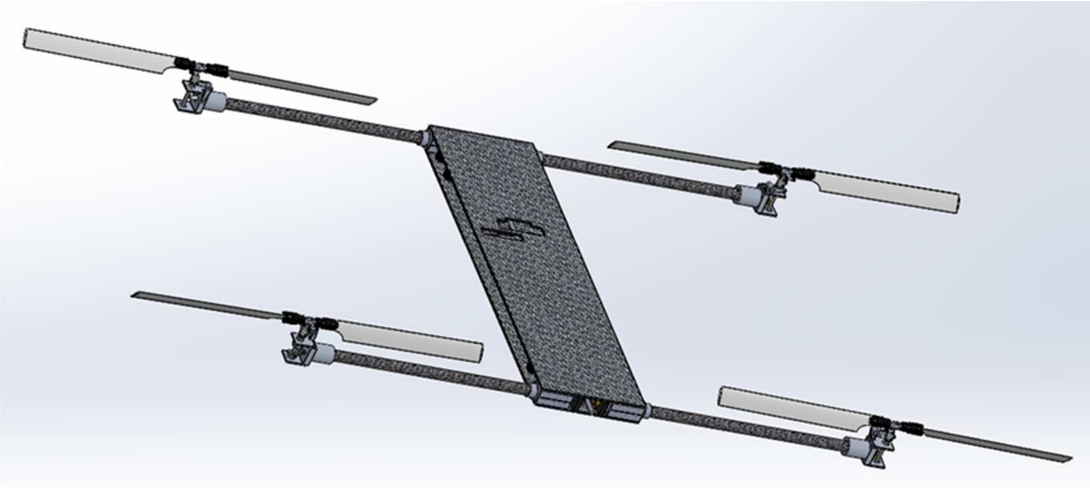

Figure 2. 16: Logan's variable pitch and variable tilt quadcopter conceptual design

Logan’s conceptual design is similar to the first gas-powered quadcopter that was made by a group of MAE students from OSU in 2013. Many of its parts were borrowed from the previous gas-powered quadcopter such as carbon fiber body frame, variable-pitch rotor assembly, gas-powered transmission assembly, etc. However, there are some differences between its variable pitch, variable tilt quadcopter and the previous gas-powered variable-pitch quadcopter. The previous gas-powered quadcopter used the belt system to power all four rotors, which is a very robust system, but the belt-driven system is not designed for the variable tilt of the rotors. This is because the belt is already twisted for 90 degrees in order to be able to transfer the power from the central drive shaft to the vertical rotor shaft. Any further twist will cause the space between the upper and lower belt decrease and eventually run into each other. In Logan’s conceptual design, he chose to use the gear-driven system, as was mentioned earlier. The central drive shaft powers two differential gearboxes in the front and rear ends of the quadcopter. Fig. 2.17 shows the concept of differential gearbox design using three bevel gears. The arm shafts which power the vertical rotor shafts are connected by the differential gearbox. This design allows the rotor able to rotate around the arm shaft axis and spin at the same time. The arm shaft was supported by the rotating bracket assembly as shown in Fig. 2.18; this assembly allowed the carbon fiber tube which was the main support structure for the arm shaft to rotate around its axis.

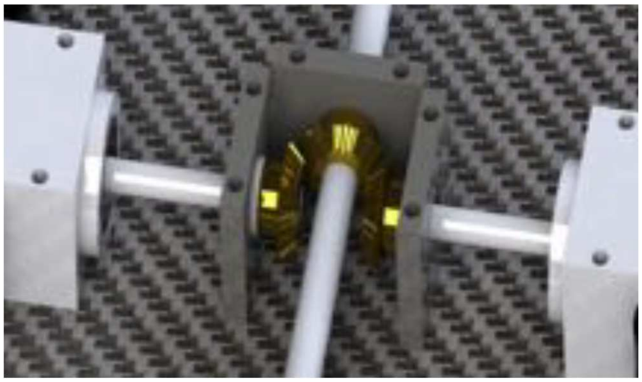

Figure 2. 17: A conceptual design of differential gearbox by Logan

Figure 2. 18: A tilt rotor mechanism conceptual design by Logan

Although this conceptual design may work in theory, this is a difficult problem since designing and developing the variable-pitch quadrotor is already a major challenge project to work on. So this variable-pitch project took over the conceptual design and modified it into a non-variable tilt rotor variable-pitch quadcopter design. But since this variable project may be used in the future for studying the variable tilt rotor quadcopter dynamics, the modified version of variable pitch quadrotor design kept most of tilt rotor designs by fixing the rotating arm support bracket. Besides, the modified version of the variable-pitch quadrotor design had to fix some of the parts from the previous gas-powered variable-pitch design and add the new parts to make it work.

CHAPTER III

DESIGN METHODOLOGY

3.1 Design Requirements

This research project is focused on developing a long-endurance variable-pitch quadrotor. The objective is to design and build a variable-pitch quadrotor which would be capable of carrying a minimum of 10 pounds of payload and able to fly for two hours. This could be achieved by using a single gas-powered engine to power the variable-pitch quadrotor since the energy density of gasoline is much higher than the LiPo battery, as was mentioned earlier. This project is divided into three phases. The first phase of this project is mainly focused on the design and fabrication of the variable pitch quadrotor by using a single electric motor to power the vehicle. This is because the first phase is a proof-of-concept and because the electric motor is much easier to work with, compared to a gas-powered engine. The second phase of the project was focused on the stability and control of the variable-pitch quadrotor and PID tuning. This required doing some modifications of the current quadcopter flight controller because most of the flight controllers are designed for controlling the fixed-pitch quadcopter only. Fig. 3.1 illustrates the overall flow chart of design choices for developing a variable-pitch quadcopter. The variable pitch quadrotor requires to control the RPM and the blade pitch of the rotor in order to fly stably. The third phase of the project was focused on the long-endurance flight, when the electric motor was replaced with a gas-powered engine or a hybrid power system.

Both systems have certain pros and cons. The challenge with a gas-powered engine is that the reciprocal motion of piston may cause excessive vibrations in the vehicle structure, and this may lead to the flight controller to be unable to function properly. However, developing the hybrid power system could be the solution to this problem, since the system is neither directly nor mechanically connected with the vehicle's transmission. Thus the system can be easily modified to reduce the rate of vibration.

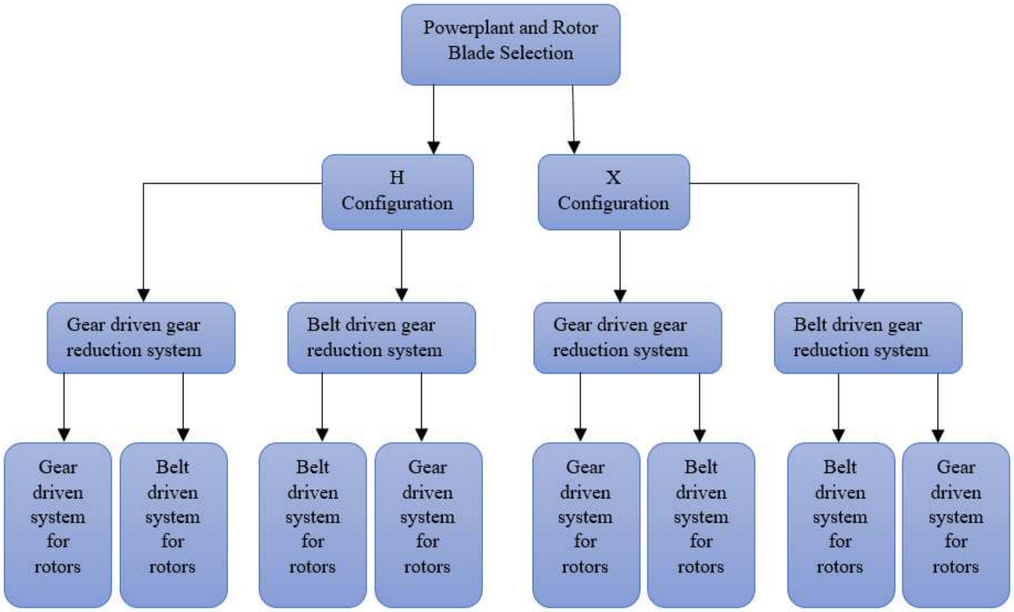

Figure 3. 1: This flow diagram illustrates the design process of a variable-pitch quadcopter

3.2 Configuration Design

The most common configuration design for the quadcopter is X-shape and H-shape. As mentioned earlier, a group of engineering students from MAE 4344 already did a pros and cons analysis on both configuration design in 2013 [18] [20]. The results of their analysis showed that H-shape is a better design for the variable-pitch quadrotor due to many reasons, such as the simplicity of manufacturing, having more space for the transmission system, and getting more options for assembling and disassembling in an easier way. More importantly, by choosing the H configuration, we can use some of the parts from the last gas-powered quadcopter project and modify it based on our design. Figure 3.2 shows an example of H-shape configuration variable-pitch quadcopter that was made by OSU senior design students in 2014. [18]

Figure 3. 2: Example of H-shape configuration variable pitch quadcopter [18]

3.3 Power Transmission Design Overview

The transmission system is responsible for transferring the power from the single motor to all four rotors. This can be done by using the pulley and belt system or gear and pinion system, – or the combination of both. All the rotors will have the same RPM because all four rotors have the same gear ratio, and they all share the same central drive shaft. This could keep all four rotors identical and easy to manufacture and assembly. The gear reduction part only happens from motor shaft to the central drive shaft. The figure 3.3 shows an example of the belt-driven system. Each belt is twisted for 90 degrees from the rotor shaft towards the central drive shaft. The belt-driven system is very robust and has more tolerance to misalignment. However, it requires the right tension for the belt, if the tension at the level of the belt is too lose or too tight, it can result in an excessive belt slip and power lose [21].

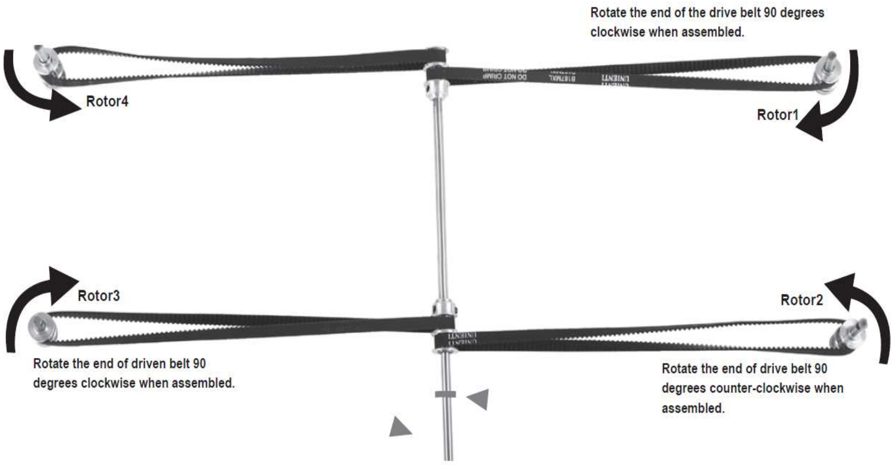

Figure 3. 3: A schema of the belt power transmission system from the RC variable-pitch quadcopter made by HobbyKing. [19]

On the other hand, the gear-driven system in Fig. 3.4 shows how the four rotors were powered by bevel gears.

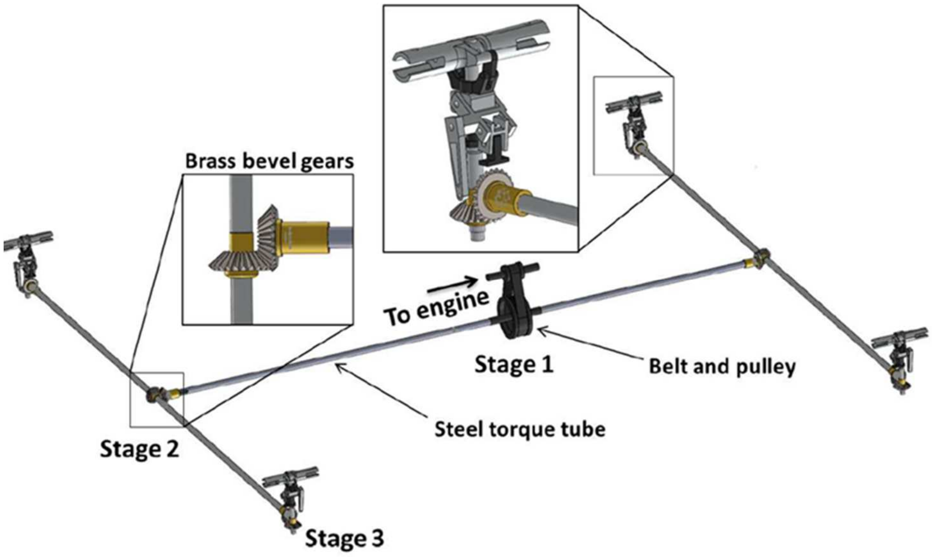

Figure 3. 4: A schematic drawing of the gear power transmission system for the variable-pitch quadcopter [8]

The central drive shaft has two bevel gears that mounted to the front and back parts of the shaft. Then the rotational motion transfers to the front and back rotors by attaching another bevel gear onto the rotor arm shaft that is perpendicular to the central drive shaft. The H shape configuration is axially symmetrical; this makes the bevel gear driven system much easier to work with because there is no need to correct each rotor's direction of rotation. They are already in the correct rotation as long as four rotors are exactly the same. However, the gear-driven system requires high precision fittings and less tolerance to vibration. A small misalignment can cause major gear wear and power loss. Besides, the bevel gear can only be mounted on a solid shaft's flat spot. This is because the bevel gear uses a set screw that transferred the gear onto the shaft. The friction between the screw and shaft will keep the gear and shaft together. Fig. 3.5 illustrates a gear mounted on a shaft by using a set screw [22]. The shaft must be solid because the hollow tube is not strong enough to stand the force that is created by the set screw and most likely will be crashed by the set screw. However, a solid steel shaft is very heavy and can reach its critical speed at lower rpm compared to the hollow shaft. Thus requires additional bearings to support the shaft and add weight and complexity to the system.

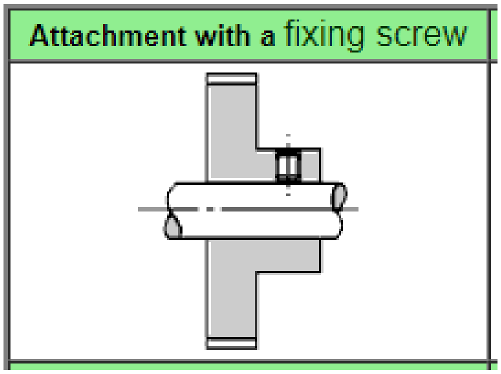

Figure 3. 5: Example of using a set screw to mount the gear on the shaft .[22]

3.4 Summary of Designs Overview

Table 3.1 shows the comparison of different designs on the variable-pitch quadcopter. All the variable-pitch quadcopters have about the same weight and using the same-sized blade, which is a symmetrical airfoil with 325 mm blade length. The comparison only provides a “fuzzy” guide of the overall design system of the variable pitch quadcopter, based on the information presented in the research paper and on common knowledge.

Table 3. 1: Comparison of variable pitch quadcopter designs

Variable Pitch Quadcopter Prototypes	**Pros**	**Cons**
Gas-powered variable pitch quadcopter [8] 	1) No central drive shaft required, weight less. 2) Less body structural weight due to the X configuration. 3) Belt-driven system for single power plant makes a more robust transmission system. 4) Gear-driven system for rotor assembly makes more efficient the transfer of the power.	1) Complex belt transmission system due to small X configuration body frame 2) Belt-driven system is less efficient, compared to the gear-driven system 3) a small compact X configuration body frame suffers from more stresses and vibrations due to the long moment arm from rotor assembly. 4) More structural components are needed for supporting the body frame and rotor arm. This increases the weight of the vehicle.
Gas-powered variable pitch quadcopter [9] 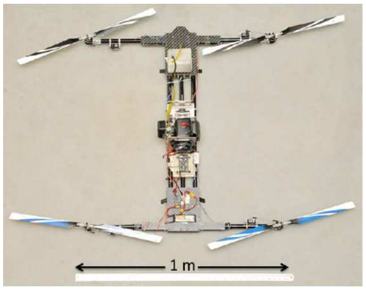	1) H configuration makes it easier to assemble 2) Power plant can choose a belt-driven system or gear driven system for transferring the power from the motor to the central drive shaft 3) Gear-driven system for rotor assembly is more efficient for transferring the power. 4) Lightweight aluminum tubes are used for the body frame to carry the structural load. 4) Less moment arm from the rotor due to large H configuration body frame.	1) Adding two gearboxes to transfer the power from the central shaft to four rotors increase the system complexity. 2) Aluminum tube body frame makes it easy to transfer the vibration and to reduce vibration dampening. 3) All gears must be properly aligned, otherwise there can be more power loss from the gear and bearings.
OSU gas-powered variable pitch quadcopter [20] 	1) H configuration is easier to assembly 2) Light-weight carbon fiber body frame provides much stronger support for the rotor arm assembly. 3) A total belt-transmission system from the motor to the rotors makes the vehicle very robust. 4) A simpler transmission design.	1) Solid steel central shaft increases weight. 2) More bearings are required for securing the central shaft 2) The belt-driven system is less efficient, compared to the gear-driven system 3) Vibration generates from the slack side of belts.

3.5 Control Method

The dynamic motion of the variable-pitch quadcopter is exactly the same as the conventional quadcopter dynamic motion. The only difference is that the variable-pitch quadrotor is controlled by varying the rotor blade pitch angle instead of varying the RPM of the propeller. For this variable-pitch quadrotor design, we will choose the H-configuration; all the rotors will have the same RPM, but each variable-pitch rotor can change its thrust by using an electrical servo to control the blade pitch angle like a helicopter tail rotor assembly. The electrical servo will be connected with a flight controller. Figure 3.6 demonstrates the mechanical system of rotor pitch control.

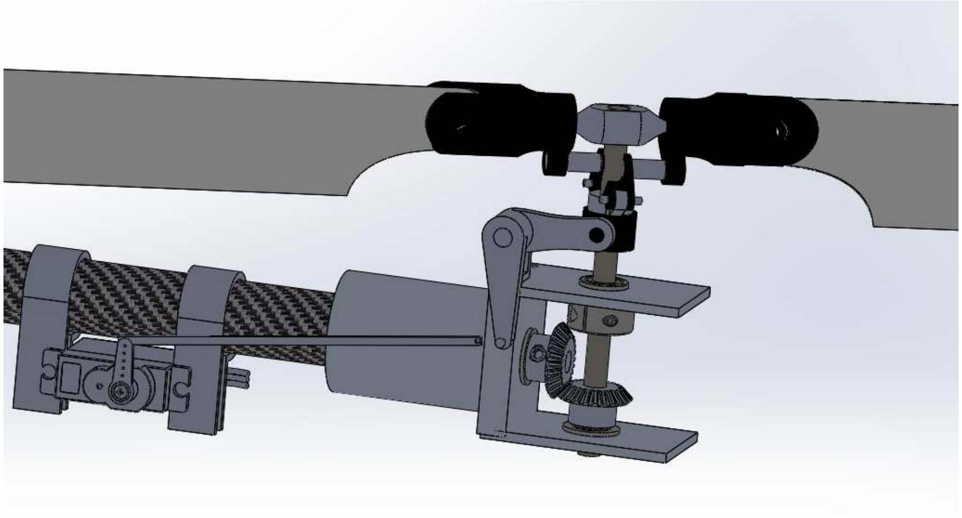

Figure 3. 6: A CAD drawing of a completed rotor assembly

Figure 3.7 shows A simple block diagram of the variable pitch quadcopter control system. The flight controller controls the ESC of the motor and rotor blade pitch servos. The ESC controls the rpm of the vehicle power plant, which controls the rotor rpm through the power transmission system. Besides, the flight controller directly controls the four servos which operate the blade pitch angle of the rotors. The single power plant variable pitch quadcopter controls its attitude by varying the pitch of the rotor blade. Increasing the power plant rpm will increase overall thrust of the quadcopter due to the fact that all rotors have the same rotational speed.

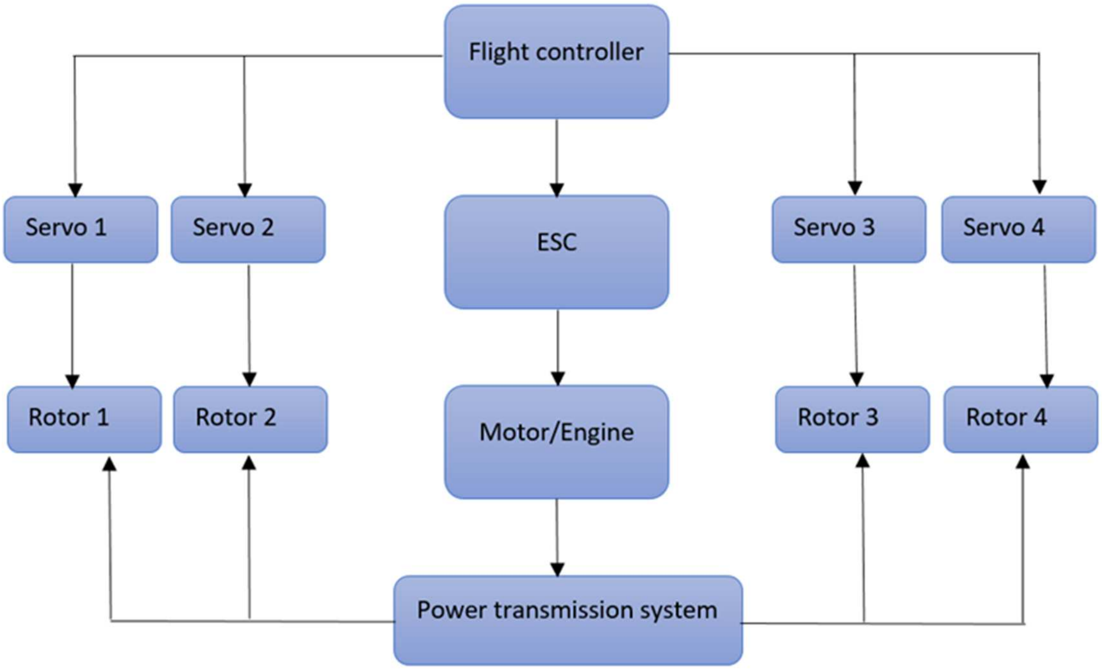

Figure 3. 7: A simple block diagram illustrates the control system of the variable pitch quadcopter

To move up and down, the vehicle will increase/decrease all rotors' pitch angle collectively. For pitch and roll, the vehicle will increase the rotor's pitch on one side and decrease the pitch on the other side. Figures 3.8a and 3.8b show the pitch and roll motion of the variable-pitch quadrotor. For the yaw motion, increasing the blade pitch for the diagonal rotors that have the same rotational direction and decreasing the blade pitch for the diagonal rotors that have the opposite rotation need to take place. This differential collective pitch will create more lift and drag on one set of diagonal rotors while creating a stronger torque of the diagonal rotors. This torque has the direction that is opposite to the rotor's rotation. Thus, the total torque acting on the vehicle is not balanced and the vehicle will yaw CW or CCW at its CG (Center of Gravity) that depends on the set of diagonal rotors which either increase or decrease pitch.

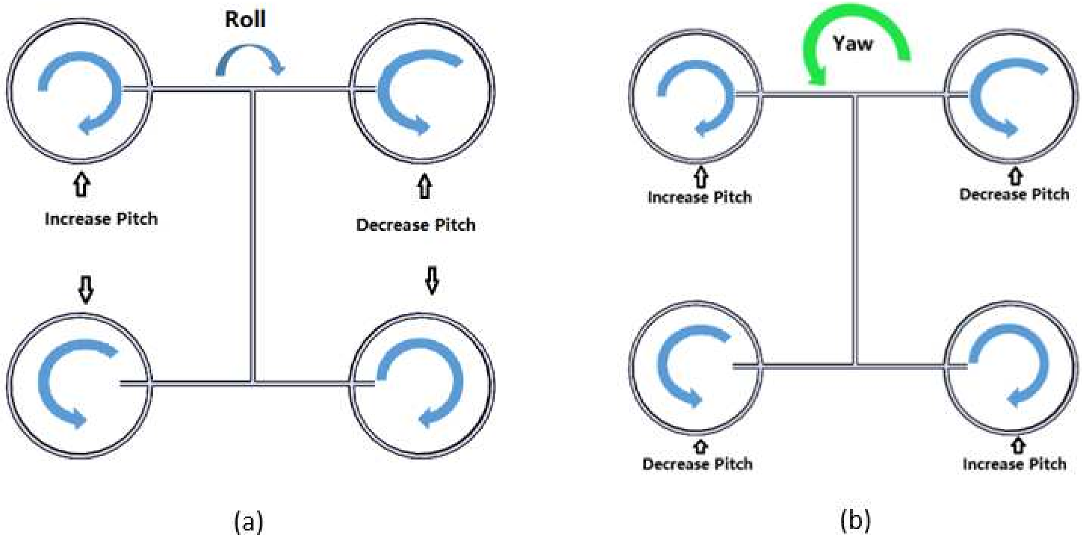

Figure 3. 8a and 3.8b: (a) A schematic drawing of Roll motion control. (b) A schematic drawing of yaw motion control.

CHAPTER IV

VEHICLE DESIGN

4.1 Finalized Design Concept

Figure 4.1 shows the first design of the electricity-powered variable-pitch quadcopter. Many parts of this quadcopter come from the previous gas-powered quadcopter projects such as rotor blades, servos, the carbon fiber body frame, pulley and belt, etc. This fact made the process of conducting the project easier because most of these parts have already been tested and analyzed by the previous senior design students [18] [20] and because it proved working. This also allowed me to have a rough estimation of the performance of this vehicle before getting into the detailed design of the vehicle.

Figure 4. 1: The first design of the electricity-powered variable-pitch quadcopter. The power transmission system from the motor to the main shaft is a gear-driven system

Figure 4. 2: The second design of the electric powered variable pitch quadcopter. The second design used the belt and pulley system to transfer the power from the motor to the main shaft.

Figure 4.2 shows the second design of the variable-pitch quadcopter. An electrical motor powers the central shaft by using the belt and pulley system. The only difference between the first and second design is the power transmission from the motor to the main shaft. The central shaft powers two differential gearboxes and transfers the power to the two rotor arm shafts that are perpendicular to the central drive shaft. The rotating arm supporting bracket assembly shown in Fig 4.3a was originally designed for the tilt rotor purposes. This design required the arm-supporting carbon fiber tube to be glued to the aluminum bracket tubing the inner wall. The outer wall diameter was slightly smaller than the housing bracket diameter. This allowed the arm-supporting carbon fiber tube to rotate freely around its axis, which caused the rotor to tilt either forwards or backwards. However, this could be fixed by using a few rubber bands that were wrapped around the aluminum bracket tubing, as shown in Fig 4.3b, so that after the bracket housing was closed and tightened by the bolts; the bracket housing could be pressed against rubber bands, and it created an additional friction force between the housing and aluminum bracket tubing. This friction force will keep an arm-supporting tube fixed in the supporting bracket. Also, the rubber band can act as a vibration dampener absorbing some vibration from the vehicle frame.

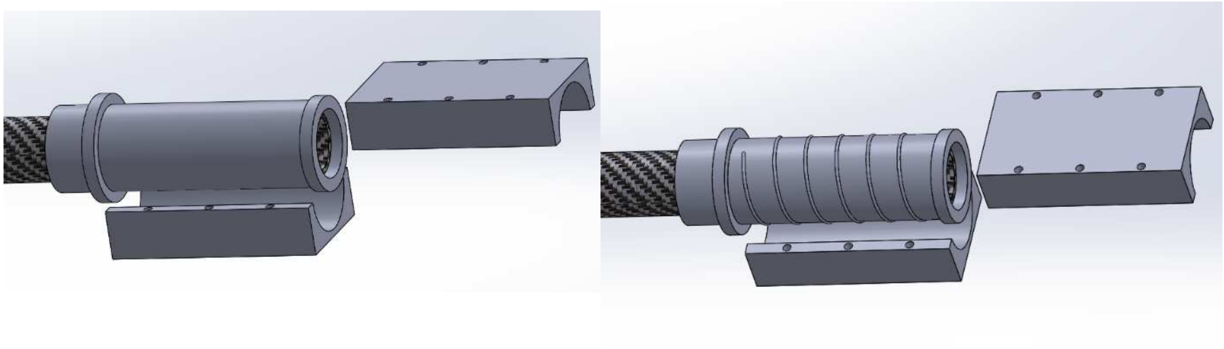

(a) (b)

Figure 4. 3: (a) variable tilt assembly without the rubber bands; this allowed the arm supporting tube to rotate freely; (b) variable tilt assembly with the rubber band wrapped around the aluminum bracket.

4.2 Vehicle Detail Design

The variable-pitch quadcopter requires a complex power transmission system; unlike the conventional quadcopter, this variable-pitch quadcopter uses a single electric motor to all four variable-pitch rotors through the complex power transmission system. Thus, all parts must be designed to work properly and to be able to stand the load from the electrical motor. So the first step is to figure out the aerodynamic loading of the rotor. This includes maximum lift, maximum torque, maximum RPM and maximum power consumption of the rotor which is powered by the given motor. These values can be calculated using the software called “Qprop” and “Xfoil”. After obtaining the maximum torque and RPM of the rotor, the second step is to calculate the stress and critical speed of drive shafts. Based on these two factors, the drive shafts selection can be chosen, based on the martial of the shaft, solid shaft or hollow tube, etc. The third step is to calculate the stress loads on the gearbox and to make sure that those bevel gears can handle the bending stress that affects the teeth and surface wear from an excessive contact stress. Next to this, there follows the analysis of the structures loading on the critical components of the vehicle such as the airframe, arm-supporting carbon fiber tube and landing gears, etc.

4.2.1 Analysis of Rotor Blade

The primary tool used for analyzing rotor aerodynamic loading is Qprop and XFLR5. The Qprop is a window command prompt program that was developed by Drela [23] from MIT. This program specializes in analyzing the performance of motor-driven propeller. Thus, it requires two input files to make this program work. One input file contains the blade aerodynamic properties, and the other is the motor characteristics file. The motor characteristic input file can be obtained from the motor manufactory company. The aerodynamic properties of blade can be provided by the XFLR5 software. This software is an advance version of Xfoil, and it is a great tool for calculating the aerodynamic coefficients of 2D airfoil and 3D wings.

In order to make the Qprop work, the first step is to use XFLR5 to generate the CL/CD graph and CL/α graph on the chosen airfoil, as shown in Figure 4.4a and 4.4b. Then it was necessary to read off the C_{L0}, $C_{L\alpha}$, C_{Lmin}, C_{Lmax}, C_{D0}, C_{D2u}, C_{D2l}, $C_L C_{D0}$ values and copy them to the input file. The definition of each terms is displayed in Table 4.1.

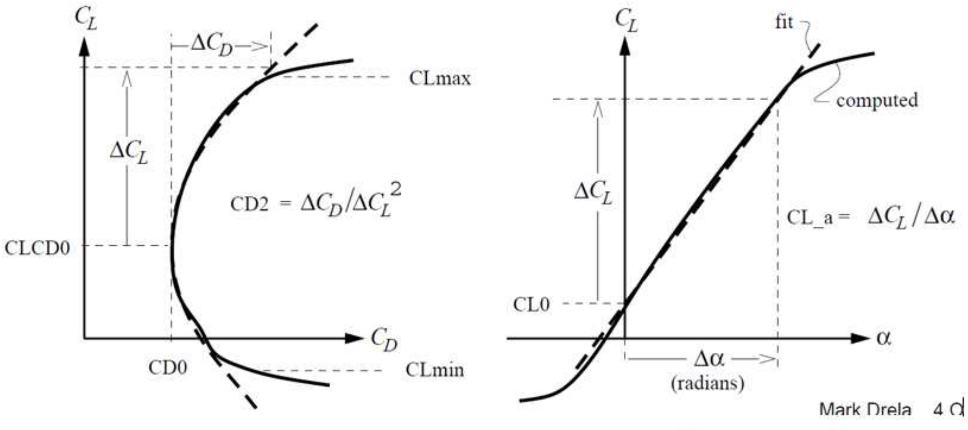

(a) (b)

Figure 4. 4a and 4.4b: (a) An example of a drag polar graph. (b) An example of a lift curve. Both graphs can be generated by using Xfoil or XFLR5.

Table 4. 1: Definition of each aerodynamic parameter. [24]

Aerodynamic Parameters	Definition
$C_L C_{D0}$	Lift coefficient at the minimum of drag coefficient
C_{D0}	Drag coefficient at the zero lift
C_{L0}	Lift coefficient at the zero angle of attack
$C_{L\alpha}$	Slope of the 2D lift curve
C_{Lmin}	It's the lift coefficient at L/D minimum of the angle of attack
C_{Lmax}	It's the lift coefficient at L/D maximum of the angle of attack
ΔC_L	It's the changing life coefficient value between the CLCD0 and C_{Lmax} / C_{Lmin}
ΔC_D	It's the horizontal distance between the CLCD0 and C_{Lmax} / C_{Lmin}
C_{D2u}	It's an upper value that takes into account the changes between CLCD0 and C_{Lmax}
C_{D2l}	It's a lower value that takes into account the changes between CLCD0 and C_{Lmin}

The rotor blade is going to be used on this variable-pitch quadcopter coming from the last gas-powered quadcopter project, as shown in Figure 4.5, which is a SAB0380R carbon fiber blade with the length of 12.5 inches from the tip to the root and 13.5 inch from the tip to the center of the rotor hub. This blade uses a symmetrical airfoil with a maximum thickness to chord ratio of 17%, which is a NACA 0017 airfoil. Assuming that the blades are spinning at 3000 RPM, the Mach number at the tip of blade is 0.31, and Reynolds number is about 241,000.

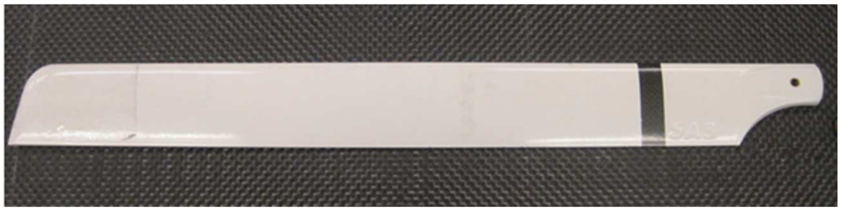

Figure 4. 5: SAB0380R carbon fiber blade [20]

Figure 4.6a, 4.6b and 4.6c are the Cl/Cd, Cl/Cd vs alpha and Cl vs alpha curves resulting from the XFLR5 airfoil analysis. Two different Reynolds numbers are used to help converge the calculation. The Cl vs alpha curve shows the airfoil stalls around 14 degree of the angle of attack. Since NACA 0017 is a symmetrical airfoil, by definition $C_L C_{D0}$ and C_{L0} are equal to zero. C_{D0} can be directly read off from Fig. 4.6a, which is 0.01096. C_{Lmax} can be obtained from Fig. 4.6b and 4.6c, which is 0.9318. C_{Lmin} is -0.9318 due to the symmetrical airfoil. C_{D2l} and C_{D2u} can be calculated by using the equation provided below:

$$C_{D2u}\,, C_{D2l} = \frac{\Delta C_D}{\Delta C_L^2} \tag{4.2.1}$$

The difference between C_{D2l} and C_{D2u} is that C_{D2l} is a value that represents the changing lift from $C_L C_{D0}$ to C_{Lmin}, and C_{D2u} is a value that represents the changing lift from $C_L C_{D0}$ to C_{Lmax}. The same thing refers to the ΔC_D. Since the airfoil is symmetrical, C_{D2l} and C_{D2u} are equal to each other. ΔC_L and ΔC_D can be read directly from XFLR5. Therefore, the C_{D2l} and C_{D2u} are calculated to be 0.00888.

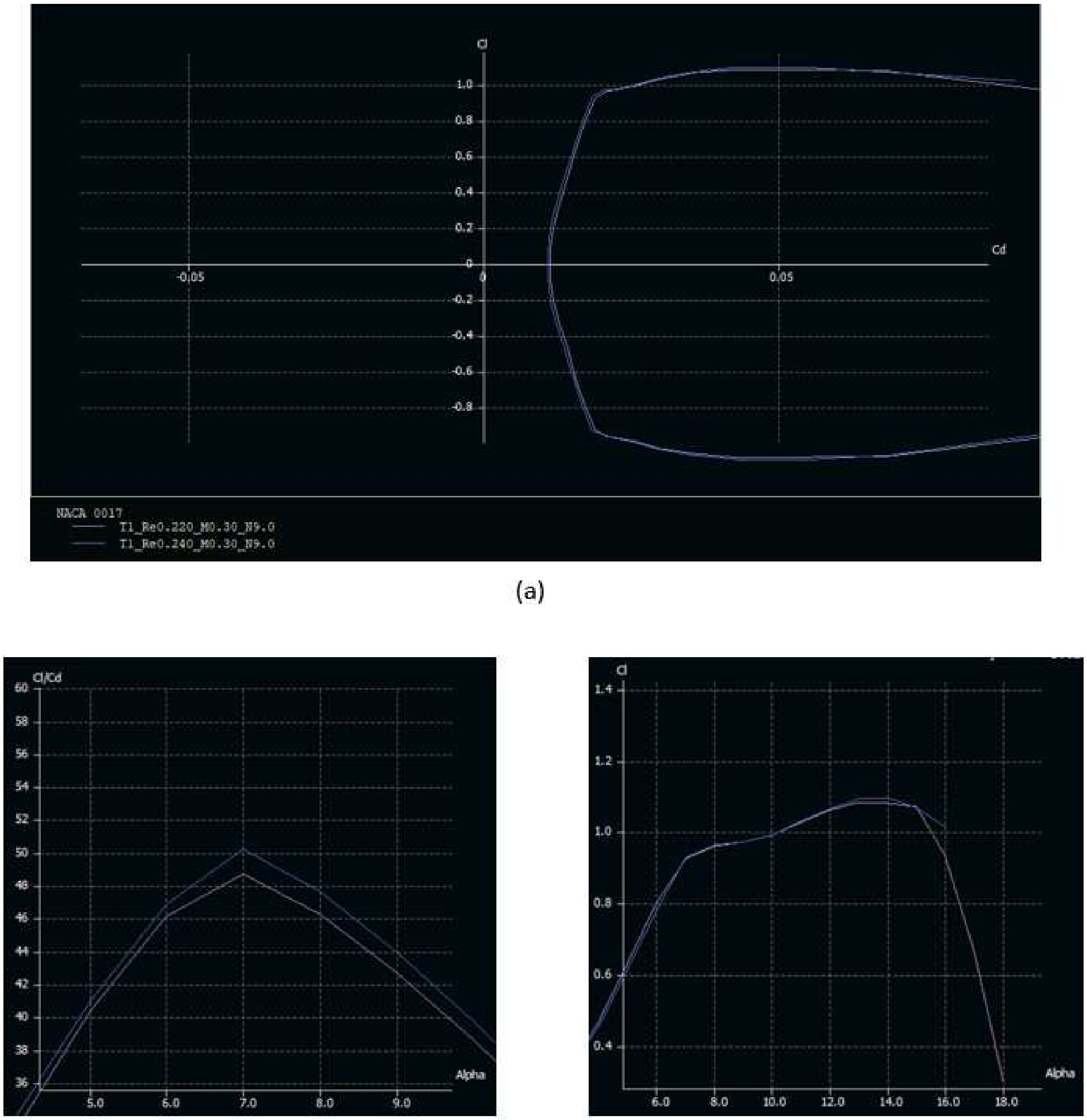

(a)

(b)

(c)

Figure 4. 6a, 4.6b, 4.6c: The Cl/Cd curve of NACA 0017. (b) Cl/Cd vs alpha curve of NACA 0017. (c) Cl vs alpha curve of NACA 0017. Two Reynolds number are used in the graphs. RE=22000, 240000

Table 4. 2: Blade Aerodynamic Coefficients

C_{L0}	$C_{L\alpha}$	C_{Lmin}	C_{Lmax}	C_{D0}	C_{D2u}	C_{D2l}	$C_L C_{D0}$	$REref$	$REexp$
0	6	-0.9138	0.9138	0.01096	0.00888	0.00888	0	241,000	-0.3

Table 4.2 shows the aerodynamic coefficients for the NACA 0017 airfoil, which were obtained from XFLR5. Fig. 4.7 shows the input file for the Qprop. The $REref$ is the original reference to Reynolds number that is used in XFLR5; the $REexp$ is a factor for adjusting blade cross-sections that experienced a different Reynolds number compared to the original reference value. For a large rotor with a strong turbulent flow, the use –0.3 for $REexp$ is a good estimation.[23]

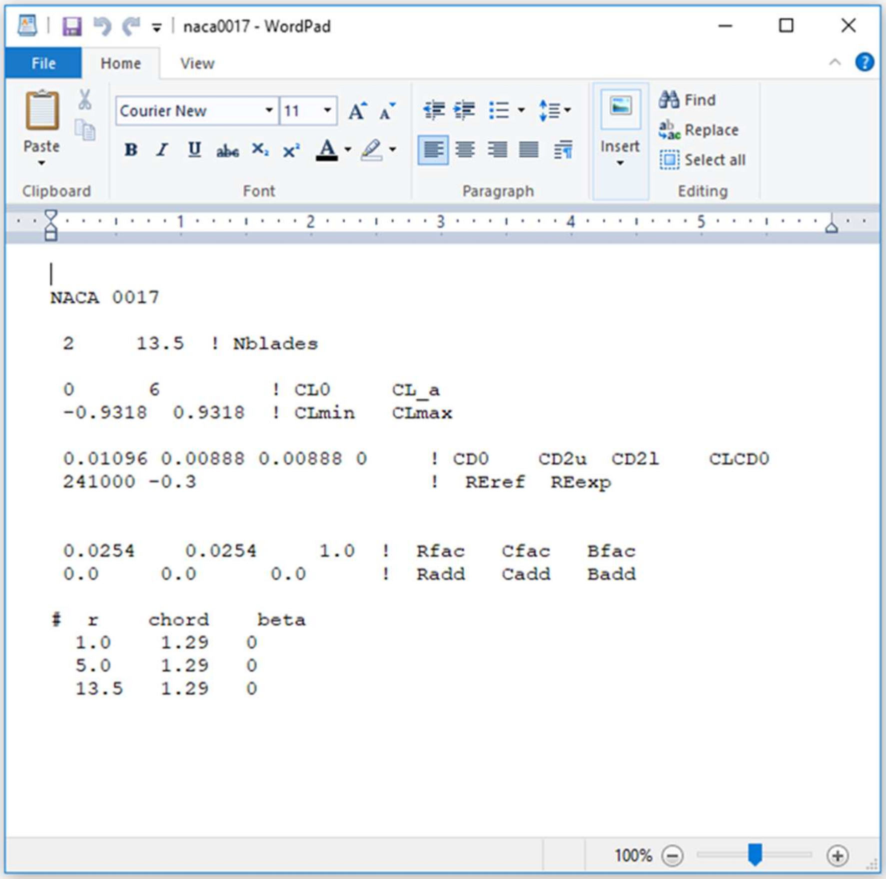

```
NACA 0017

 2     13.5  ! Nblades

 0      6         ! CL0     CL_a
 -0.9318  0.9318  ! CLmin   CLmax

 0.01096 0.00888 0.00888 0      ! CD0    CD2u  CD2l    CLCD0
 241000 -0.3                    !  REref  REexp


 0.0254    0.0254     1.0  !  Rfac   Cfac   Bfac
 0.0      0.0      0.0      !  Radd   Cadd   Badd

#  r    chord    beta
  1.0    1.29   0
  5.0    1.29   0
  13.5   1.29   0
```

Figure 4. 7:Qprop rotor input file

Electric Motor

The motor selected for this vehicle is a Hacker A60-20M brushless motor, as shown in Fig. 4.8. A typical brushless motor has a higher power and torque, compared to a brushed DC motor with the same weight. This motor has the maximum power of 2,200 watts and is rated 170 Kv [25]. Although this motor has a pretty low RPM, its 12 poles indicate the fact that this motor is a high torque motor, which is ideal for the variable pitch quadcopter.

Figure 4. 8: Hacker A60-20M brushless motor. [55]

Table 4.3 shows the factory specifications for this electrical motor. However, the maximum torque was not given in the specification. According to lon [56], the equation from below can be used for calculating the motor torque.

$$K_T = \frac{30}{\pi * K_V} \tag{4.2.2}$$

$$T_m = K_T * (I - I_0) \tag{4.2.3}$$

The K_T is the motor torque constant, K_V is the motor speed constant, I is the peak current, and I_0 is the idle current. Using the equations from above, the maximum torque was calculated to be 3.03 N-m.

Table 4. 3: Motor Specification [25]

RPM Volt KV	170
Max Watts	2,200
Max RPM	7,000
Timing	25°
Poles	12
Idle Current	1.7
Resistance	32
Weight (grams)	760
Length Metric	70
Diameter Metric	59
Shaft Diameter	8mm
Prop Mount Type	Threaded shaft with mounting hardware included
Product Place Of Manufacture	China

Figure 4.9 shows the input for the motor file. The information required from the motor is the resistance of the motor, the idle current of the motor and motor Kv. These values can be found in Table 4.3 presented above.

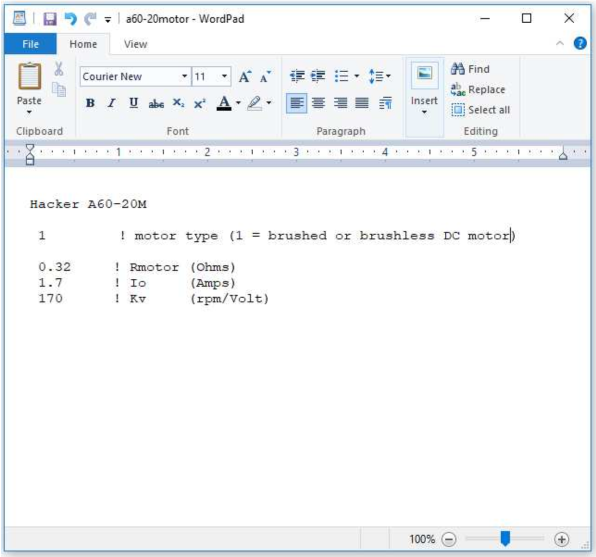

```
Hacker A60-20M

 1         ! motor type (1 = brushed or brushless DC motor)

 0.32     ! Rmotor (Ohms)
 1.7      ! Io     (Amps)
 170      ! Kv     (rpm/Volt)
```

Figure 4. 9: Qprop motor input file

After obtaining the propeller input file and motor input file, Qprop can be used for predicting the performance of the motor-driven propeller. Qprop is a very useful tool to determine the load torque from the rotor drag, thrust and power consumption from the rotor as a function of blade pitch angle α and rotor RPM. Fig. 4.10 shows the output graph from the Qprop. The solid lines in colors such as green and blue, etc. are the constant thrust lines, and each line has a different thrust value. The lowest constant thrust line started at 20 N, and the highest value of constant thrust line stopped at 45 N. The black dash lines are the constant rotor rpm lines. Each dash line increased by 500 rpm value. The red horizontal line that was slightly above 500 Watts is the power limit for each rotor's power consumption. The maximum power which can be put out by the electric motor is 2200 watts, which means that for each rotor, the power is limited to 550 watts. So any thrust lines and RPM lines that are above the 550 watts' limit will exceed the rotor's operation range. The major advantage of the variable-pitch rotor is that lift is a function of RPM and pitch angle α; this gives the variable-pitch rotor ability to operate anywhere on this graph as long as within the operation limit of the rotor. This can help the quadcopter to hover more efficiently at a particular combination of RPM and pitch angle.

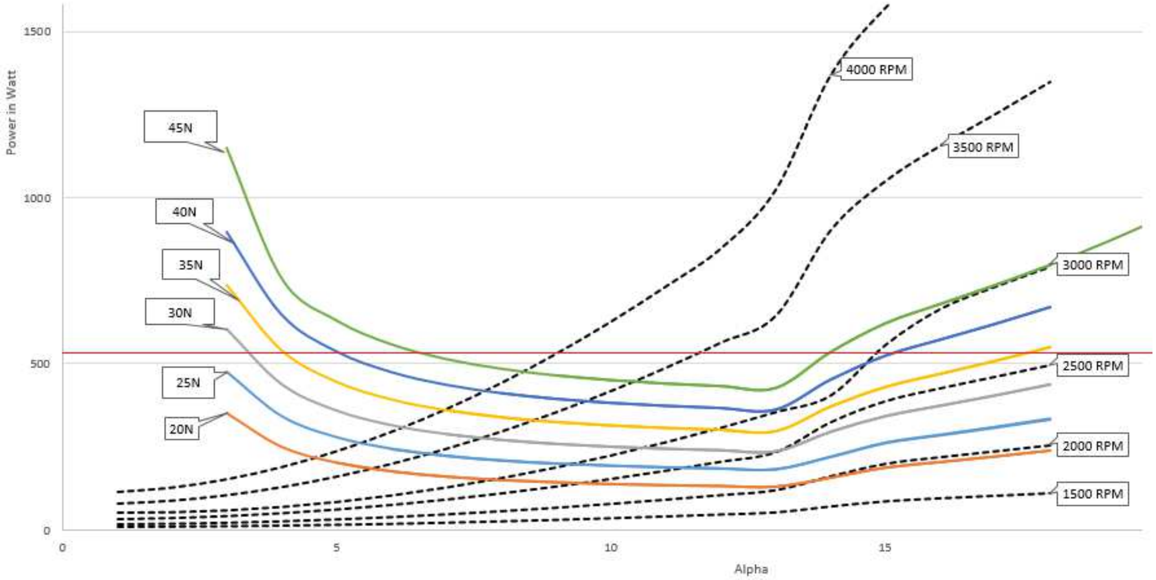

Figure 4. 101: The constant thrust lines are displayed with solid lines. The constant RPM lines are the dash lines.

Figure 4.10 from above shows the limitations of a 13.5-inch rotor blade that is powered by the Hacker A60-20M motor. The maximum RPM of Hacker A60-20M electric motor is about 7000 RPM. The power transmission system for this vehicle has a gear reduction ratio of 1:2.25 from the motor to the rotors. This reduces the rotor maximum RPM to 3100 RPM. The maximum thrust generated by the rotor is about 40 N or 9 lbf at 14 degrees of pitch angle. Any higher thrust will stall the blade. This rotor blade used NACA 0017 airfoil and was based on the XFLR5 airfoil analysis; this airfoil stalled at 14 degrees of the angle of attack. That is why all the thrust and RPM curves suddenly changed the slope after passing the 14-degree angle of attack; power consumption increased dramatically as well.

The torque curve created by the rotor drag at 3000 RPM is shown in Figure 4.11. Based on this graph, the torque value observed before the rotor stalls is about 1.28 N-m. So the total torque that is required to power all four rotors at maximum RPM is about 5.12 N-m. The maximum torque that is provided by the motor is only 3.03 N-m, but with the gear reduction system, the motor torque is multiplied by 2.25, which is about 6.8 N-m. Thus, it means that the motor will not stall under the torque load due to the rotor drag.

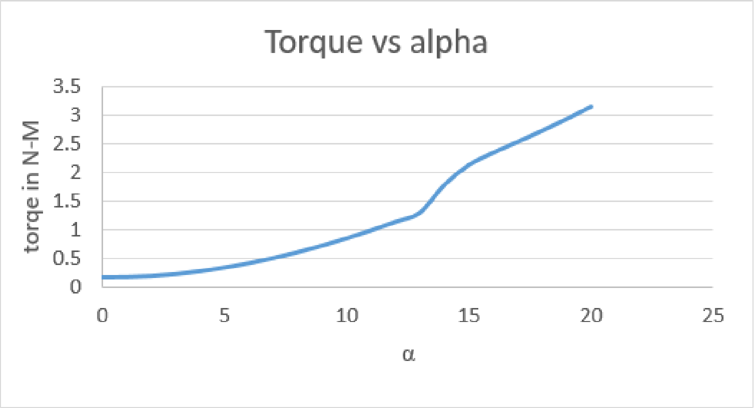

Figure 4. 11: Torque curve for 3000 RPM

4..2.2 Blade deflection

The blade deflection will determine the minimum height between the tip of the rotor and the supporting arm. The deflection happens when the blade produces a lift. In the case of a conventional quadcopter, it is unlikely for the blade to strike the supporting arm during the flight because the direction of blade deflection is always upward. For a variable pitch quadcopter, it is actually capable of producing a negative lift by turning the blade pitch angle into the negative angle of attack. This should allow the quadcopter to be used for aggressive maneuvers and aerobic flights. This variable pitch quadcopter is designed for a long-endurance flight so that it would not be able to fly upside down; but since this is a large quadcopter and since it has a large moment of inertia, using the negative thrust could help people increase the maneuverability of the quadcopter.

The SAB0380R blade is made of carbon fiber composite material. Each blade weights 20 grams. The easiest way to analyze the blade deflection is to use the Solidworks Simulation, since we don't know what materials were exactly used for this blade. The Solidworks Simulation can predict the blade deflection by applying similar materials with similar properties of the real blade material.

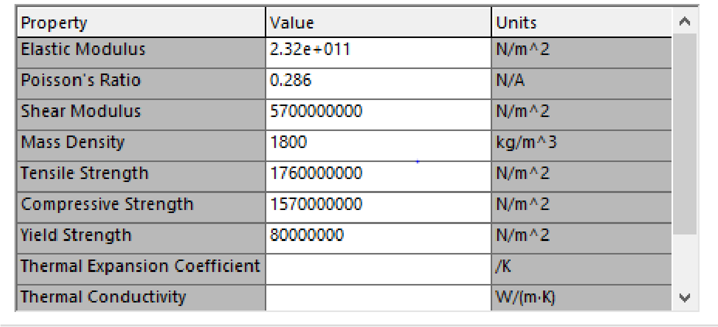

Property	Value	Units
Elastic Modulus	2.32e+011	N/m^2
Poisson's Ratio	0.286	N/A
Shear Modulus	5700000000	N/m^2
Mass Density	1800	kg/m^3
Tensile Strength	1760000000	N/m^2
Compressive Strength	1570000000	N/m^2
Yield Strength	80000000	N/m^2
Thermal Expansion Coefficient		/K
Thermal Conductivity		W/(m·K)

Figure 4. 12: The 3K carbon fiber composite material properties

Figure 4.12 shows the 3K carbon fiber material properties [27]. This is the most popular type of carbon fiber used for making RC airplane and helicopter parts due to its light weight and high strengths. In order to predict the simulation more accurately, a real bending test was performed on this blade to serve as a model for designing the blade in Solidworks. Figure 4.13 shows the actual blade deflection testing. A water bottle weight is about 1.6 lbs, and it hangs at 75% of the blade's length. Two marks on the paper indicated the tip deflection under 1.6 lbs of load, which is about 1.2 inch or 30 mm. The blade lift distribution is not uniform throughout the blade length. This is due to the tangential velocity along the blade sections increasing from the root to the tip, which causes more lift to generate near the rotor tip and less lift to generate at the root. Figure 4.14 shows a typical rotor lift distribution [28]. So by summing all the force at 75% of the blade length, it is possible to predict the blade deflection in a more reliable way.

Figure 4. 13: Blade deflection test

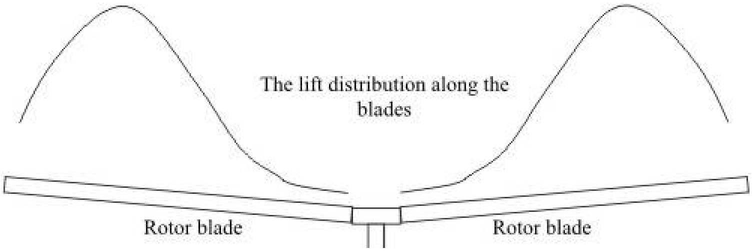

Figure 4. 14: Lift distribution along the helicopter rotor blade.[28]

Figure 4.15 shows the Solildworks blade model which has the similar stiffness, compared to the real blade. The green arrow indicates the blade which was fixed on the end. The purple arrow indicates a 1.6 lbs of load acting at 75% of the blade. The result shows that the blade tip deflection is about 29 mm, which is very close to the actual value. The highest deflection occurs at a low rotor RPM with a high blade pitch angle. Based on the Qprop ouput graph from above, the lowest RPM for this quadcopter to takeoff is at 1800 with 4.2 lbs of thrust per rotor. The highest lift occured at 3000 RPM with 10 lbs of thrust. Both conditions needed to be checked.

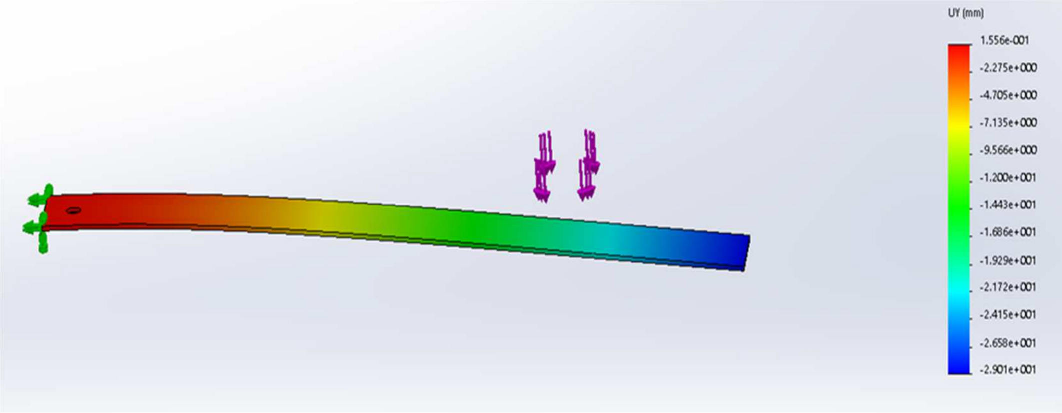

Figure 4. 15: FEA simulation of the blade deflection test in Solidworks

Figure 4.16 shows the deflection of blade at the 1800 RPM with 2.1 lbs of force acting downwards on the blade. The centrifugal force that generated at 1800 RPM is acting along the blade and pulling the blade outward. This changed the stiffness of the blade and made the blade more rigid. Therefore, it is possible to say that this simulation requires a non-linear finite element analysis (FEA) to compute the displacement of the blade. The result shows that the displacment at the tip of the blade is about 4.6 mm.

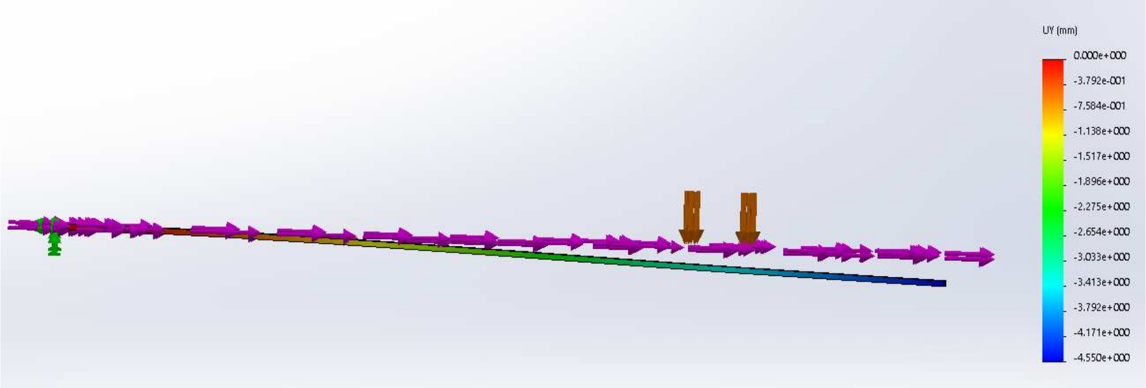

Figure 4. 16: Non-linear FEA simulation of blade deflection at 1800 RPM with 2.1 lbs of downward force acting on the blade.

Figure 4.17 illustrates the blade deflection at the 3000 RPM with 5 lbs of force acting downward on the blade. The result shows that the blade tip’s displacement is about 4.4 mm, which is lower than the last simluation. This is because the centrifugal force at 3000 RPM is much greater than the 1800 RPM. The greater of the centrifugal force acting on the blade, the less of the blade deflection can be observed. Therefore, the maximum blade deflection occurs at the lowest RPM of the vehicle. This varible ptich quadcopter has a 2.5 inch of clearance between the rotor tip and arm supporting tube. So there is no way the blades will strike the boom.

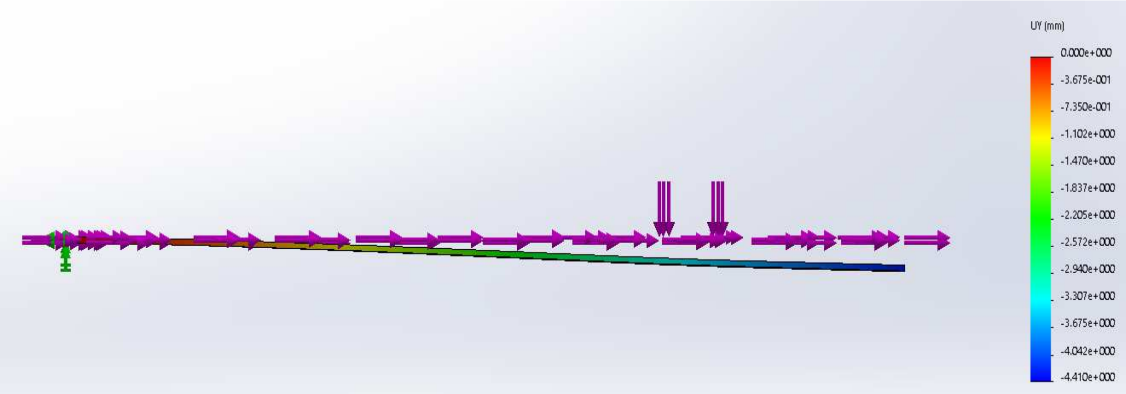

Figure 4. 17: Non-linear FEA simulation of blade deflection at 3000 RPM with 5 lbs of downward force acting on the blade.

4.2.3 Power Transmission System

The power transmission system design for this varibale pitch quadcopter is using a single electric motor to power all four rotors. Fig. 4.18 shows an example of the schema of the power transmission system from the second design.

Figure 4. 18: A schematic drawing of power transmission system from the second design

In the second design, the electric motor uses the pulley and belt system to transfer the power from motor shaft to the main shaft. At each end of the main shaft, the bevel gearbox is used to distribute power from the main shaft to the two rotor arm shafts that are twisted 90 degree towards the main shaft. All bevel gears are identical, and no gear ratio is between them. The motor has a maximum RPM of 7000 and driving a pulley and belt system with a gear ratio of 1:2.25, which brings down the maxinum rotor RPM to 3000. Based on the Qprop analysis, it is possible to say that it only takes about 1900 RPM to lift off the ground; so maximum 3000 RPM can provide plently thrust for this quadcopter.

Differential Gearbox

The gearbox is made of Delrin Acetal material, which has excellent machinabilty and high strength and stiffness properites. The gearbox is 1.8”(width) x 1.2”(height) x 1.6”(length) rectangle shape, as shown in Fig. 4.19. The front and back walls of the gearbox have a flange bearing which is pressed fitted and which provides support for the main shaft. The left and right walls also have a flange bearing them press-fitted and supporting the arm shaft.

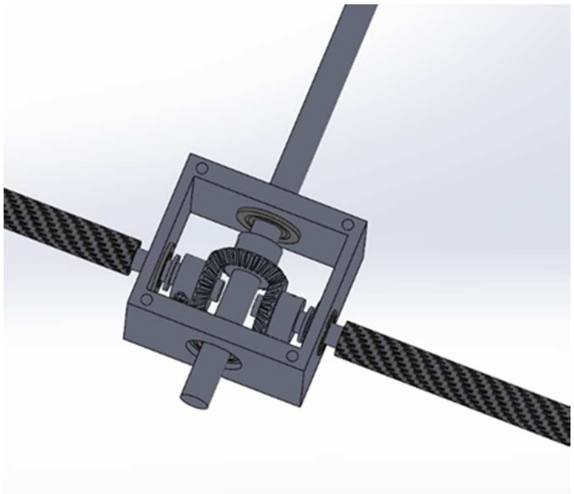

Figure 4. 19: CAD drawing of the differential gearbox design

The bevel gears that are used in the gearbox are straight bevel gears with pitch angles of exactly 90 degrees towards each other. They all have a 24 teeth number and the same ptich diameter. These bevel gears have two different bore diameters; the one on the main drive shaft has a bore diameter of 5/16”. The one on the arm shaft has a bore diamter of 6 mm. They all are secured on the steel shaft by using a set screw. A few vey thin shims that are placed between the gear and flange bearing to fill the gap and transfer some of the axial load from the arm to the bearing. The space inside of the gearbox must have a width distance that is greater than 0.658” in order to fit the bevel gears inside; Fig. 4.20 demonstreates this dimension.

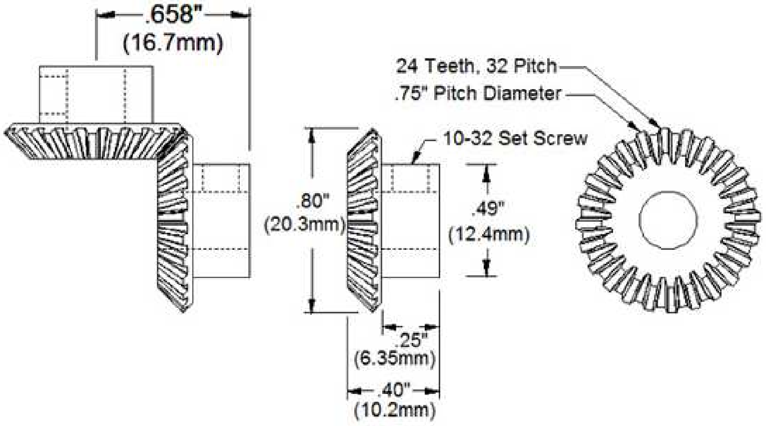

Figure 4. 20: Dimension of the bevel gear mesh.[29]

Motor Mount

The second design of the varible pitch quadcopter uses a pulley and belt to transfer the power from the motor to the main drive shaft. The timing belt that is used in this vehicle is a AT5 340; it has a pitch number of 5 mm, and its length is 340 mm. The motor-mounted height depends on the gear ratio of the driver pulley and driven pulley, since the belt length is fixed. The drive pulley is a T5 type of timing pulley that has a diameter of 24.6 mm with 16 teeth, and a T5 type of the driven pulley has a diameter of 57.3 with 36 teeth. Fig. 4.21 shows how to calcaulate the distance between two pulleys [30]. This distance will determine the heights which the motor mount needs to have.

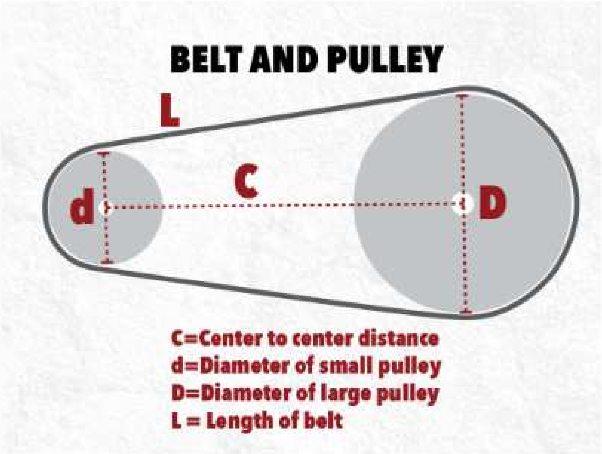

$$\frac{b+\sqrt{b^2-32\,(D-d)^2}}{16}=C \qquad \text{Whereas } b = 4L - 6.28\,(D+d)$$

Figure 4. 21: The distance between two pulleys can be calculated using the equation presented above. [30]

Based on the equation from Fig. 4.21, it is possible to conclude that the distance between the driver and driven pulley is 104.4 mm. The motor mounts are of two L shape Delrin Acetal material, and they have 0.3” wall thickness, which provides enough rigidity for the motor mount. The dimension of the motor mounts is shown in Fig. 4.22.

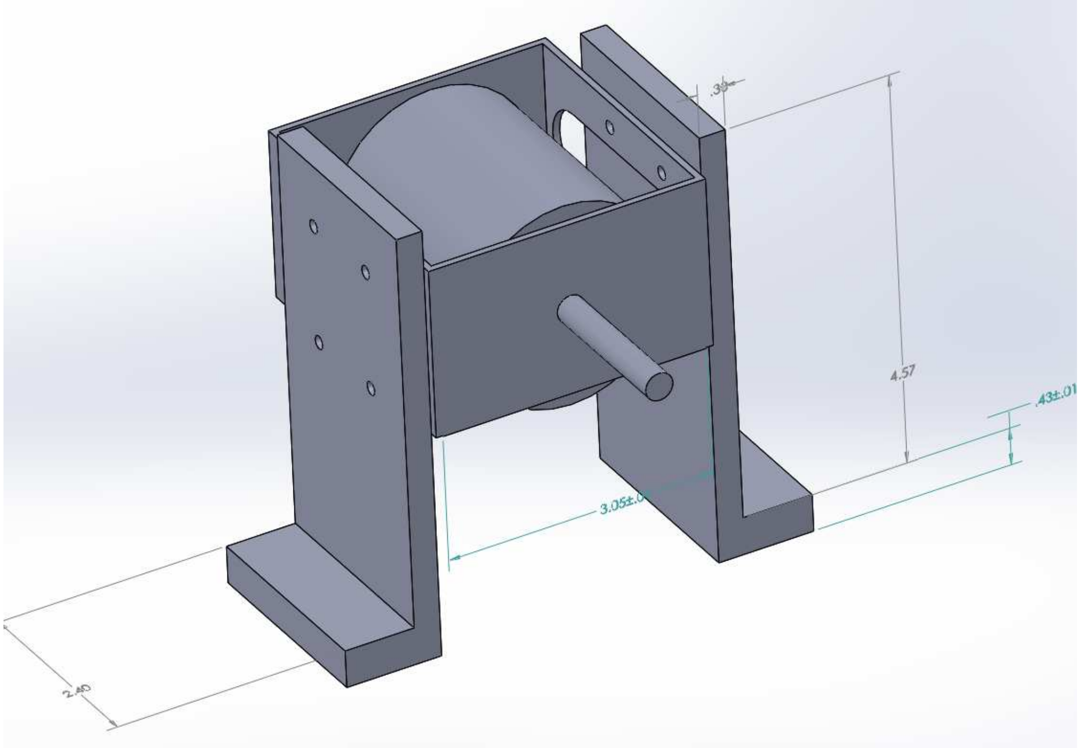

Figure 4. 22: The 3D CAD drawing of the motor mount with the dimension displayed. The unit is measured in inches.

The timing belt pulley system is different from the regular flat belt pulley system. The timing belt pulley has a fixed number of teeths, – just like the sprokcet gear which does not require the initial tension on the belt. The belt tension is only pulling on one side of the timing belt. The tensile force on one side of the belt is trying to pull the motor shaft downwards. If the shaft is only supported at one end, this will cause the tip of shaft to deflect downwards and cause the vibrations of the system. Therefore, the shaft must be supported on the both end in order to minimize the shaft deflection. Fig. 4.23 shows the motor shaft was supported by a bearing mount assembly. This bearing mount provides support at the tip of the motor shaft. There are two parts in the bearing mount assembly. The top part is a bearing mount which is made of aluminium and which uses a screw to tighten the bearing housing to secure the bearing. The lower part of the bearing mount is made of Delrin Acetal material, and it is secured to the bearing mount that is sandwiched between the top and bottom of the quadcopter body frame panels. The bearing mount and base are joint by two pieces of alumimou bar with screws. The hole for the screws is slightly bigger so that its top part can adjust the height to match the motor shaft height before tighterning the screws.

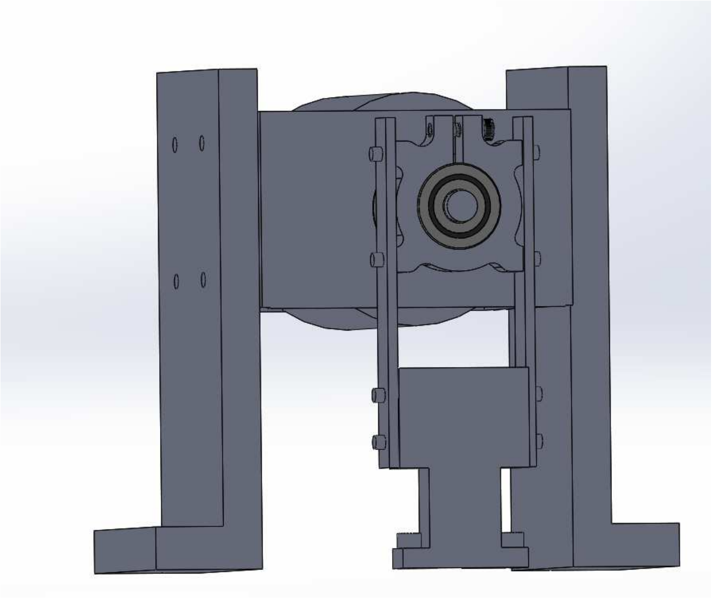

Figure 4. 23: 3D CAD drawing of motor shaft is supported by a bearing mount at the tip of the shaft.

The equation from Fig. 4.24 is used for calculating the both end-supported shaft deflection with a single load acting in the middle of the shaft [31]. The variables for calculating the shaft deflection are demonstrated in Table 4.4.

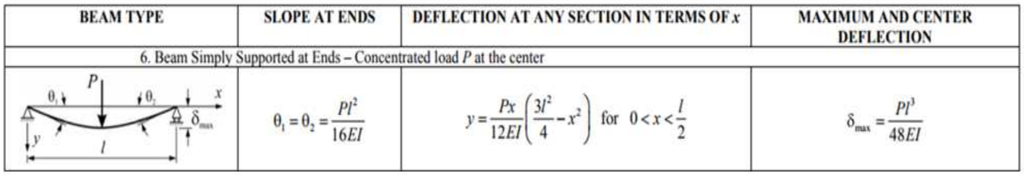

BEAM TYPE	SLOPE AT ENDS	DEFLECTION AT ANY SECTION IN TERMS OF *x*	MAXIMUM AND CENTER DEFLECTION
6. Beam Simply Supported at Ends – Concentrated load *P* at the center			
	$\theta_1 = \theta_2 = \frac{Pl^2}{16EI}$	$y = \frac{Px}{12EI}\left(\frac{3l^2}{4} - x^2\right)$ for $0 < x < \frac{l}{2}$	$\delta_{max} = \frac{Pl^3}{48EI}$

Figure 4. 24: Concentrated load at the midspan of the shaft with both end supported. [31]

In Table 4.4, P is the applied load in force. The force P = T/R; T is the maximum torque from the motor, and R is the radius of the driver pulley. E is the young's module of carbon steel, L is the length of the shaft, and I is the moment of the inertia of shaft. The maximum motor shaft deflection is δ_{max} = 0.0153 mm. This deflection is so small that it almost has no impact on vibration.

Table 4. 4: The variables for calcauting the shaft deflection

T (N/m)	R (m)	P (N)	L (m)	E (pa)	(m^4)
6.8	0.0123	552.8	0.0381	2.07E+11	2.0106E-10

Belt Selection

It is very important to have a proper timing belt selected for the power transmission system. If the belt type is different from the pulley type, this will cause the belt to slip and wear out the teeth on the belt. Fig. 4.25 shows the different types of belt tooth profile and dimensions.

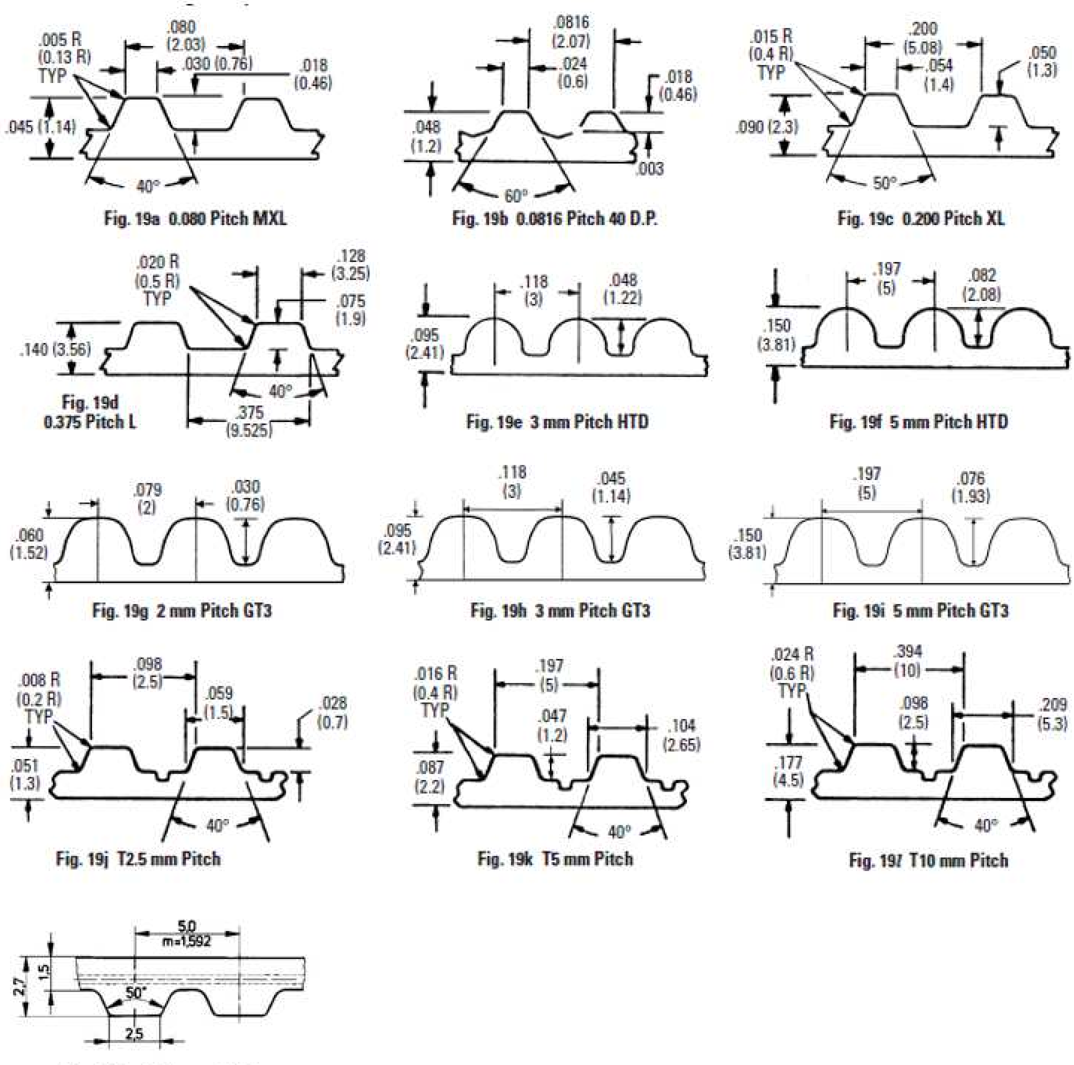

Fig. 19a 0.080 Pitch MXL

Fig. 19b 0.0816 Pitch 40 D.P.

Fig. 19c 0.200 Pitch XL

Fig. 19d 0.375 Pitch L

Fig. 19e 3 mm Pitch HTD

Fig. 19f 5 mm Pitch HTD

Fig. 19g 2 mm Pitch GT3

Fig. 19h 3 mm Pitch GT3

Fig. 19i 5 mm Pitch GT3

Fig. 19j T2.5 mm Pitch

Fig. 19k T5 mm Pitch

Fig. 19*l* T10 mm Pitch

Fig. 19m AT5mm Pitch

Figure 4. 25: Different types of the belt tooth profile [38]

Some of the belts are designed for a light load, and some of the belts are designed for the heavy power transmission. For example, most of the XL, L, H, XH, T type of belts are used for conveying a light load. AT, STD, HTD, and GT3 types of belts are used for the power transmission purpose. Fig. 4.26 shows the recommended belt selection, based on the HP and RPM of the operation condition.

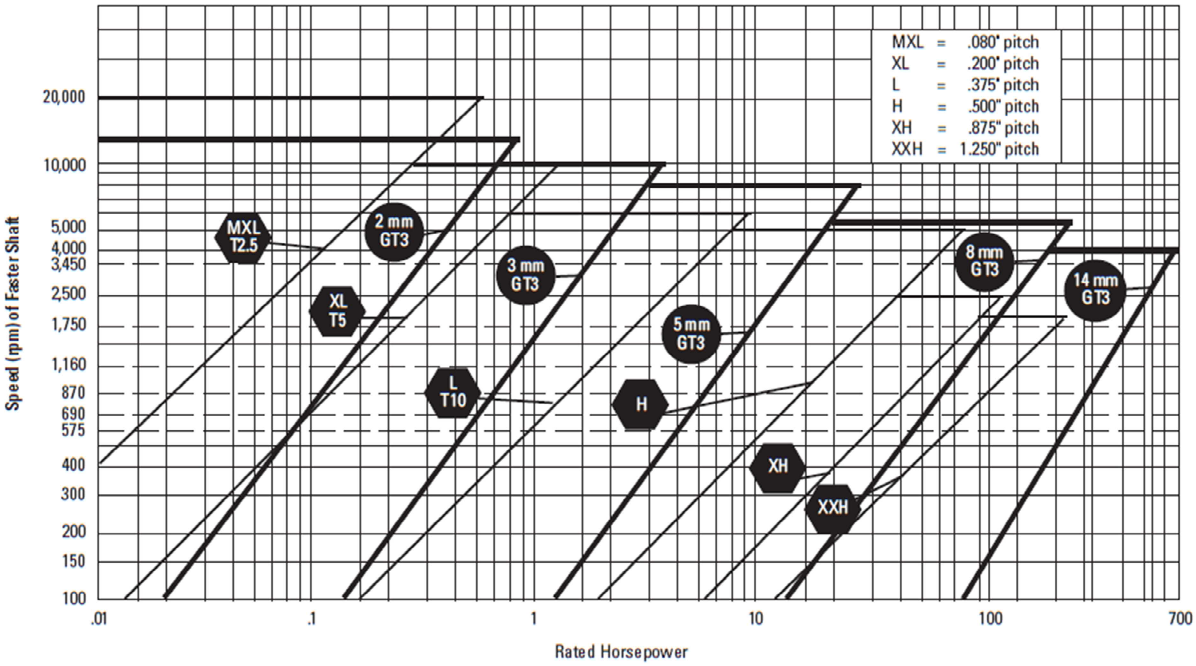

Figure 4. 26: Recommended power range for different types of pulleys [38]

This quadcopter used AT5 belts for transferring the power from the motor to the main shaft. The maximum allowable tensile load on the belt cross section depends on the belt manufacture data sheet. Table 4.5 shows the allowable tensile load on the belts having a different width.

Table 4. 5: Allowable Tensile load on different belt width [39]

Belt width in mm		6	10	16	25	32	50	75	100
AT 5	BRECO M		560	1260	1680	2240	3500		
	BRECO V		280	630	840	1120	1750		
	BRECOFLEX		490	840	1400	1890	3010	4620	6160
T 5	BRECO M	180	300	540	840	960	1260		
	BRECO V	90	150	240	420	480	630		
	BRECOFLEX	180	330	570	930	1200	1920	2940	3930

BRECO M = Open length belting BRECO V = Joined belts BRECOFLEX = Truly endless belts

The torque on the motor can be calculated using equation from Shigley's Mechanical Engineering Design book [32] in below

$$T = \frac{30P}{\pi * RPM}$$

where T is the torque in N-m, and P is the power in Watt. The lower the rpm, the higher the torque is required.

The rotor speed is typically operating around 2600 rpm, but it could drop below 2000 rpm if too much load is applied. At the rotor speed of 2000 rpm, motor speed is about 4500 rpm. Using the equation presented above, it is possible to find out that the torque is about 4.67 N-m. The tensile load on the belt can be calculated using the equation demonstrated below:

$$F = \frac{T}{R},$$

where F is the tensile force, T is the torque from the motor, and R is the radius of the motor pulley. 4.67 N-m/ = (0.012 m) = 389 N. The AT5 belt that was used on this quadcopter has 16 mm belt width, which has an allowable tensile load of 840 N. The maximum tension on the belt is far less than the allowable tension of the belt. So this belt should not stretch under the operating load.

4.2.4 Drive Shaft Stress Analysis

Rotor Arm Shaft Design

When designing the arm shaft, two types of shafts could be used for the transmission system. One of them is a 6 mm carbon steel solid shaft, and the other one is a 6 x 8 mm carbon fiber tube, as shown in Fig. 4.27.

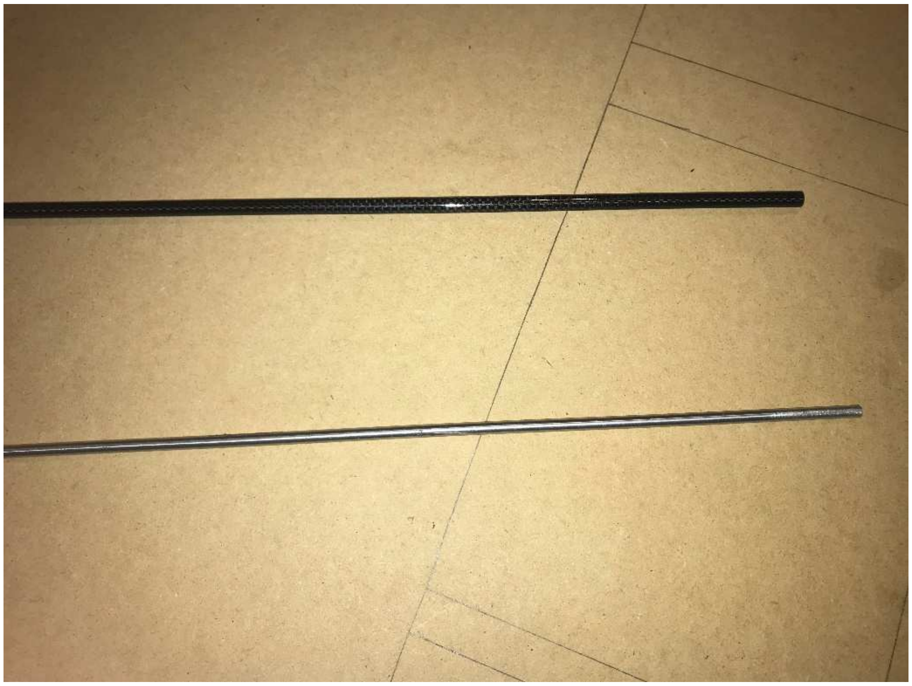

Figure 4. 27: The carbon fiber shaft is on the top, and the solid steel shaft is at the bottom.

A single 6 mm steel shaft weights about 135 g or 0.3 lbs, and the 6 x 8 mm carbon fiber tube weights about 19 g or 0.042 lbs. For designing a large variable pitch quadcopter, it is important to keep the weight of vehicle as low as possible. So the best way is to choose materials that have a high strengh per weight ratio; carbon fiber is the best option for that. So by choosing the carbon fiber shaft, it could be possible to save about 1.1 lbs of the structure's weight for the vehicle. However, this carbon fiber shaft has only 500 mm in length, and its outer diameter is 8 mm, which can not fit into a 6 mm bore bevel gear. The desired shift lentgh is 600 mm; thus it needs to be modifed before it can be actually used. The gearbox design requires the bevel gear to use a set screw to be locked on a drive shaft, as shown in Fig. 4.28.

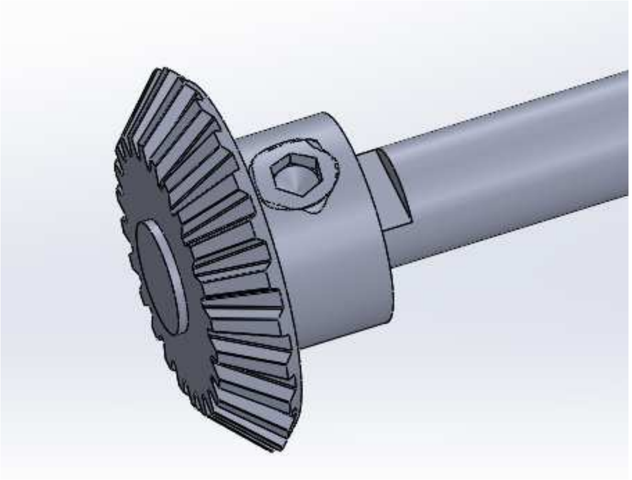

Figure 4. 28: Example of using a set screw to mount the bevel gear on the shaft.

After the set screw has been tightened, it creates a compressional force against the drive shaft surface. This should be fine for the steel shaft due to the steel shaft which is solid and which has a high compression strengh, but for the carbon fiber shaft which is made of a hollow tube having 1 mm of thickness, the set screw could easily crash through the tube. Thus, it requires a piece of a short steel rod that can be inserted into the end of the carbon fiber shaft so that overall length can increase up to 600 mm and bevel gear can be mounted onto the steel rod of the carbon fiber shaft. The steel rod will be bonded to the carbon fiber tube by using epoxy. Fig.4.29 shows the final design of the carbon fiber shaft.

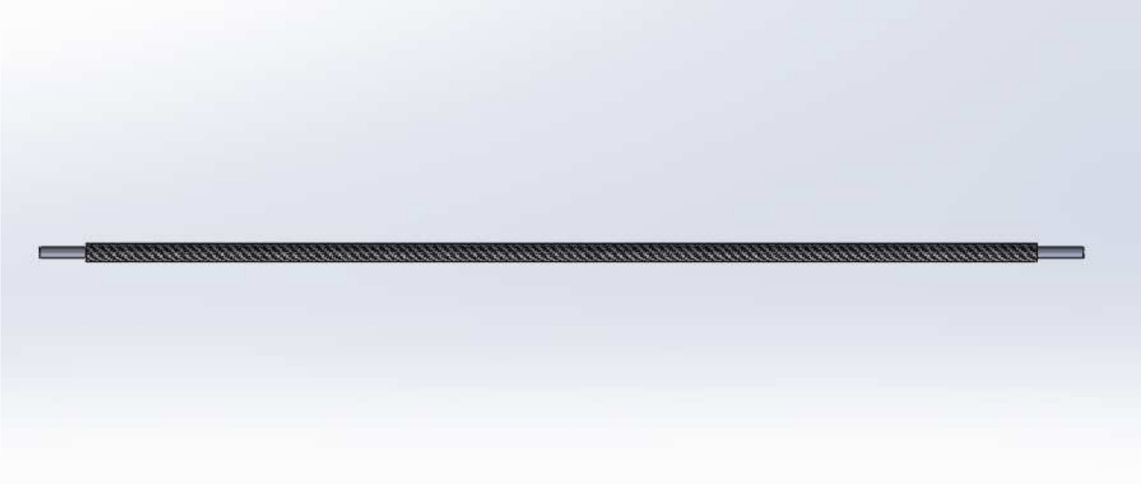

Figure 4. 29: 3D CAD drawing of the final design of carbon fiber shaft

The maximum of the torsional stress that is acting on this shaft comes from the motor maximum toqrue which is about 6.8 N-m or 5 lb-ft. This is the maximum torque which only happens at the peck current of the motor. The shaft can only experience this maximum torque under the condition that the quadcopter startup will have the maximum power when all rotors are at rest. This is unlikely to happen because the ESC for controlling the electric motor was set in the helicopter mode, which allows the rotor to spool up more gently at the stage of starting up. Nonetheless, we still need to design for the worst case scenario. When the torque applies to the shaft, there are the places where this shaft could fail; one is the bonding surface between the shaft and steel rod, the other ones are the carbon fiber shaft which is a failure in itself, due to the torsional load. The shaft torsional stress for hollow tube can be calculated by using the equations from Shigley's Mechanical Engineering Design book [32].

$$\tau = \frac{T * r_{out}}{J} \quad (4.2.4)$$

$$J = \frac{\pi}{2}(r_{out}^4 - r_{in}^4) \quad (4.2.5),$$

where τ is the shear stress, r_{out} and r_{in} is the outer radius and inner radius of the shaft, J is the polar Moment of inertia for hollow tube, and T is the applied torque.

The bonding adhesive material used for the testing carbon fiber shaft is Devcon 30 minutes 2-Ton Epoxy. It claims that it has the bond strength of 2500 psi. The stress on the bond surface can be calculated using the equation as follows:

$$F = \frac{M}{r} \quad (4.2.6)$$

$$\sigma = \frac{F}{A_s} \quad (4.2.7),$$

where “M” is the applied torque, “r” is the inner radius of the carbon fiber tube, “σ" is the shear stress acting on the bonding surface, and “A_s” is the total bonding surface area. [33]

Using equation from above, it was found that the shear stress on the carbon fibre tube and bonding surface between the steel rod and carbon fiber depends on the torque that is applied to the shaft. The shear strength for carbon fiber composite material can vary from 70 MPa to 260 MPa, depending on whether it is oriented 0/90-degree or -/+ 45-degree angle towards the loading axis [27], since there is no inforatiom about the mechanical properties of this carbon fibre shaft. Therefore, the best way to know if this carbon fiber shaft could handle the 6.8 N-m torque, is to put this shaft into a torsional test. Fig. 4.30 shows the settings of the experiment. The lever arm is about 11 inches, and it comes from the center of the shaft to the hanging weight. A plastic bag filled with testing weights is attached to the end of the lever arm. An electric drill is attached to the other end of the shaft to rotate the shaft. The torque on the electric drill is rated at 37 N-m, which is enough torque for running this experiment. The steel rod was inserted into the carbon fibre tube about 13 cm in length and assumed that 6.8 N-m torque was applied to the shaft; the shear stress on the bonding surface is about 137 psi; this is far less than 2,500 psi. So the carbon fiber shaft will crack before the steel rod debonding from the carbon fiber tube.

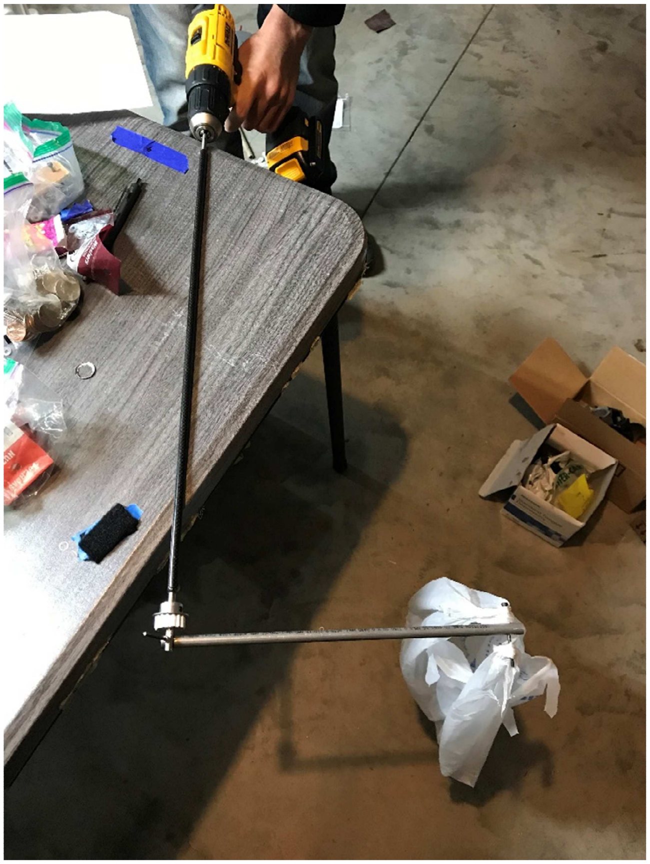

Figure 4. 30: A torsional test conducted on the carbon fiber shaft

The table 4.6 displays the tested weights in grams, – as well as the torque load that was caused by testing weight in Newton-meters (N-m). The results show that carbon fibre shaft passed the first torque load and failed at the second torque load. During the 5.4 N-m test, the lever arm rotated about 50 degrees before the carbon fiber tube failure which is equivalent to 4.06 N-m of the torque.

Table 4. 6: Carbon fiber shaft torsional test

Weight in g	Torque in N-m	Result
1345	3.66	passed
2000	5.4	failed
2500	6.8	N/A

Fig. 4.31 shows the carbon fiber tube failure under the torsional load. The cracks oriented about 45 degrees to the center line of the shaft indicated that it is a typical torsional failure for the shaft. Although the result did not pass the 6.8 N-m test, this shaft would never experience this 6.8 N-m torque value because that ESC was programed in Helicopter mode, which allows the rotor to slowly spool up. So the only torque that is acting on the shaft during the flight will come from the rotor drag. The maximum torque from the rotor is about 1.3 N-m, which is much less than 4.06 N-m.

Figure 4. 31: Carbon fiber shaft failure under torsional load

Shaft Critical Speed

When the operating RPM is close to the critical speed of shaft, this will excite the natural frequency of rotating shaft and cause the shaft to whirl at its natural frequency. This excessive vibration can cause damage to the gearbox and power transmission system.

The critical speed of the shaft depends on the length and weight of the shaft, – as well as on Young's module and an area moment of the inertia of the carbon fiber shaft. Equations 4.2.8[32] and 4.2.9 [32] were used for calculating the critical speed of shaft with considering only the shaft mass.

$$\omega_n = \sqrt{\frac{5g}{4\sigma_{st}}} \tag{4.2.8}$$

$$\sigma_{st} = \frac{5wL^4}{384EI} \qquad (4.2.9),$$

where ω_n is the critical speed of the shaft in rad/s. σ_{st} is the static shaft deflection with bearing supported on both ends. w is the mass per unit length, L is the length of the shaft, E is the young's module for the carbon fiber composite material, and I is the moment of inertia of the hollow shaft. Table 4.7 displays all the variables for calculating the critical speed of the shaft.

Table 4. 7: Variables for computing the critical speed of the shaft

M/L (kg/m)	E (pa)	I (m^4)	L (m)
0.1	1.03E+11	1.37444E-10	0.59

The calculation shows that ω_n = 1048.4 rad/s for this shaft (1 rad/s is about 9.55 RPM). So the critical speed for this shaft was about 10,012 RPM, and the shaft maximum RPM was 3000, – which is much lower than the critical speed. Therefore, there was no need to place a bearing in the middle span of the shaft. The main shaft was supported by several bearings and gearboxes along the shaft. There was no need to consider the critical speed of the main shaft.

4.2.5 Bending Stress on Bevel Gear

The maximum resistance torque that was created by each rotor is about 1.3 N-m. This resistance torque creates a bending stress on the bevel gear's teeth. To make sure that these bevel gears can survive the bending stress that is generated by the resistance torque, the bending stress on the gear tooth must be calculated and compared with the yield strength of the bevel gear material. If the stress is larger than the yield strength, the gear teeth will likely be stripped out and damaged.

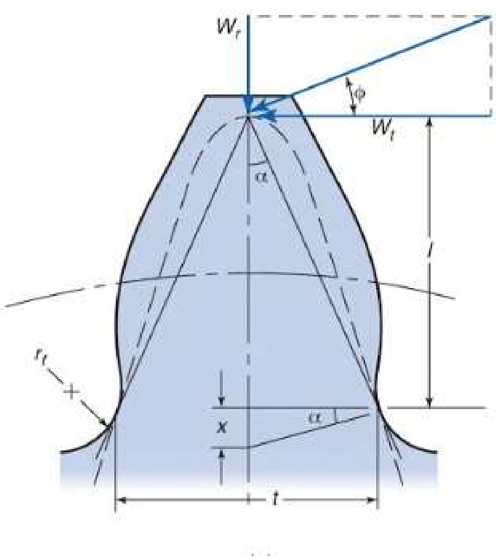

Figure 4. 32: Example of the gear teeth's profile. [34]

Fig. 4.32 shows the force that is acting on the gear tooth; "W_r" is the force that is normal to the tooth top surface, and "W_t" is the tangential force that is acting on the tooth. To calculate the bending stress on the tooth, "W_t" will be calculated first.[32]

$$W_t = \frac{T}{R} \tag{4.2.10},$$

where "T" is the resistance torque, and "R" is the pitch radius of the gear.

The bending stress equation for the bevel gear is shown below:

$$S_t = \frac{W^t}{F} P_d K_0 K_v \frac{K_s K_m}{K_x J} \qquad (4.2.11),$$

where F is the gear tooth width. Fig. 4.33 shows an example of the gear nomenclature.

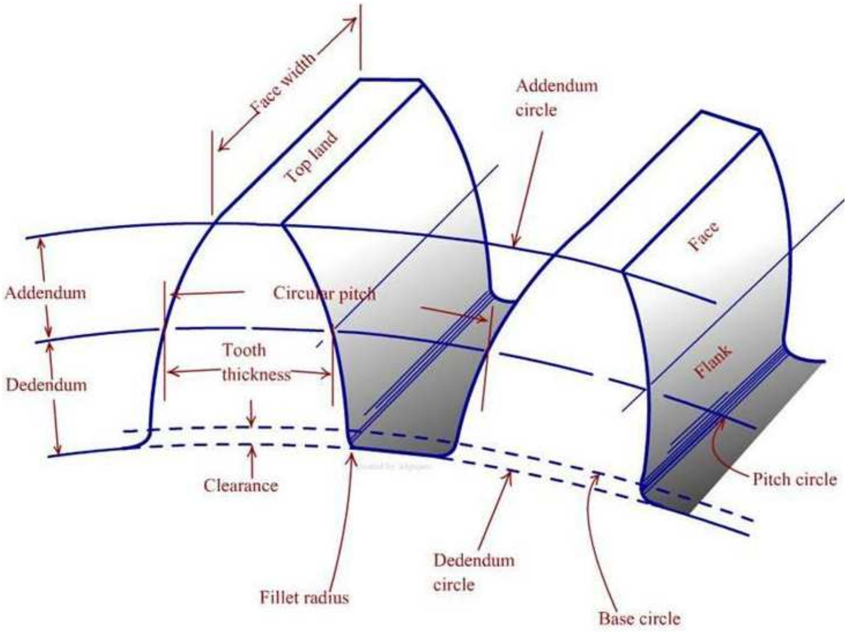

Figure 4. 33: The gear teeth nomenclature. [35]

P_d is the outer transverse diametral pitch which is defined as $P_d = N/d_p$, N is the number of the teethes on the gear, and d_p is the pitch diameter of the gear.

K_0 is the overload factor that compensates for the system vibrations which are caused by the driving condition between the driver and driven sources. Fig. 4.34 shows the overload factor based on the driver source and driven source condition [32]. According to the American Gear Manufactures Association (AGMA), the definition for the characteristics of the driving source is shown in Tables 4.8a and 4.8b. [36]

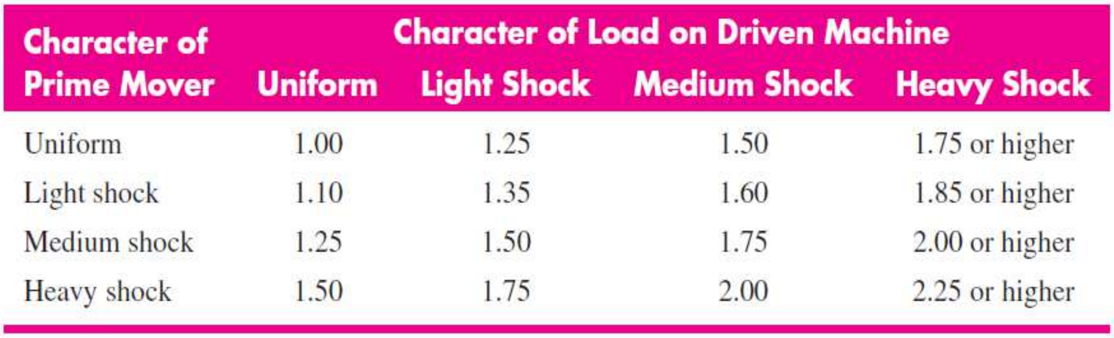

Character of Prime Mover	Character of Load on Driven Machine			
	Uniform	Light Shock	Medium Shock	Heavy Shock
Uniform	1.00	1.25	1.50	1.75 or higher
Light shock	1.10	1.35	1.60	1.85 or higher
Medium shock	1.25	1.50	1.75	2.00 or higher
Heavy shock	1.50	1.75	2.00	2.25 or higher

Figure 4. 34: Overload factor K_0 depends on the driver and driven source [32]

Table 4. 8: Driver source condition

Uniform	Electric motor, steam turbine, gas turbine
Light shock	Combustion engine with many cylinders
Medium shock	Combustion engine with few cylinders
Heavy shock	Single cylinder combustion engine

Table 4. 9: Driven source condition

Uniform	Generator, centrifugal compressor, pure liquid mixer
Light shock	Lobe-type blower, variable density liquid mixer
Medium shock	Machine tool main drive, multi-cylinder compressor or pump, liquid/solid mixer
Heavy shock	Ore crusher , rolling mail, power shovel, single cylinder compressor or pump, punch press

K_v is the Dynamic Load Factor that takes into account the manufacture quality control of the gear related to the operating RPM. Fig. 4.35 shows that K_v is a function of pitch line velocity and Q_v

value. According to the AGMA, Q_v is the transmission accuracy number that is rated from 5-11 for describing the manufacture quality of the gear. A Q_v value between 5-8 is a commercial quality, and between 9-11 – a high precision quality.

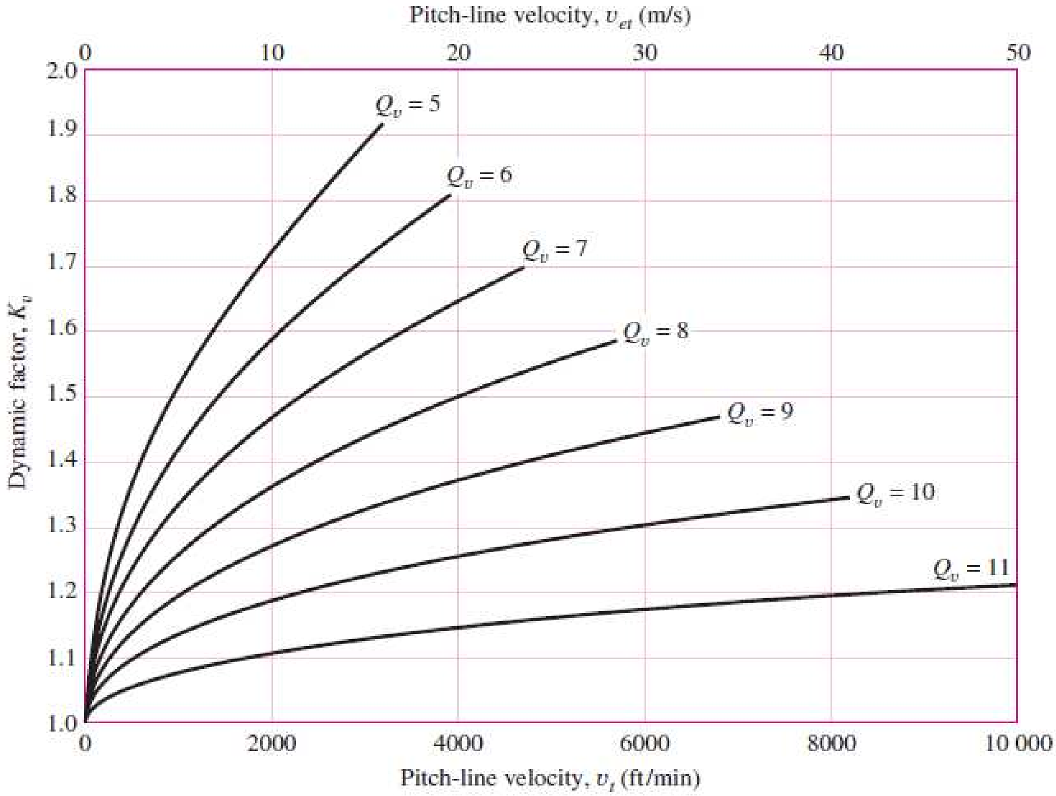

Figure 4. 35: The dynamic load factor Kv depends on the gear pitch line velocity v_t and manufacture quality of gear Qv. [32]

The K_v can also be calculated based on the pitch line velocity v_t and Q_v value [32].

$$K_v = \left(\frac{A+\sqrt{v_t}}{A}\right)^B \tag{4.2.12}$$

$$A = 50 + 56(1 - B) \tag{4.2.13}$$

$$B = 0.25(12 - Q_v)^{2/3} \tag{4.2.14}$$

K_x is the Lengthwise Curvature Factor for Bending Strength. For a straight bevel gear, the K_x value equal to 1 according to the AGMA.

K_s is the Size Factor for bending [32], and the equation for calculating the size factor is shown below:

$$K_s = \begin{cases} 0.4867 + \frac{0.2132}{P_d} & 0.5 \leq P_d \leq 16\ teeth/in \\ 0.5 & P_d \geq 16\ teeth/in \end{cases} \qquad (4.2.15)$$

K_m is the Load Distribution Factor for bevel gear; this factor can be calculated using the equation below:

$$K_m = K_{mb} + 0.0036F^2 \qquad (4.2.16),$$

where

$$K_{mb} = \begin{cases} 1.00 & both\ members\ straddle - mounted \\ 1.10 & one\ member\ straddle - mounted \\ 1.25 & neither\ member\ straddle - mounted \end{cases} \qquad (4.2.17)$$

J is the Bending Strength Geometry Factor for 20^0 pressure angle and 90^0 shaft angle straight bevel gear. This factor is dependent on the teeth number for the driver gear and driven gear. Based on these two numbers, it is possible to go to Fig 4.36 to read off the Geometry Factor [32].

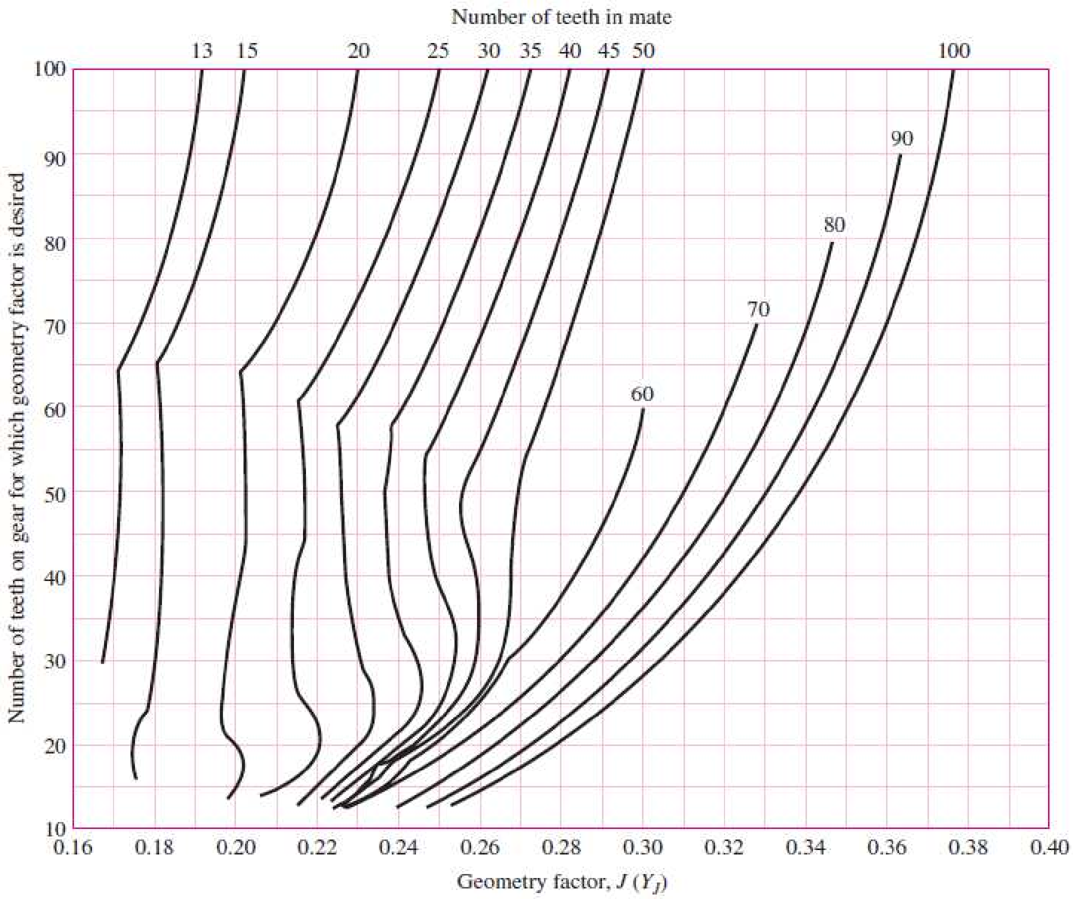

Figure 4. 36: Geometry factor for the 20 degree pressure angle straight bevel gear [32]

Table 4.9 displays all the factors and variables which are necessary for computing the bending stress on the gear tooth.

Table 4. 10: List of factors for calculating the gear teeth bending stress

W_t	Load	28.76 lbf
F	The net face width	0.17 inch
P_d	Outer transverse diametral pitch	30 teeth per inch
K_0	Overload factor	1.5

K_v Dynamic Factor	1.26
K_m Load Distribution Factor	1.1
J Bending strength Geometry Factor	0.218
K_x Lengthwise Curvature Factor	1
K_s Size Factor	0.5

Using the equation 4.2.11 from above, the bending stress on the teeth is calculated in below

$$S_t = \frac{28.76}{0.17}\,(30)(1.5)(1.26)\frac{(0.5)(1.1)}{(1)(0.218)} = 20{,}016 \text{ psi}$$

The bevel gear is made of hardened brass which has a yield strength of 50,763 psi. The factor of safety is calculated in below

$$\text{SF} = \frac{50763}{20016} = 2.536$$

This indicates that when the quadcopter operates at its maximum limit, these gears still have a SF of 2.536.

4.2.6 Bearing Analysis

The gearbox consists of four flange bearings that press fitting on to the gear wall. The main shaft bearing used 5/16 inch for inner diameter and the arm shaft used 6 mm for the inner diameter. Each bearing properties are shown in table 4.10 [40].

Table 4. 11: Gearbox bearings specification

Shaft Dia	Housing ID	Housing Wd	Flange OD	Flange Thick	Material	Dynamic	Static	Rated Speed
6mm	13mm	5mm	15mm	1.1mm	440C stainless steel	240 lbf	90	48000 RPM
5/16 inch	1/2inch	5/32inch	0.547 inch	0.03 inch	440C Stainless steel	120 lbf	50	48000 RPM

The radial force and axial force on the gears will transfer to the bearings. The bearings must able to withstand the loads from the gears and maintain good bearing life. The radial load for the main shaft bearing is calculated using equation 4.2.10 from above, which is about 57.5 lbf; but since there are two bearings supporting the main gear, each bearing will be carrying half the load, which is 28.3 lbf. The axial load of the main bevel gear also needs to be calcaluated because the 8x10mm shims are added between the gear and bearing. This will transfer most of the axial load of the gear to the bearing. To calculate the bevel gear axial load, the euqation [68] shows in below

$$W_a = W_t * \tan(\varphi)\sin(\Gamma) \tag{4.2.18}$$

φ is the gear tooth pressure angle, for stright bevel gear is 20 degrees. Γ is the gear contact angle, for this bevel gear is 45 degrees. W_t is the gear load which is the torque divided by radius of gear. The axial load for one gear mesh is shown below:

$$W_a = 28.3 * \tan(20)\sin(45) = 7.28 \text{ lbf}$$

Thus, it is possible to say that there are two bevels from the arm shafts that are meshed with the main shaft bevel gear. The axial load is double on the main shaft gear, which is about 14.6 lbf. The dynamic rating load for the main shaft bearing is 120 lbf. The design load is a way below the rating load.

The 6mm bearing radial load comprises half of the main gear total load. This is because the main gear load is a summation of 2 rotor shaft gears' load. Thus, the radial load is also 28.3 lbf, which is a way below the rated dynamic load of 240 lbf. The equation for computing the bearing life in hours is presented below:

$$L_{10} = \frac{60L_R n_R}{60n_D}(\frac{C_{10}}{F_e})^a \qquad (4.2.19),$$

where

L_{10} is the bearing operation life;

L_R is the rated bearing life in 10E+6;

n_R is the rated RPM;

n_D is the operation RPM;

C_{10} is the dynamic load rating;

F_e is the radial and axial combination load; and

a is 3 for ball bearing.

Thus, the main shaft bearing experienced both radial and axial load. The combination of axial load and radial load equivalent load F_e, must be calculated in order to find the life time of bearing.

$$F_e = X_i V F_r + Y_i F_a \qquad (4.2.20),$$

where V = 1 is used for ball bearing, F_r is the radial load, and F_a is the axial load. The X and Y are the factors which are based on factor E, and factor E is based on F_a/C_0. If $F_a/VF_r \leq e$ then uses X_1 and Y_1 table from Fig. 4.37. If $\frac{F_a}{VF_r} \geq e$, then employing the X_2 and Y_2 table from Fig. 4.37.

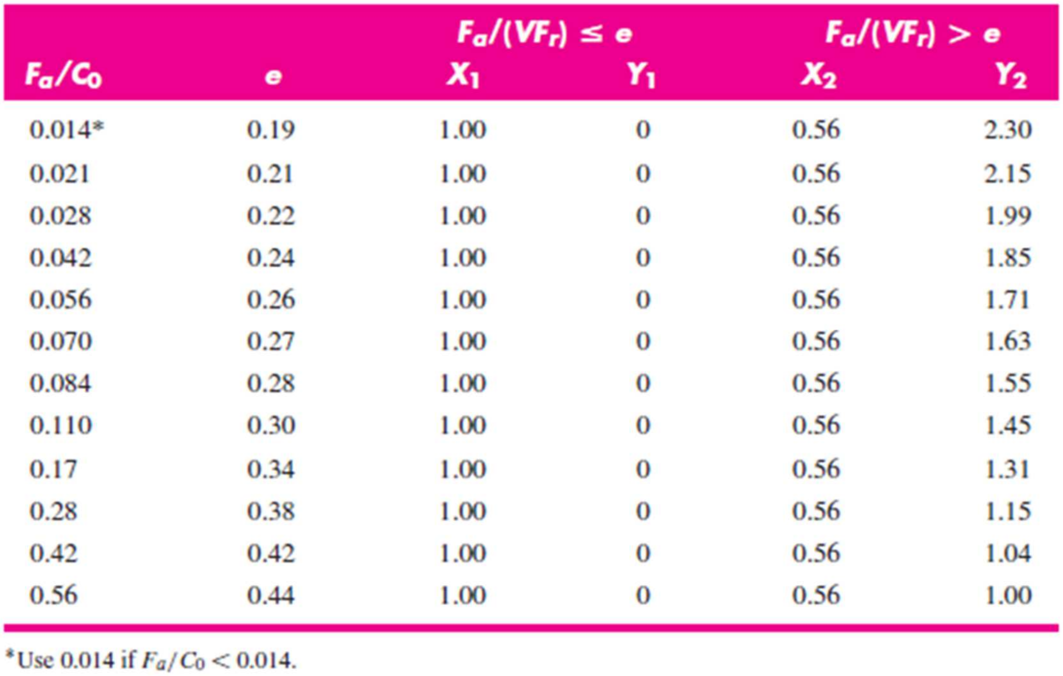

		$F_a/(VF_r) \le e$		$F_a/(VF_r) > e$	
F_a/C_0	e	X_1	Y_1	X_2	Y_2
0.014*	0.19	1.00	0	0.56	2.30
0.021	0.21	1.00	0	0.56	2.15
0.028	0.22	1.00	0	0.56	1.99
0.042	0.24	1.00	0	0.56	1.85
0.056	0.26	1.00	0	0.56	1.71
0.070	0.27	1.00	0	0.56	1.63
0.084	0.28	1.00	0	0.56	1.55
0.110	0.30	1.00	0	0.56	1.45
0.17	0.34	1.00	0	0.56	1.31
0.28	0.38	1.00	0	0.56	1.15
0.42	0.42	1.00	0	0.56	1.04
0.56	0.44	1.00	0	0.56	1.00

*Use 0.014 if $F_a/C_0 < 0.014$.

Figure 4. 37: Equivalent load factor for ball bearings. [32]

The F_a/C_0 for the main shaft bearing is 0.2; based on the information from Fig. 4.37, it is possible to say that e value is 0.38, which is smaller than the F_a/VF_r value. So it is better to use the X_2 and Y_2 table from Fig. 36 to calculate the F_e.

$$F_e = 0.56(1)(28.3) + (1.15)(14) = 31.95 \text{ lbf}$$

Bearing life for 5/16 inch shaft diameter is expressed below:

$$L_{10} = \frac{10^6}{60(2500)}\left(\frac{120}{31.95}\right)^3 = 353 \text{ hours}$$

Bearing life for 6mm shaft diameter is expressed below as well:

$$L_{10} = \frac{10^6}{60(2500)}\left(\frac{240}{28.3}\right)^3 = 4087 \text{ hours}$$

Rotor Shaft Bearings

The rotor shaft bearing has a shaft diameter of 6 mm, the bearing specification can be found in Table 4.10. The axial load is different, depending on the rotor spinning direction. Arms 1 and 4 placed the rotor shaft bevel gear upward, and Arm 2 and Arm 3 placed the rotor shaft downward. This is due to the differential gearbox which changed the direction of arm shaft rotation. If Arms 4 and 3 have the same setup, they will spin in the same direction. Fig. 4.38a and 38b show a different setup, and Fig. 4.39 shows the rotor spinning direction.

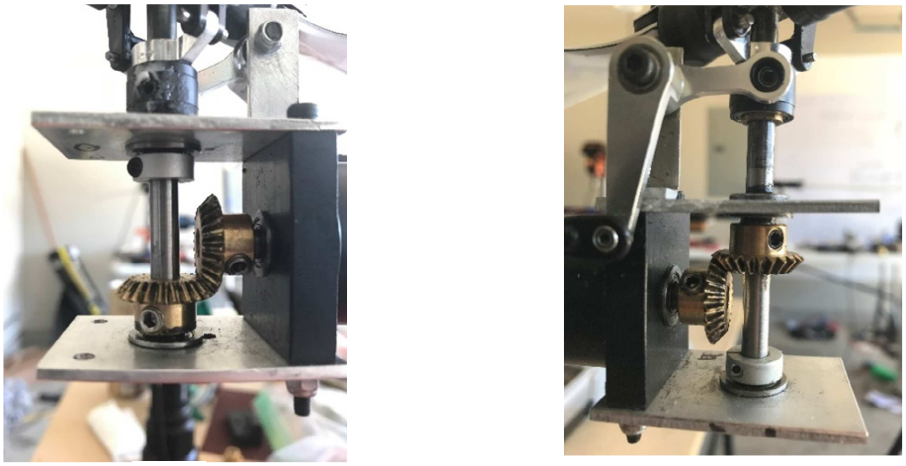

(a) (b)

Figure 4. 38a and 4.38b: (a) shows the setup for Arms 2 and 3. Figure (b) shows the setup for Arms 1 and 4.

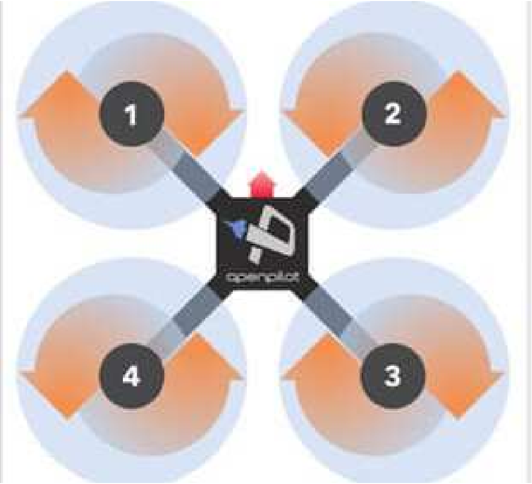

Figure 4. 39: The direction of rotor spinning [41]

The axial load on bearing the rotor shaft Arms 1 and 4 is higher due to the thrust created by the rotor and axial load produced by the gear mesh moving in the same direction. The axial load on bearing the Rotor Shaft Arms 2 and 3 is much less due to the axial load from the gear mesh which is acting in the opposite direction of the rotor thrust; so the net axial load is much smaller on the bearing.

The maximum of lift that is generated by the rotor is 9 lbf, and the axial load on each gear is 7.28 lbf (see Equation 4.2.18). So for Arms 1 and 4 of the rotor shaft, both forces are acting upwards, and total is 16.28 lbf of the force that is acting on the rotor bearings. This is only 18% of the static loading. For small bearings, the thrust load should not be higher than 25% of the static loading on bearing. The radial load on the bearing is the half of the W_t value due to there are two bearings on the rotor shaft that sharing the radial load, which is about 14 lbf.

For Arm 2 and 3 shaft bearing, the axial load of the bevel gear is acting against rotor thrust, so the overall axial load is equal to 1.3 lbf that acting on the bearing. The radial load will still be the same as Arm 1 and Arm 4, which is 14 lbf, since the rotor shaft bearing experienced both a radial and axial load. The combination of axial load and radial load equivalent load F_e, must be calculated with the use of Equation 4.2.20 presented above and in Fig. 36.

For Arms 1 and 4, F_a/C_0 value is 0.1812, and e factor can be interpolated using Fig. 36. From the interpolation, it becomes clear that in this case, the value is 0.344, and F_a/VF_r value is 1.134. So $F_a/VF_r \geq e$, according to Fig. 36, X_2 =0.56 and Y_2 =1.293 by interpolation. Thus, F_e can be calculated this way:

$$F_e = 0.56(1)(14) + (1.293)(16.3) = 28.9 \text{ lbf.}$$

Using Equation 4.2.18 from above, the life of rotor shaft bearing could be expressed this way:

$$L_{10} = \frac{10^6}{60(2500)}(\frac{240}{28.9})^3 = 3818 \text{ hours.}$$

For Arms 2 and 3, F_a/C_0 value is 0.0144, and according to Fig. 36, e factor is 0.19, which is greater than F_a/VF_r. Therefore F_e can be calcaulated this way:

$$F_e = (1)(1)(14) = 14 \text{ lbf}$$

Life of the rotor shaft bearing is shown below:

$$L_{10} = \frac{10^6}{60(2500)}(\frac{240}{14})^3 = 33586 \text{ hours}$$

4.2.7 Body Frame Stress Analysis

The body frame of the variable-pitch quadcopter is borrowed from the pervious gas-powered quadcopter. The body frame was made of two pieces of carbon fiber plate that were sandwiched together. Fig. 4.40 shows the top and bottom carbon fiber plates. Each plate has a dimension of 29 inch (length) x 8 (width) x 1/8 (thickness). According to Senior Design Final Report from 2013 [20], the fabrication of each carbon fiber plate consisted of total 14 layers of carbon fiber sheet. 12 layers of carbon fiber sheet were orientated in 0/90 degree, and two layers of carbon fiber sheet were orientated under the angle of 45 degree. This layout is based on the supposition that the carbon fiber plate is very strong and stiff in X and Y direction. However, torsion on the airframe may be a concern, since the carbon fiber layout only consists of two layers of carbon fiber sheet that is orientated under the angle of 45 degrees.

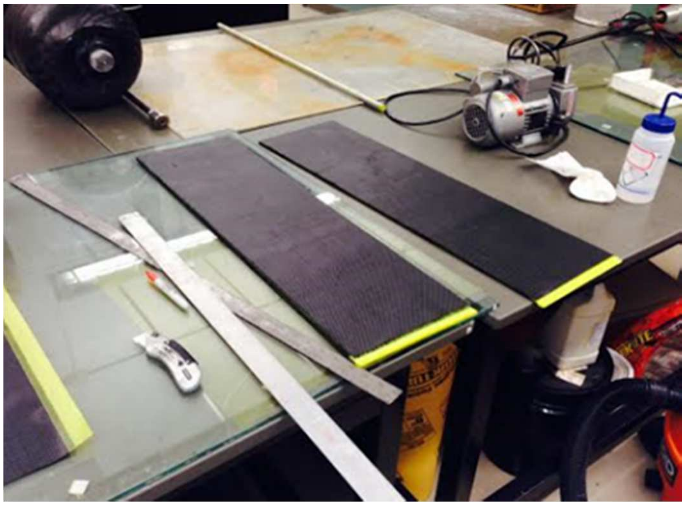

Figure 4. 40: The carbon fiber plates that were made by the senior design team

The rotor-supporting arms on this variable-pitch quadcopter is designed for the variable tilt purpose. The tip of the rotor must have two inches of clearance from the body frame when the rotor is tilted forward. Therefore, the rotor-supporting arm is much longer, compared to the previous gas-powered variable pitch quadcopter [18] [20]. A longer arm means increasing the bending stress that is acting on the airframe.

The Solidworks FEA were used for simulating the bending stress and deformations on the airframe. The material properties which were used in Solidwork simulation is the 3K carbon fiber composite. It is the most common type of carbon fiber material used for making UAVs and other aerospace applications. Fig. 4.41a and 4.41b show the simplified airframe of the quadcopter.

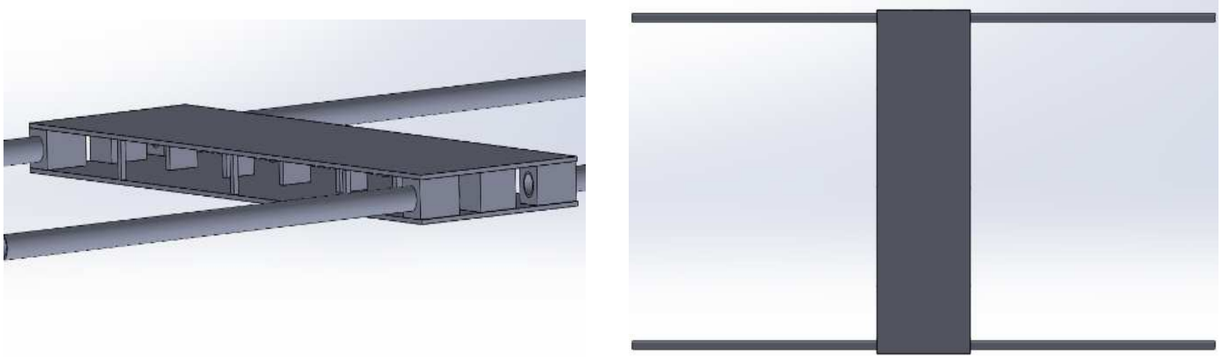

(a) (b)

Figure 4. 41a and 4.41b: Simplified quadcopter model for Solidworks simulation. (a) Shows the internal structure of the model. (b) Top view of the model.

Nine pounds of force were applied upwards to the tip of each rotor supporting arm to represent the maximum thrust generated by the rotor. The body frame is fixed at the bottom of its center of gravity location. Fig. 4.42 displays the maximum deformation at the tip of the supporting arm, which is about 2.2 mm. Fig. 4.43 shows the maximum bending stress occurring at the root of the supporting arm, which is about 48.5 MPa. The ultimate compressive strength of the carbon fiber composite material is 570 MPa. This gives the airframe a minimum safety factor of 11.7. The worst case scenario is when the quadcopter is doing yaw motion which requires two diagonal rotors to increase the thrust and opposite diagonal rotors – to decrease thrust. This motion creates a torsion on the body frame and causes the body frame to twist. To find the maximum tip deflection of the supporting arm under the yaw motion, nine pounds of force were applied upwards to the tip of two diagonal supporting arms. The other two diagonal supporting arms did not apply any force. Fig. 4.44 shows that the supporting arm tip deflection is about 3.3 mm under nine pounds of load, which is higher than 2.2 mm when all supporting arms are under nine pounds of load. This indicates that body frame is being twisted under the torsional load. This torsional deformation on the body frame may not be an issue for the flight controller that try to stabilize the quadcopter. If this become an issue later, adding more spacers in between the two carbon fiber plates can minimize the torsional deformation on the body frame.

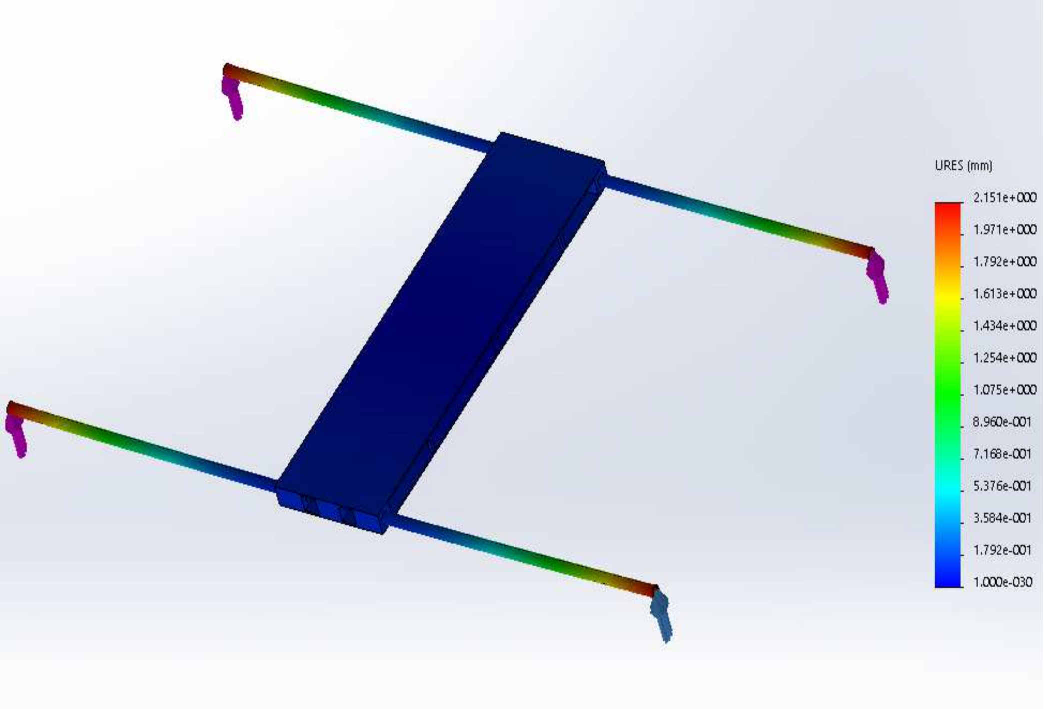

Figure 4. 42: FEA analysis of the deformation of the body frame

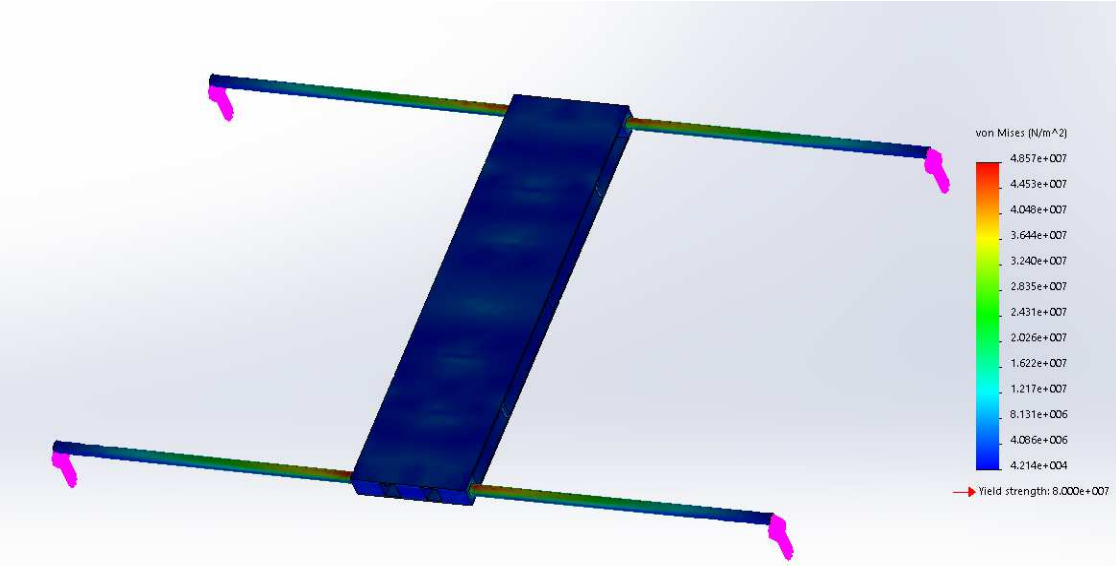

Figure 4. 43: FEA analysis of the maximum bending stress of the body frame

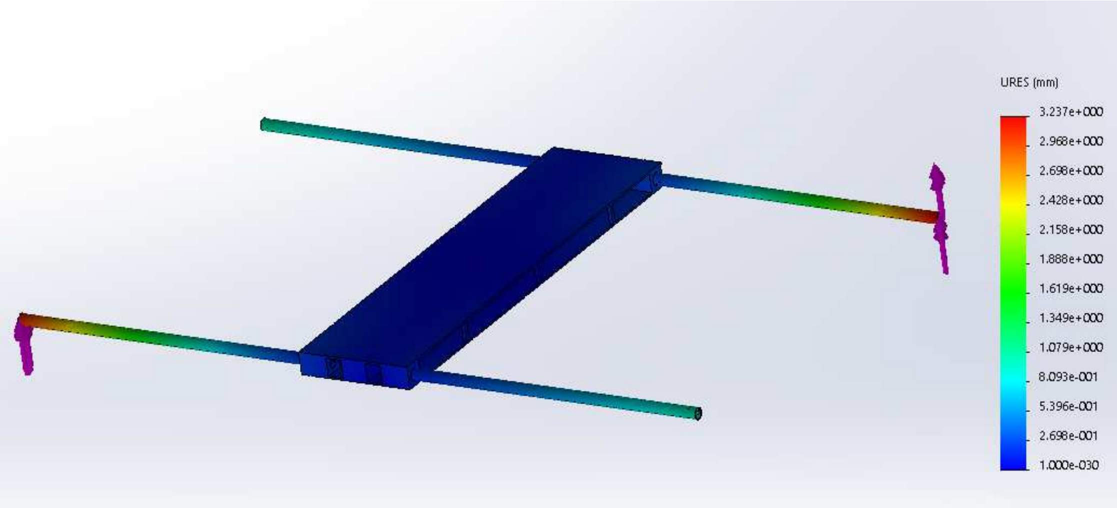

Figure 4. 44: FEA analysis of the maximum torsional deformation of the body frame and supporting arm tip deflection.

CHAPTER V

VEHICLE CONSTRUCTION

5.1 Variable Pitch Quadcopter Version I

Figure 5. 1: Quadcopter version I without batteries.

The quadcopter body frame is made of two identical carbon fiber plates that have a dimension of 29 inch (length) x 8 inch (width) x 1/8 inch (thickness). These two plates are sandwiched together with their internal structures by using 3M x 50 mm bolts. Figure 5.2 demonstrates the internal strcutures' layout.

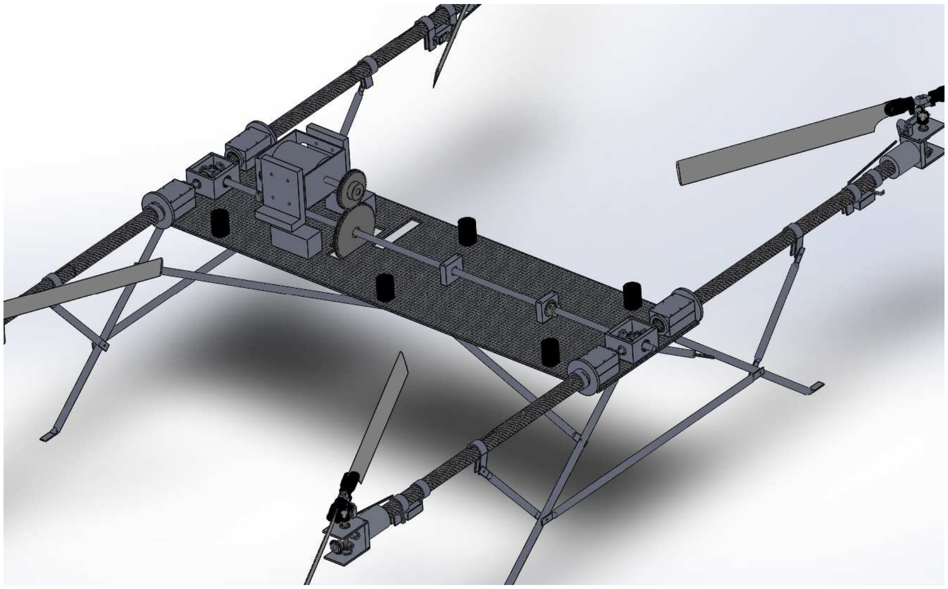

Figure 5. 2: 3D drawing of the quadcopter version I internal structure layout

A Mod 1 plastic pinion gear with 72 teeth is secured on the main shaft using a set screw. The main rotary shaft is made of a solid carbon steel rod which has a diameter of 5/16 inch and which is 32 inches long. Two identical gearboxes are attached to each end of the main shaft. A flange bearing is pressed onto each side of the gearbox to secure the main drive shaft and two arm shafts that go into the gearbox. Three bevel gears are secured on a flat spot of each shaft by using set screws. Figure 5.3 shows two rotor arm assemblies attached to the gearbox. Three bearing holders are used to secure the main shaft. Each bearing holder has an 8 x 22 x 7 mm ABEC bearing that fit in. Two bearing holders are located in front of the motor, and one is behind the motor. Three spacers are used on each side of the body frame to improve the rigidity of the frame. Two plastic blocks are placed underneath the motor mounted there to provide the support when the motor mount is bolted onto the frame. All the internal components that are sandwiched in between the two carbon fiber plates have the same height of 30 mm.

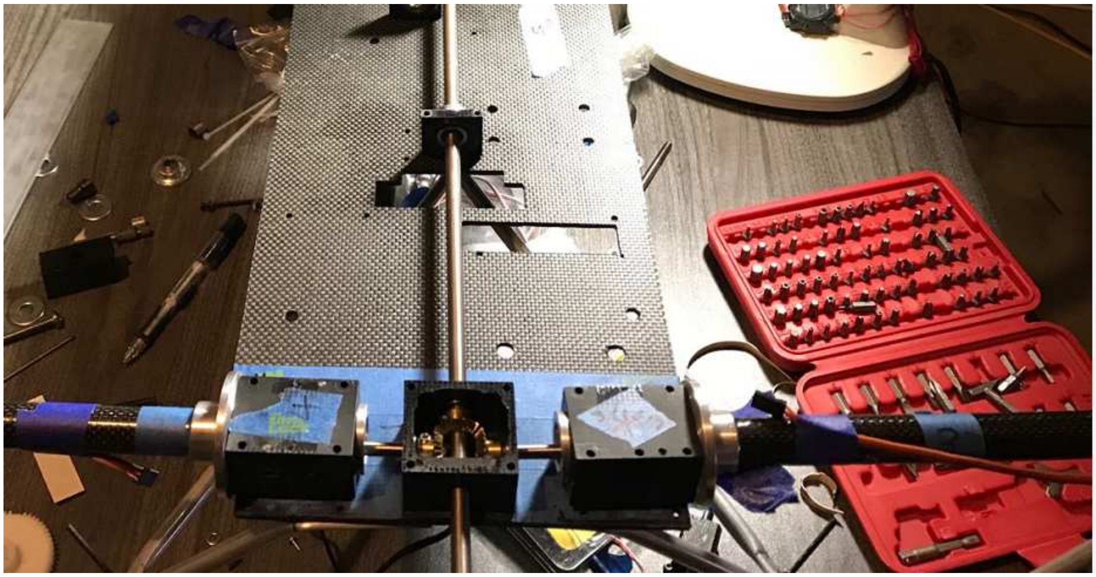

Figure 5. 3: The main shaft power two-arm shaft by using the gearbox

5.1.1 Rotor Arm Assembly

The rotor arm assembly is made of two sub-assemblies. The aluminum swivel tube sub-assembly and end arm bracket sub-assembly are joined together by a strong carbon fiber tube that connects the two sub-assemblies together with epoxy, as shown in Fig. 5.4

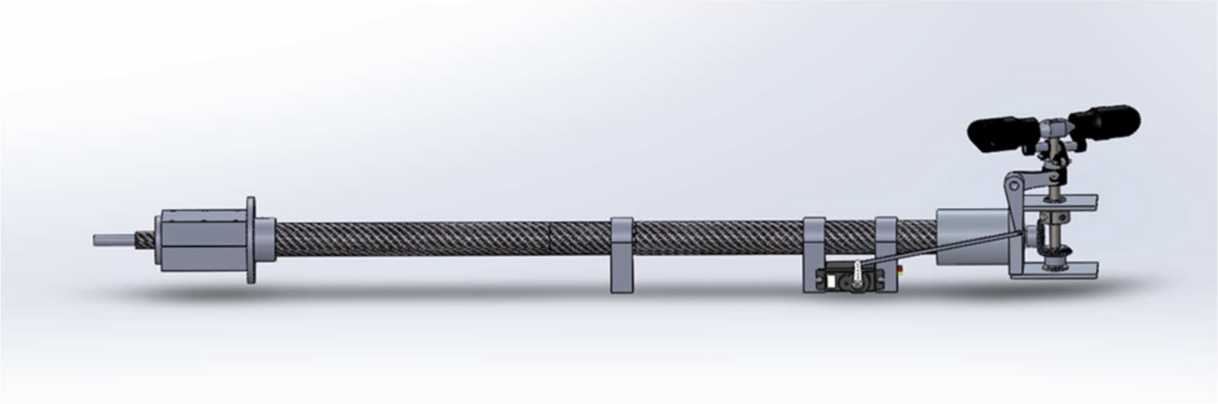

Figure 5. 4: A 3D CAD drawing of the rotor arm assembly. Rotor blades are not installed.

The aluminum swivel tube assembly was made by Logan from OSU MAE department for the variable tilt rotor purpose. The carbon fiber tube is epoxied to the inner wall of the swivel tube. The swivel tube has a tapered hole, so when the carbon fiber tube is inserted into the swivel tube, it provides a tight fit. Two swivel brackets have a cutout hole that is slightly bigger diameter than the swivel tube outer surface. When the two swivel brackets are clamped onto the swivel tube and when they are sandwiched between the upper and lower body frame panels, this allows the whole rotor arm assembly to tilt. However, this research project is only focused on the development of the variable-pitch quadcopter. The tilt rotor mechanism can be the subject of the future study. Figure 5.5 demonstrates using a few rubber bands that wrap around the aluminum swivel tube outer surface to secure the rotor arm assembly when the rotor arm assembly is bolted into the body frame.

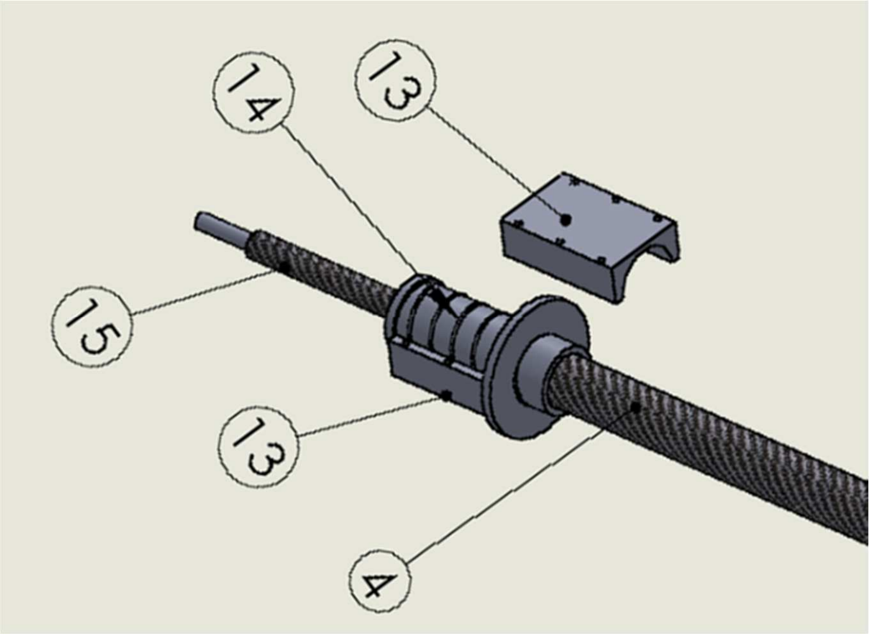

Figure 5. 5: An exploded view of the aluminum swivel tube assembly

It requires a calibration to make sure the rotor shaft axis is located under 90 degrees of the angle towards the body frame every time when the quadcopter is disassembled. The calibration can be done using a blade pitch gauge to grab onto the top mounting plate from the end arm assembly to make sure that the mounting plate is parallel to the body frame. Fig. 5.6 shows an exploded view of the end arm bracket assembly. The rotor assembly is modified from the Compass Chronos 700 tail rotor assembly. The rotor shaft is secured by two 6 mm-long flange bearings that press fit on the 1/8 inch-thickness aluminum mounting plates. A 6 mm-long shaft clamp is mounted on the rotor shaft to prevent the shaft moving upward. Two 6x8 mm washers are placed in between the clamp and bearing inner ring. A bevel gear is mounted on the flat spot of the rotor shaft with the help of a set screw. Four 6x8 mm washers filled the gap in between the bevel gear and bottom flange, bearing inner ring to prevent the shaft moving downward. Table 5.1 lists all the components for the rotor arm assembly.

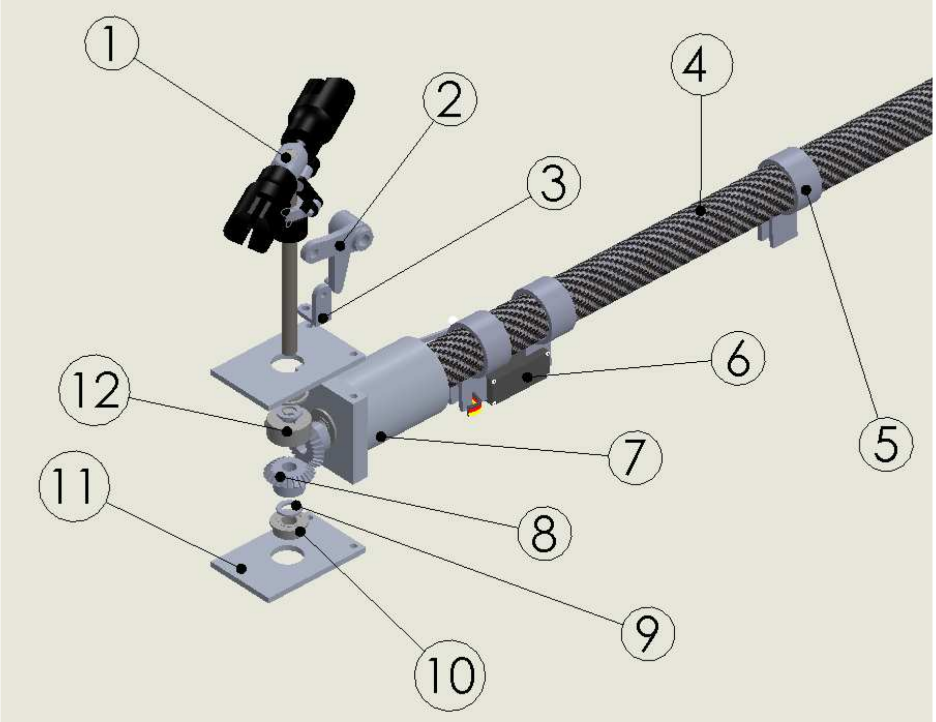

Figure 5. 6: An exploded view of the end arm bracket assembly.

Table 5. 1: A list of parts for constructing the rotor arm assembly

Rotor arm assembly parts	
#1	Compass Chronos 700 tail rotor assembly
#2	Metal Tail Arm Set
#3	Tail rotor control linkage hinge. Made from 1/8” thickness of aluminum plate
#4	0.76”OD x 0.625”ID carbon fiber supporting tube.
#5	Tube clamp mount. Made from 1/8” thickness of aluminum plate
#6	Savox SC-1257TG digital servo
#7	End arm bracket. Made from Delrin plastic
#8	32P 24T straight bevel gear
#9	6 x8 mm shim
#10	6 mm bore flange bearing
#11	1/8 inch thickness aluminum mounting plate
#12	6 mm shaft clamp
#13	Swivel bracket
#14	Aluminum swivel tube with rubber band wrapped around the outer surface
#15	Carbon fiber arm shaft

5.1.2 Motor Mount

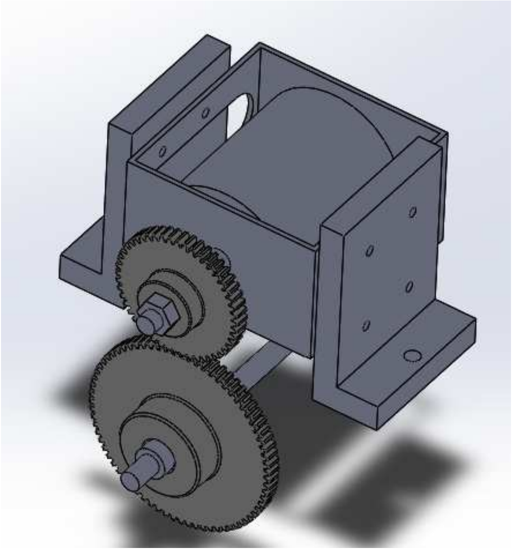

Figure 5. 7: A CAD drawing of the quadcopter version I motor mount.

The motor mount is made of Derlin plastic material. This type of plastic has excellent machinability and high strength and stiffness. The motor mount is machined in L shape with the wall thickness equal to 0.3 inches. The bottom of the motor mount is about 0.4 inch-thick. Four M5 alloy steel socket cap bolts are used on each side of the motor mount to secure the motor mount to the motor metal frame. One 5/16” x 5” long bolt is used to bolt each motor mount base to the quadcopter body frame. In order to have a proper gear mesh and minimum backlash, the motor mount bottom is sanded to reduce the gap between the two gears. The motor gear is Mod 1with a 52-teeth spur gear that is made of Hostaform C material. The motor shaft has 30 mm threaded shaft at the tip. The motor gear is mounted on the motor shaft by using a locknut to press against the gear hub, and on the back side of the gear there is a washer and shaft sleeve that are pressed in between the motor shaft retaining ring and gear.

5.1.3 Landing Gear

The quadcopter landing gear is made of 10 OD x 8 ID mm aluminum tubes. The walls of these aluminum tubes are 1mm-thick, which means that they are not very strong and that they are easy to bend under the heavy load. The landing gear is designed to deform under a hard landing, which absorbs the most energy and save the quadcopter's body structures. The arm strut tubes help support the rotor arm assembly and prevent the rotor arm from deflecting downwards when encountering a hard landing.

The tip of the aluminum tube is squeezed to a flat solid surface. This flat surface is easy to bend to a variety of angles and drilling holes on the flat surface. The landing gear legs are bolted under the body frame structure and positioned under the gearbox, which is the strongest part of the body frame. Fig. 5.8 demonstrates the landing gear assembly, and Fig. 5.9 shows the dimension of the landing gear.

Figure 5. 8: Landing gear is constructed from the aluminum tubes

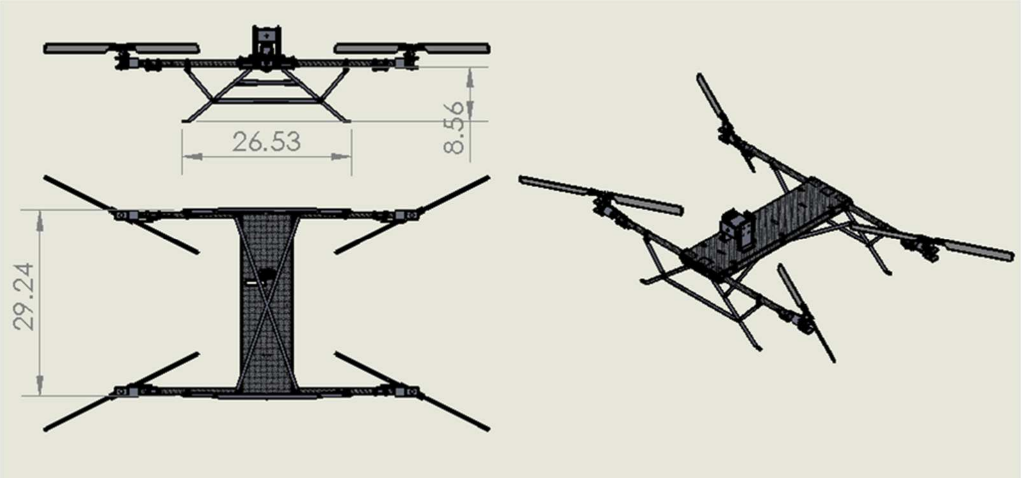

Figure 5. 9: Landing gear dimension in inches.

5.2 Variable Pitch Quadcopter Version II

The version II quadcopter is an improved variant of the first version of quadcopter. There are few changes made on second version of the quadcopter. The motor power transmission system was changed from the gear-driven system to the timing belt-driven system. The belt-driven system is much more “tolerant to vibrations and misalignment, compared to the gear-driven system. Fig. 5.10 shows the timing belt-driven system of the second version of quadcopter. Five bearings are used for securing the main shaft. Two bearings are placed very close to the main shaft pulley to minimalize the vibration from main shaft pulley.

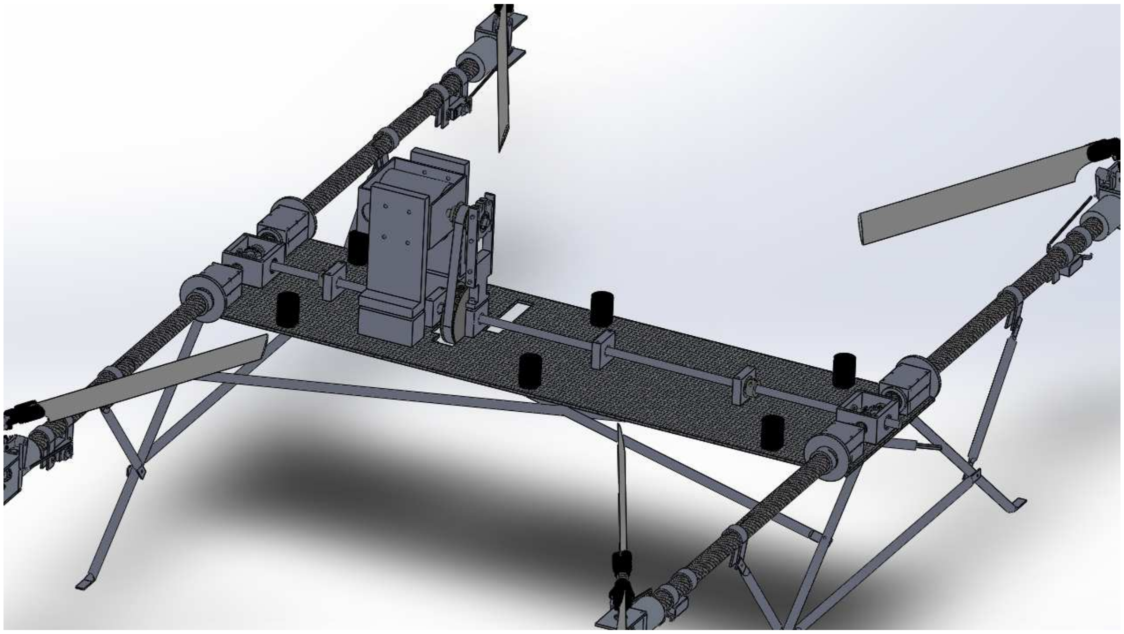

Figure 5. 10: A CAD drawing of the internal view of the quadcopter version II

5.2.1 AT5 Belt and Pulley System

The motor pulley and main shaft pulley are AT5 pulleys, and they are made of aluminum material. The motor pulley consists of 16 teeth, and the main shaft pulley consists of 36 teeth. This gives a gear reduction ratio of 2.25:1 from motor pulley to the main shaft pulley. There is no gear reduction from the rotor shaft to the main shaft. The motor has a maximum 7000 rpm, this gives the rotor speed about 3100 rpm with no load. The motor shaft bearing mount is made for supporting the tip of the motor shaft.

5.2.2 Motor Shaft Supporting Bearing Mount

Figure 5.11 demonstrates the bearing mount assembly. The base of the bearing mount is made of Delrin plastic and mounted on top panel of body frame. This bearing mount assembly provided support at the tip of the motor shaft.

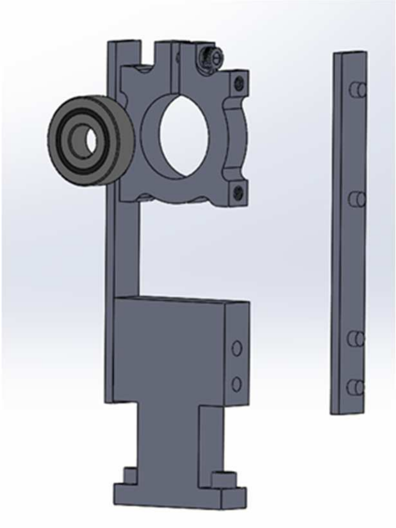

Figure 5. 11: An exploded view of a motor shaft supporting the bearing mount.

The base mount is positioned on the top of the main shaft bearing holder. Two M3 bolts are used to go through both of the base mount and main shaft bearing holder and bolting them together. This is to ensure that the tension between the two pulleys will not cause the body frame to deform. Two aluminum plates are used to join the base mount and bear the holder together, using screws and bolts. The two holes on the top of the plates are made slightly bigger than the screw holes; this allows a small adjustment to raise or lower the bearing mount before tightening screws. To install the motor mount on the quadcopter, it is necessary to ensure that the motor shaft is lined up with the main shaft in order to provide a smooth operation for the pulleys and belt. A laser alignment tool is used for checking the alignment of the two shafts. This will ensure the motor shaft is perfect line up with the main shaft vertically. To line up two pulleys horizontally, eyeballing is good enough for this because both pulleys have a belt which is 21 mm-wide, and the belt is only 16 mm-wide; so if two pulleys are not lined up perfectly in the horizontal way, the belt could still be able to move front and back about 2.5 mm towards its desired position when the motor starts to spin.

5.3 Variable Pitch Quadcopter Version III

The version III is the final version of this variable-pitch quadcopter. This version III is built upon the previous version. A few parts are added to the version III to ensure the smooth power transmission from the motor to the rotors. The belt tensioner is added to the quadcopter for providing the belt proper tension. The arm shaft bearing carriers are added to the four rotor arm assemblies for securing the arm shaft that are inside the arm supporting tube. This gives arm shafts a smooth rotation and less vibration on the gearbox. A few shims are added to the 8 mm bore bearing on the gearbox for transferring the axial load from the main shaft bevel gear to the bearing.

5.3.1 Belt Tensioner

The distance between the motor shaft center and the main shaft center was about 94 mm. Based on the calculations, it is possible to say that the desired belt pitch length was about 320 mm. However, the belt length was to come with a standard size. So the next available belt pitch length was 330mm. Therefore, a belt tensioner was required to keep the proper tension on the belt and make sure the belt would not slip during the operation. Fig. 5.12 shows the belt tensioner design.

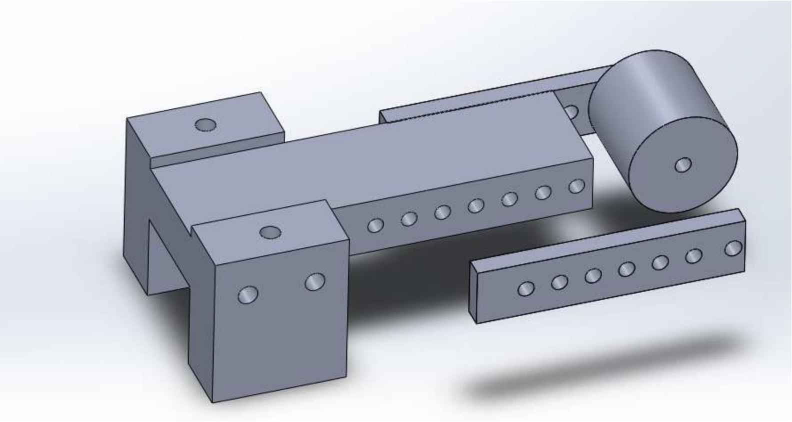

Figure 5. 12: A 3D drawing of the adjustable belt tensioner.

The based mount is made of Delirn plastic; two M3 bolts go through the top of the holes and are bolted to the top panel of the body frame. Two 1/8 thickness aluminum plates are bolted together with the base mount and idler pulley. A series of holes along the length of the aluminum plates allows the pulley idler go in and out to adjust the tension on the belt.

5.3.2 Gearbox

The bevel gears in the gearbox are mounted on the shafts by using set screws. These set screws do not handle the axial load very well. So a few 8 ID x 10 OD x 0.25 mm-shims are placed in between the bevel gears and bearing on the gearbox. This will transfer the axial load from the bevel gear to the bearings. Using multiple 0.25 mm thickness shims will create a tight fit between the bevel gear and bearing. However, it must ensure that the outer diameter of the shim is small enough to only touch the inner ring of the bearing and not the outer ring of the bearing. Otherwise it will create a lot of friction and heat to the bearing. Figure 5.13 shows the shims which have been added to the gearbox.

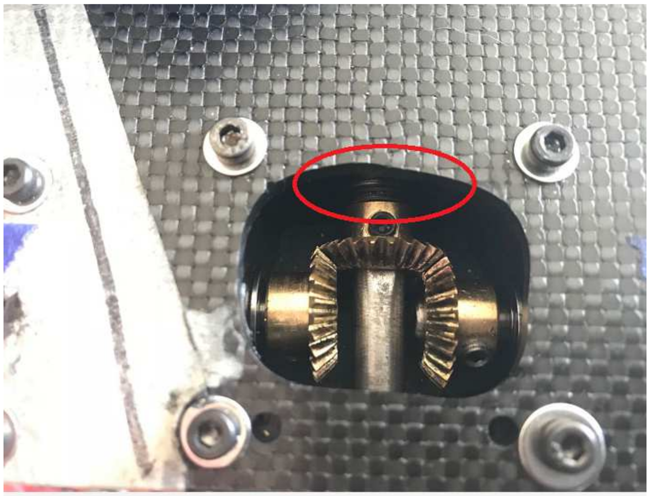

Figure 5. 13: 8x10x0.25 mm-shims are added to the gearbox for transferring the axial load to the bearing.

5.3.3 Bearing Carrier in the Arm Tube

In order to prevent the arm shaft whirling inside the supporting tube during the use of the device, a bearing carrier is added into the supporting tube. Fig. 5.14a shows the exploded view of the 3D design bearing carrier, and Fig. 5.14b shows the actual bearing carrier.

(a)

(b)

Figure 5. 14a and 5.14b: The figure on the left demonstrates assembly drawing of the bearing carrier. The figure on the right is the actual bearing carrier.

The bearing carrier consists of three parts: the first of them is the 8 mm bore flange bearing, the second part is the bearing carrier, and the third part is the rubber Oring. The inner diameter of the supporting tube is between 0.623 to 0.624 inches. In order to have a tight fitting to fit the bearing carrier inside the supporting tube, the bearing carrier outer diameter must cut down to 0.623-inch diameter. The bearing carrier has two different inner diameters. One side's diameter is 13 mm, and the other's - 9 mm. The 13 mm inner diameter only extends 1/3 of the total length of the bearing carrier, and the rest of its length is 9 mm in diameter. The 13 mm-inner diameter hole is made for the press to fit the 8 mm bore flange bearing on the bearing carrier. After the bearing has been pressed fit on the bearing carrier, the bearing carrier outer diameter is expanded a little bit, and then it becomes slightly bigger than the inner diameter of the supporting tube. So the outer surface bearing carrier needs to be sand down in order to be able to fit into the supporting tube again. The groove cutting on the bearing carrier is a very time-consuming job because the gap between the bearing carrier and the inner diameter of the supporting tube is very tight. If the groove is too deep, the rubber Oring will not able to provide a good friction between the bearing carrier and the inner arm-supporting tube. If the groove is too shallow, the bearing carrier will not be able to press into the arm-supporting tube. So this requires much time of trial and error in order to achieve a tight fitting. The carbon fiber arm shaft is sanded down on one side in order for the bearing carrier to slide on. This is due to the manufacture tolerance of the carbon fiber arm shaft. Fig. 5.15 shows that the carbon fiber arm shaft is sanded down on one side. To remove the bearing carrier from the arm-supporting tube, the carbon fiber shaft needs to be pulled outward, and the bearing carrier will catch on the unprecedented part of the shaft and move with the shaft turned outward.

Figure 5. 15: Half of the carbon fiber shaft is sanded for fitting into the bearing carrier.

CHAPTER VI

TESTING AND RESULT

6.1 Initial Testing

The purpose for this testing was connected with examining all the mechanisms of the quadcopter and proving the fact that it can lift off and carry its own weight. The variable pitch quadcopter version I was used for the first ground testing. The version I was using the gear driven system to transfer the power from the motor to the main shaft. Fig. 6.1 shows the completed version I quadcopter without batteries on board.

Figure 6. 1: Quadcopter Version I without batteries.

A CC3D flight controller was used for controlling the collective pitch of the quadcopter. Earlier this flight controller was mainly used for fixed-pitch quadcopters, but it could be modified for controlling the variable-pitch quadcopter. Fig. 6.2 shows the setup for using a CC3D flight controller on this quadcopter. The CC3D had six input channels, and the first four channels were Motor 1 through Motor 4. Last two channel were Aux channels. A Frsky X4R receiver was used to connect the CC3D by the Sbus port. All four servos on the quadcopter were powered separately from the flight controller by using a Lipo Battery. A 5 Volt BEC was used for powering the CC3D. Two 5 cells 5000 mAh Lipo batteries were connected in series to power the electric motor. Since the electric motor ESC did not have the BEC on board, the motor ESC was connected to the receiver directly. The RPM of the electric motor was controlled directly by the throttle stick on the transmitter but not on the CC3D flight controller. Fig. 6.3 shows the two 5 cells Lipo batteries and one small Lipo battery applied for powering the servos and flight controller. Blue tape was used for securing the batteries to the quadcopter body frame.

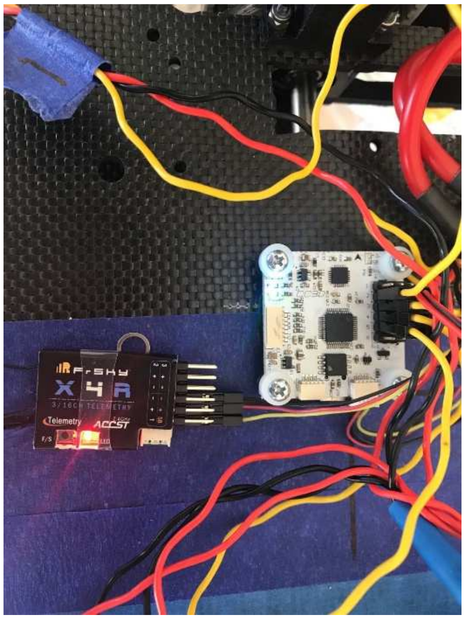

Figure 6. 2: CC3D flight controller setup.

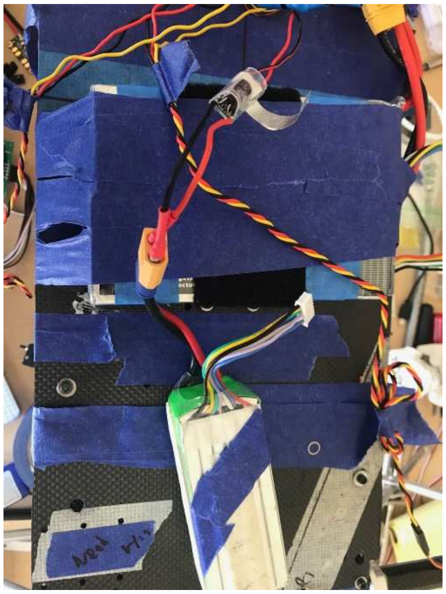

Figure 6. 3: Two 5 cells Lipo batteries are connected in series for powering the motor only. A small Lipo battery is used for powering the flight controller and servos.

The testing took place at the Richmond Hill back parking lot. Four wood logs were used to tie down the quadcopter on the ground, and only about 3 to 4 inches of space were used for the quadcopter to move freely when it was at airborne. Fig. 6.4 shows the testing setup. During the testing, the quadcopter did lift off for a second, but then the motor gear teeth got destroyed. So the testing was stopped.

Figure 6. 4: The first ground testing setup

Test Results

The result of the first testing showed that this motor does have the power to lift off the quadcopter. However, the motor gear got destroyed due to the excessive vibration from the main shaft. Fig. 6.5 shows the motor gear and main gear after the testing. The white gear is the motor gear, and the black gear is the main gear.

Figure 6. 5: motor gear damaged after the first testing

There were only two bearing holders that were holding the main shaft; both of them were placed far apart from each other. The main shaft gear is hanging in the middle of the shaft and there is no bearing to secure the shaft from moving upon down. When the motor gear is trying to drive the main shaft gear, they are also trying to push each other away. So at higher rpm, the main gear is separated from the motor gear. The load from the main shaft creates different rpm between the two gear and when two gears mesh again, the main gear strikes the motor gear and destroys the teeth on the motor gear. The motor shaft also gets bent after the gear strike.

6.2 Second Testing

The quadcopter version II was used for the second testing. The version II employs the belt and pulley driven system to power the main shaft. To simplify the test, all four servos were disabled, and flight controller was removed from the quadcopter. The pitch of the rotor blade was fixed at the angle equal to 18 degrees by using the blue tape to tape the pitch control linkage to the arm supporting tube. The only controllable parameter was the rpm of the motor. Figure 6.6 shows the testing setup.

Figure 6. 6: Setup for second ground testing.

The motor was powered up to its maximum power and hold for 30 seconds. There were some high frequency taping noise came out the quadcopter at 10 second of testing and rotor arm was shaking laterally. At about 20 second, all four rotors were slowing down and quit spinning in a few second, and motor is still spinning at maximum power. The testing was stopped after the 30 seconds run.

Test Results

The quadcopter did not lift off the ground during the second test. The blade angle was set to 18 degrees. Based on the Qprop prediction, the rotor blade stalled around 14 degrees of the angle. So the rotor blade was probably stalled during the test. After a careful inspection of the quadcopter from the second test, it became clear that there are a few issues which need to be addressed in this connection. The main shaft bevel gear set screw got loosened, and the gear was pushed back and disengaged from the gearbox. Thus, all four rotors stopped spinning. This could be fixed by placing a few shims to fit between the bevel gear and bearing. So the axial load was transferred to the bearing but not the bevel gear set screw. Also, all the set screws on the quadcopter needed to be located to prevent their loosening during the test. The timing belt got loosened after the second testing, and excessive belt wearing can also be seen in Fig. 6.7. This belt is a AT5 timing belt which is 9 mm wide. The motor pulley is a 16 teeth AT5 pulley, but the main pulley is a 36 teeth XL pulley. Although they both have a 5 mm pitch, but the tooth profile on each pulley is totally different. So the incompatibility of the belt and pulley caused the belt to slip; this led to an excessive belt wear. Fig. 6.8 shows different tooth profiles between the XL pulley and AT5 pulley. To prevent this from happening again, the XL pulley was replaced with the AT5 pulley, and belt width was increased from 9 mm to 16 mm. This should ensure that the belt will not slip or stretch under excessive loads.

Figure 6. 7: The belt became loose, and the white powder accumulated on the pulley indicated the excessive belt wear caused by belt slipping.

Figure 6. 8: A comparison between an AT5 and XL pulley. The AT5 pulley can be seen in the right part of the image, and XL pulley – in the left part of it.

The last thing which needed to be fixed was connected with putting a bearing carrier inside the arm supporting tube. The tapping noise during the second test actually came from the carbon fiber arm shaft hitting the inner wall of supporting tube at a lower rpm. Fig. 6.9 demonstrates what happened when a long fixable shaft spinning was applied at certain rpms. By placing a bearing carrier in the middle of the shaft, this could have been possible to reduce the shaft whirling.

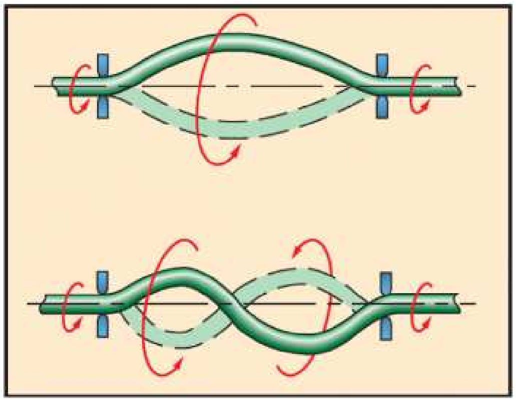

Figure 6. 9: Example of a shaft whirling at its natural frequency [41]

6.3 Third Testing

The quadcopter version III was used for the third testing. The version III was an improved version from the version II. This version used 16 mm AT5 belt instead of 9 mm belt. A belt tensioner was made for setting a proper belt tension. A few 8x10x0.25 mm shims were placed tightly between the main bevel gear and bearing. A bearing carrier was press-fitted in the arm supporting tube at about the middle point of the tube to reduce the arm shaft whirling. All four servos that control the blade pitch were controlled directly by the transmitter. Fig. 6.10 shows a control setup for the third test.

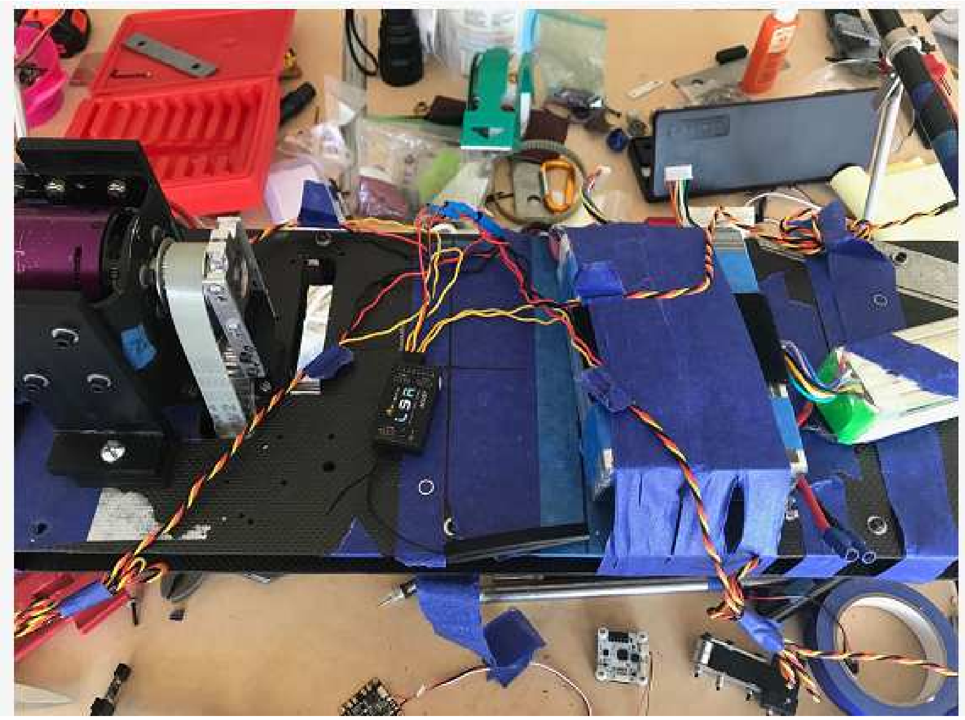

Figure 6. 10: Pitch control system setup

Servo 1 through servo 4 was connected to channel 1 through channel 4 on the receiver. All servos were charged with the help of a 5 Volts BEC, which was powered by a small Lipo battery. Servo 1 had the power wire and ground wire which were supposed to go into the receiver and supply 5 Volts power to the receiver. The motor ESC was connected on Channel 5 of the receiver. The servo

1 through servo 4 control could be mixed in the transmitter and controlled by one channel there. A blade pitch gauge was used to calibrate each blade pitch angle. When the throttle stuck at the bottom, all blades needed to be trimmed at 0 degree. This could be done by adjusting the control linkage length. Next move was the throttle stick to line up with the second mark on the throttle channel; checking all four rotor blade pitch angles, it was made clear then that they should all pitch about 9 degrees. If one servo pitches too much or too little, going into that servo channel on the transmitter changed the weight on the control or trimmed up or down. The next move was to make the throttle stick to the third mark, the blade pitch should be about 18 degrees. The blade stalled at 14 degrees, which is about half a way in between the second and first mark of the throttle. After the blade pitch angle was calibrated with the throttle stick, the blade pitch angle could be recorded during the test. Figure 6.11 demonstrates blade pitch calibration by using a blade pitch gauge. Figure 6.12 shows the throttle marks on the transmitter.

Figure 6. 11: Example of using a pitch gauge to calibrate the rotor blade pitch angle.

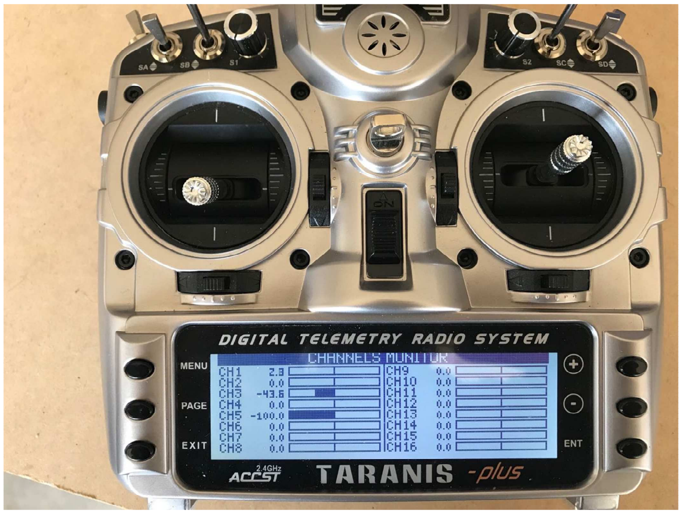

Figure 6. 12: A Taranis X9d transmitter is used for control mixing.

The S2 knob on the transmitter is used for controlling the rpm of the motor. For this test, the motor rpm will be fixed at its maximum power, which is about 7000 rpm without load. A SkyRC Helicopter Optical Tachometer is used to measure the rotor speed at a safe distance. Figure 6.13 shows the image of Optical Tachometer.

Figure 6. 13: SkyRC Helicopter Optical Tachometer [42]

The test is conducted at Richmond Hill back parking lot. A 6ft x 6ft Fiberboard wood is used to tie down the quadcopter. The quadcopter landing gear is tied to the Fiberboard wood by using nylon ropes, and quadcopter is able to move about 2 to 3 inches of distance above the ground. Figure 6.14 shows the quadcopter setup for the testing.

Figure 6. 14: Quadcopter setup for the third testing.

For the first 30 seconds of testing, the pitch angle on blades was set to 0 degrees, and the motor rpm was set at the maximum power. The Optical Tachometer was used for checking the rpm of the rotor speed at the motor maximum power setting. The optical tachometer showed 3018 rpm on the rotor speed at motor maximum power setting. Based on the gear ratio, this indicated that motor is spinning at 6790 rpm, which matched the rpm from the motor ESC data log. Then slowly the throttle stick was increased until the quadcopter lifted off the ground. The throttle stick position at the moment of lifting off was a little bit above the second mark, which was about 9 to 10 degrees of pitch. At the same time, the rpm of the rotor was dropped to around 2600 rpm.

Test Results

The result showed that the quadcopter version III did lift off the ground after all the changes which were made on this version. The rotor speed was matched with motor speed, which indicated that there is no slip between the belt and pulley and that everything was working properly. Fig. 6.15 shows the data log from the motor ESC recorder at hovering condition.

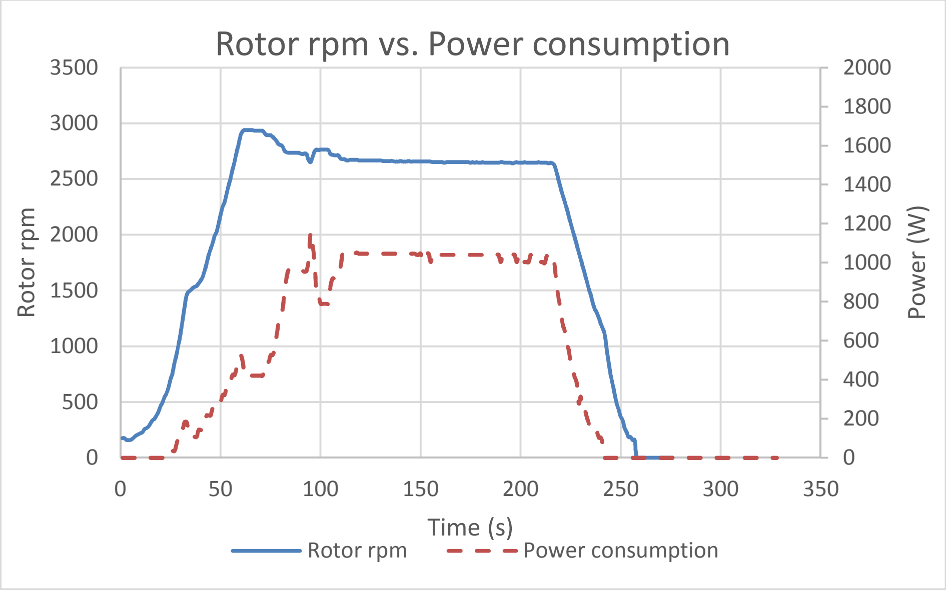

Figure 6. 15: Data log from motor ESC.

Figure 6.15 shows that the power consumption was at hovering position. The voltage of the battery dropped from 41.2 Volts to 36.6 Volts during the hover. So by increasing the pitch of the blade, the motor rpm decreased, which also caused the rotor rpm to decrease. Based on the Qprop prediction, the rotor speed was holding around 2600 rpm at hovering condition. The quadcopter total weight was about 17 lbs. This indicated that blade pitch angle was about 9 degrees at that point. In order to predicate the true performance of this vehicle, thrust, power consumption and motor rpm were recorded then at a different rotor blade pitch angle.

6.4 Thrust Testing for Different Blade Pitch Angles

The purpose of this test was to measure the thrust of the vehicle at 4, 6, 8, 10, 12, 14, 16, 18 degrees of blade pitch angles. The power consumption and rotor rpm were recorded at different blade pitch angles through the motor ESC. These measurements were later used for determining the vehicle's performance.

A digital scale was used to measure the thrust of the quadcopter by comparing the initial setup weight of the quadcopter and weight of the quadcopter at a particular blade pitch angle during the test. Figure 6.16 demonstrates the test setup.

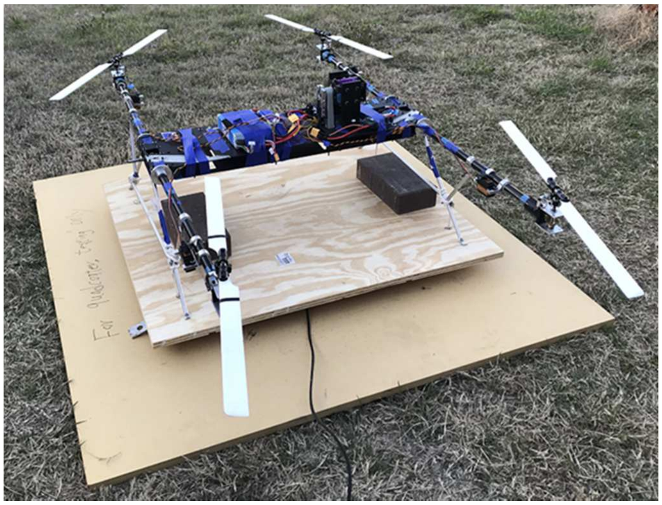

Figure 6. 16: Test setup for measuring the quadcopter thrust

A large fiberboard was used for providing a flat surface for the digital scale. A smaller plywood was placed on the top of the digital scale. The quadcopter was secured to the plywood by using ropes tied to the quadcopter landing gears. Two heavy bricks were added to the plywood to ensure that the quadcopter would not move at its maximum thrust. Figure 6.17 shows the digital scale that was used during the test. A pitch gauge was used to calibrate the blade pitch angle of four rotors and make sure that they all pitch at the same degree. Four new carbon fiber arm shafts were installed for replacing the old arm shafts. The old arm shafts were bent from the previous tests, and they caused vibration in the gearbox. The new arm shafts helped reduce the vibration on the gearboxes and decrease the power loss through the transmission system. New rotor shaft bearings were installed on the rotor arm number 2 and number 3 to replace the old rotor shaft bearings. The old shaft bearings caused too much resistance on the rotor shaft and needed to be replaced. The test started at the 4 degrees' blade pitch angle and was increased by 2 degrees for every test until it reached the theoretical stall angle which was about 18 degrees.

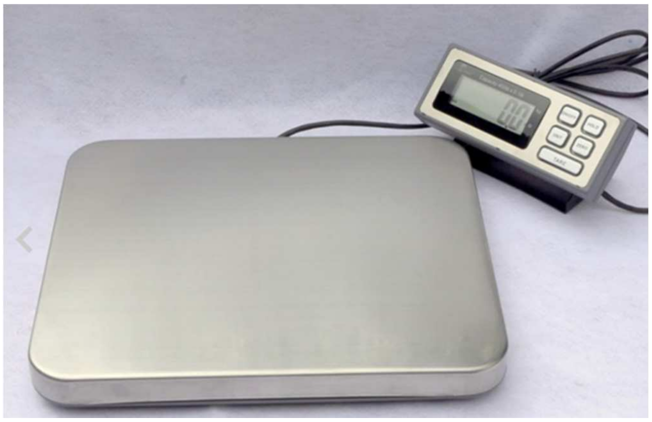

Figure 6. 17: A large digital scale is used for measuring the thrust values. [43]

Test results

The initial setup weight of the quadcopter was about 54 lbs from the digital scale reading. The quadcopter weight was about 16.9 lbs. The total thrust of the quadcopter at different pitch angles could be calculated by using the initial setup weight of the quadcopter and subtracting the lowest weight that was recorded at that particular blade pitch angle during the test. This gave the total thrust produced by the quadcopter at a specific blade pitch angle. Figure 6.18 demonstrates the total thrust produced by the quadcopter and maximum payload at a different blade pitch angle.

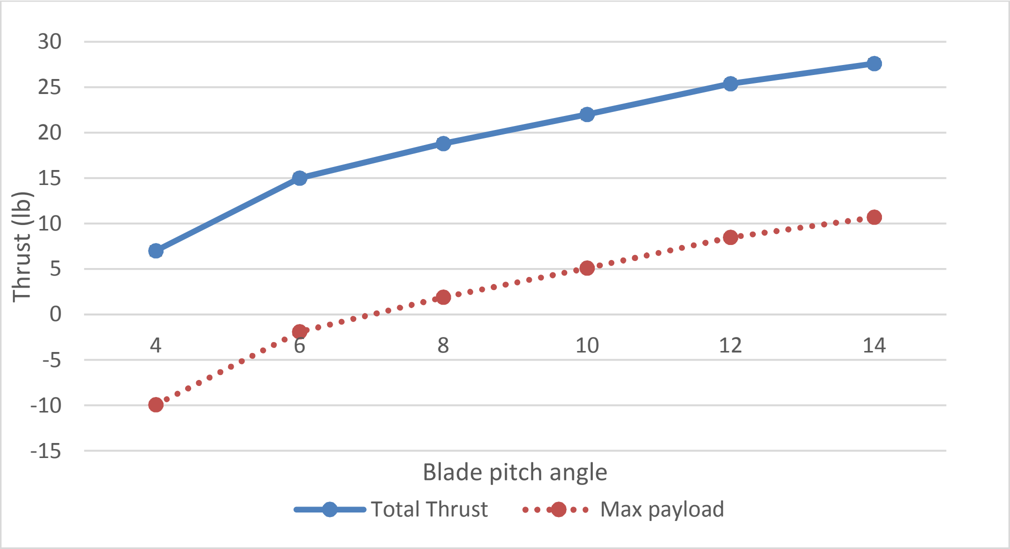

Figure 6. 18: The solid line represents the total thrust generated by the quadcopter, and the dash line represents the extra lift produced by the quadcopter.

The maximum payload of the quadcopter was calculated by using total thrust of the quadcopter at a particular blade pitch angle subtracted the weight of the vehicle, which was 16.9 lbs. This gave the extra lift produced by the quadcopter. As noted in Figure 6.18, there were some negative values for the payload at the pitch angle of 4 degrees and 6 degrees. This means that the quadcopter did not have enough thrust to lift off its own weight. Based on the maximum payload curve, the payload was zero at near 7 degrees of the blade pitch angle. This points to the fact that the quadcopter could lift its own weight at 7 degrees of the blade pitch angle. The highest total thrust was recorded at 14 degree of the blade pitch angle. The total thrust was about 27.6 lbs. The maximum payload was equal to 10.7 lbs. The test was not able to continue due to number 2 rotor arm shaft failure at 14 degree blade pitch angle. The steel rod on the carbon fiber arm shaft was debonded from the carbon fiber tube due to the torsional load on the arm shaft. This caused rotor number 2 disengage from the gearbox and stop rotating. Figure 6.19 shows the power consumption rate of the quadcopter at different blade pitch angles. The quadcopter left off at 7 degrees of the blade pitch angle, which was about 900 watts of power consumption for hovering. The maximum power consumption rate was at 14 degrees of the blade pitch angle, which was about 1766 watts from the motor ESC data log.

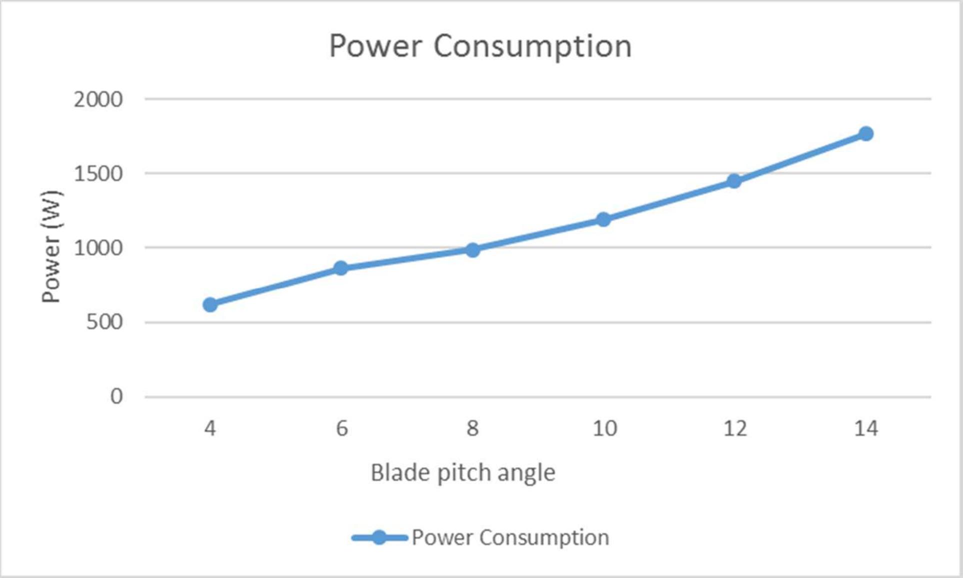

Figure 6. 19: The power consumption rate was recorded at different pitch angles

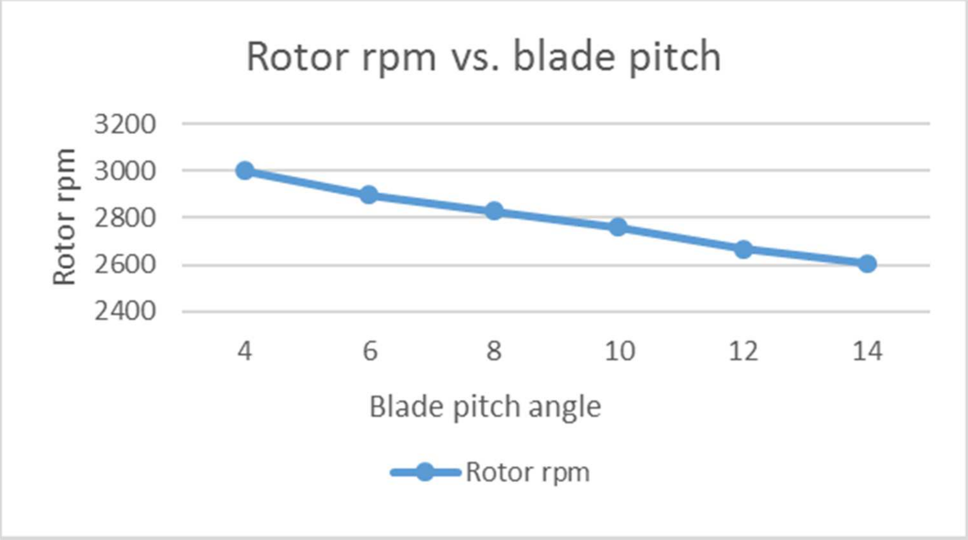

Figure 6. 20: The rotor rpm was recorded at different pitch angles

Figure 6.20 shows that the rotor rpm dropped when the blade pitch angle increased. This is a typical phenomenon happening with variable pitch rotorcrafts. Most of the RC helicopter could program the throttle channel so that when the blade pitch angle increased; the power of the motor also increased to compensate the drop of the rotor rpm. This test was aimed at finding out the necessary information about the maximal thrust and power limit on the vehicle; therefore, the power setting on the motor fixed at the maximum level. So when pitch increased, there was no room left for the further increase of the rotor rpm. Based on the graph, it is possible to say that the hovering rpm was about 2850, and that the lowest rpm was about 2600 at 14 degrees of blade pitch angle. The pervious test showed the quadcopter hovering at 9 degree of blade pitch angle with 2600 rotor rpm and power consumption which was about 988 watts. After new shafts, new rotor shaft bearings were installed on the quadcopter during this test. The quadcopter was able to hover at 7 degrees of the blade pitch angle with 2850 rpm, and its power consumption was about 900 watts. So by installing the new shafts and bearings on the quadcopter allowed us to improve the overall efficiency of the power transmission system.

6.5 Endurance Test on Quadcopter Power Transmission System

This test was designed to check the reliability and durability of the quadcopter power transmission system. The quadcopter was tethered to the ground and hovering as long as the battery could supply. The on-board battery for this quadcopter could provide about 15 minutes of the flight time. Figure 6.21 shows the quadcopter at hovering.

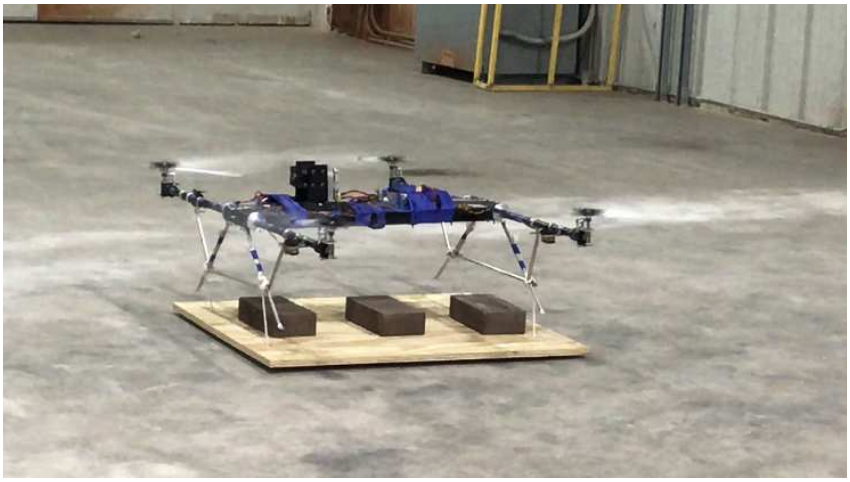

Figure 6. 21: The endurance test setup for the quadcopter

Test Results

The quadcopter was able to stay hovering for 9 minutes and 30 seconds. The quadcopter was hovering fairly stably during the first two minutes of the test. Then one side of the rotors occasionally showed a sudden drop of a lift and caused the whole quadcopter to jitter. This jittering motion became more frequent about half way of the testing. After about 2/3 of the test, this jittering motion became so violent that quadcopter could not stable itself during the hover. At the end of the test, one rotor's rpm dropped so much that it could not generate enough lift to stay in the hovering position; so the testing was stopped. Figures 6.22a and 22b show the front and back gearboxes after the testing.

(a) (b)

Figure 6. 22a and 6.22b: (a) The front gearbox shows excessive teeth wear after the test. (b) The back gearbox shows the excessive teeth wear on the bevel gear after the test.

Both gearboxes showed an excessive teeth wear on the bevel gears. A considerable amount of material has been removed from the bevel gear teeth and deposited onto the bottom of the gearbox. This became the cause of the quadcopter jittering motion. When the teeth started to wear down on the bevel gears, this caused the arm shaft bevel gear teeth skipping from the main shaft bevel gear. This created a different rpm between the main shaft bevel gear and arm shaft bevel gear, which caused a sudden drop of the rotor rpm and the jittering motion on the quadcopter. The gearbox has only one bearing for supporting the bevel gear of the arm shaft. Every bearing allowed a little misalignment for the shaft due to the tolerance of the bearing. When three bevel gears meshed together in the gearbox, this little misalignment of the bearing quickly was transferred to the arm shaft bevel gear and turned into vibration, which caused an excessive teeth wear on the bevel gears. Figure 6.23 shows that the rotor shaft bevel gears did have some teeth wear on the surface, but the condition was much better than the gearbox bevel gears.

Figure 6. 23: A moderate bevel gear teeth wear on the rotor shaft bevel gears

6.6 Evaluate the Vehicle Performance

The vehicle performance is estimated, based on the fuel version of this kind of quadcopters. According to the power consumption rate at the maximum thrust of the quadcopter, a gas-powered engine can be selected to replace the current electric motor with the same hp rating. Table 6.1 shows the weight breakdown of the current electric powered quadcopter, and table 6.2 indicates the weight breakdown of the fuel version quadcopter.

Table 6. 1: Weight break down for the electric powered quadcopter

Electric Quadcoper Weight				
Motor + motor mount	1154	g	2.54457	lbs
Batteries	1641	g	3.618405	lbs
Quadcopter body weight	4699	g	10.3613	lbs
ESC	134	g	0.29547	lbs
BEC	70	g	0.15435	lbs
total	7698	g	16.97409	lbs

Table 6. 2: Weight break down for the fuel version of the quadcopter

Fuel Version Quadcopter				
NITRO STAR F4.6 ENGINE	600	g	1.323	lbs
Speed reduction gearbox	300	g	0.6615	lbs
battery for servos	150	g	0.33075	lbs
quadcopter body weight	4699	g	10.3613	lbs
BEC	70	g	0.15435	lbs
total weight without fuel	5819	g	12.8309	lbs

A Nitro Star F4.6 engine is selected to replace the electric motor in the current quadcopter. This engine has a very high rpm; thus, a speed reduction gearbox is required to transfer the power from the engine to the main shaft. The large Lipo batteries for powering the motor are removed from the quadcopter, but a small-sized Lipo battery is still needed for powering all the servos in the fuel version quadcopter. Everything else will stay the same; thus, the total weight of the fuel versions of the quadcopter is about 12.8 lbs without having fuel on board. The Nitro Star F4.6 specifications are shown in figure 6.24.

Technical specifications:

1. Glow Plug: Cold R5 (HPI #1504)
2. Displacement: 4.6cc
3. Bore: 18.68mm
4. Stroke: 16.6mm
5. Power: 2.9hp @ 32,000RPM
6. Carburettor: F1-7.5 (Composite 7.5mm)

Figure 6. 24: Nitro Star F4.6 engine is selected for replacing the electric motor on the quadcopter [44]

The maximum of the thrust produced by the quadcopter is about 27.6 lbs. The weight of the fuel version quadcopter is about 12.8 lbs without fuel. The power consumption at the maximum thrust is about 1766 watts or 2.37 hp. This Nitro engine has 2.9 hp, based on the manufacturer specification. To be safe, take 85% for the real output power, which is about 2.46 hp. This is still more than enough to power this quadcopter to the maximum thrust. The fuel consumption rate of this engine is about 0.5 oz/min. This number is based on the O.S. ENGINE fuel consumption rate data sheet. The quadcopter is not controllable when it reveals its maximum thrust. So to be safe, the design payload should be 8 lbs, which is about 9 degrees of blade pitch to lift off. The maximum thrust is at 14 degree of pitch. This gives about 5 degrees of reserved blade pitch angle for maneuvers. By converting 8 lbs of payload to Nitro fuel, this quadcopter could have about 4 hours of flight time. Table 6.3 shows the estimated endurance time on the fuel version quadcopter.

Table 6. 3: Estimated endurance time based on 8 lbs of payload

Max thrust	27.6	lbs	
Power required	2.4	hp	
Power of Nitro enigne	2.9	hp	
Max lifting capability	14.76911	lbs	
Safe flight payload	8	lbs	
Nitro fuel density	1.1371	g/cm^3	
8 lbs Nitro fuel in volume	3191.188	cm^3	107.9 oz
Fuel consumption rate	0.5	oz/min	
Total flight time	215.81	minutes	3.59 hours

Maximum Rate of Climb and Forward Flight Speed

The maximum rate of climb and forward flight speed can be calculated based on the maximum thrust of the quadcopter, the total weight of the quadcopter, and the basic geometry of the quadcopter. The equations shown below were developed by Kalus & Lita [45] for predicting the maximum forward speed and climb rate of the quadcopter. The equations are being tested with the real performance data of some of the quadcopters presented on the market, and the results show some realistic numbers.

$$V_{hor} = \sqrt[4]{1 - 1/TR^2}\sqrt{2\frac{mg}{\rho c_D A}} * TR \qquad (6.5.1)$$

$$V_{ver} = \sqrt{2\frac{mg}{\rho c_D A}} * \sqrt{(TR-1)} \quad (6.5.2)$$

$$A = \frac{1}{2}MTM^2 + 3 * \pi r_p^2 \quad (6.5.3),$$

where

V_{hor} is the maximum forward flight speed (m/s),

V_{ver} is the maximum climb rate (m/s),

TR is the thrust over weight ratio $TR = T/(m * g)$. m is the mass of the quadcopter, g is the gravity,

ρ is the density of air (kg/m^3) ,

C_D is the drag coefficient of the quadcopter,

A is the effective area of the quadcopter (m^2),

MTM is the motor to motor distance, and

r_p is the radius of the propeller (m)

Figure 6.25 shows the maximum climb rate vs. payload on the electric powered quadcopter and gas-powered quadcopter. Figure 6.26 shows the maximum forward speed vs. payload on the electric powered quadcopter and gas-powered quadcopter. When calculating the thrust to weight ratio, the thrust should be based on 85% of the maximum thrust. This is because the quadcopter cannot fly at its maximum thrust, there must be some reserve of the thrust left for controlling the quadcopter during the flight. The gas-powered quadcopter is assumed to have 2 lbs of fuel on board. The climb rate and forward flight speed curves can be easily shifted up or down for the gas-powered quadcopter by changing the fuel weight on the quadcopter. Besides, the climb rate and forward flight speed increase during the flight of the gas-powered quadcopter due to the fuel weight which gradually decreases over time.

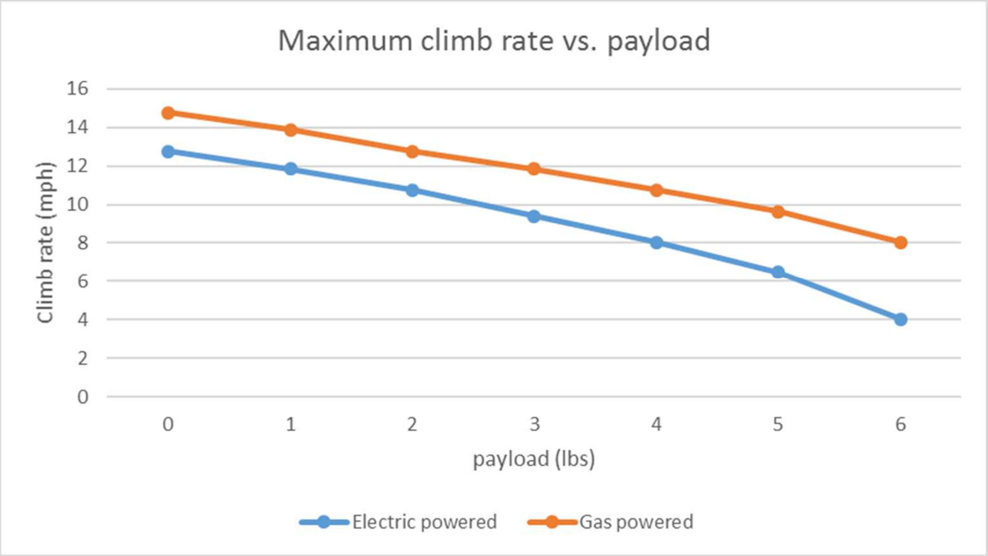

Figure 6. 25: Maximum climb rate decrease as payload increase

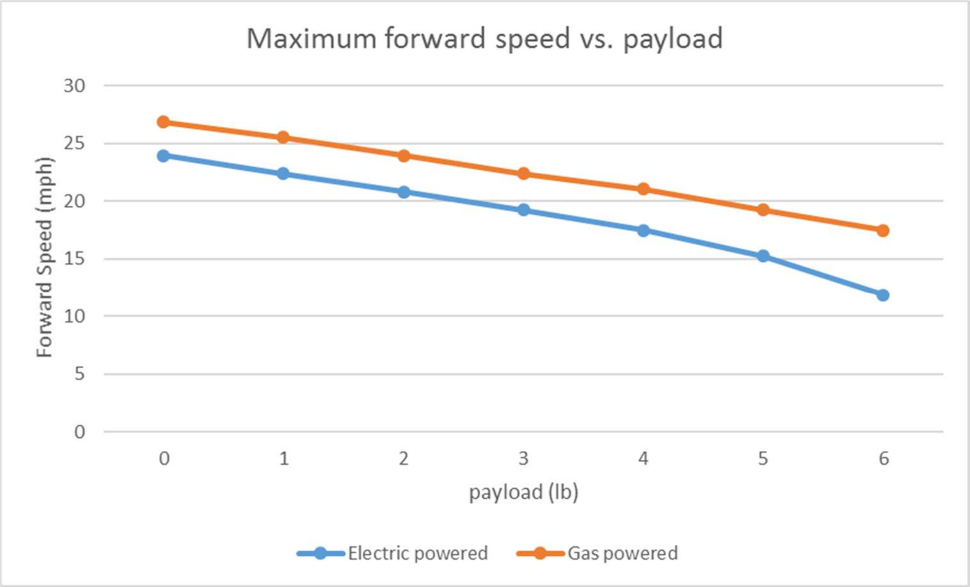

Figure 6. 26: Maximum forward speed of the quadcopter decreases as payload increases

CHAPTER VII

CONCLUSION & FUTURE WORK

Conclusion

The quadcopter has quickly gained interest in recent years and began to be vastly used in many applications such as aerial photography, land mapping and recreation, etc. However, most of the quadcopters are powered by four electric motors with four fixed pitch propellers, and they have a very limited flight time and payload capacity. Thus, the applications of the quadcopter are very limited. So the goal of this research project was to design and develop a variable-pitch quadcopter with single power plant for a long endurance flight and overcoming the limitations of the fixed-pitch quadcopter. The Qprop program was used for predicating the thrust and power consumption created by the rotor blades at different rpm and blade pitch angles. An electric motor was selected as the power plant of the variable pitch quadcopter based on the Qprop analysis.

Two types of the power transmission system were developed and tested. The first type of the power transmission system uses the gear-driven system extending from the motor to the main shaft. The second type is using the belt-driven system extending from the motor to the main shaft. Both types of the power transmission system use the main shaft to power two gearboxes which power the four variable pitch rotors.

A detailed stress analysis of the structural components and drivetrain system was conducted to ensure that the quadcopter can stand the maximum load from the rotors. A number of tethered flight tests and improvements were done on the quadcopter to ensure that all the mechanisms are working properly. The thrust vs. pitch testing was done on this quadcopter to determine the vehicle performance, based on the electric version of the quadcopter and fuel version of the quadcopter.

The final endurance test of the quadcopter was done for determining the reliability and durability of the power transmission system in the quadcopter.

Future Work

In the future, it is planned to replace all bevel gears in the gearbox with steel alloy bevel gears. The current design is using brass bevel gears; they are relatively soft and weak, compared to the steel alloy bevel gears. Each carbon fiber arm shaft requires two bearing carriers to secure the shaft from vibration for 100%. The current design is only having one bearing carrier for each carbon fiber arm shaft. One bearing carrier helps reduce the shaft vibration, but two will reduce the shaft vibration to minimum. Using additional bearing support for the gearbox will help reduce the bevel gear vibrations. The current gearbox design only has one bearing for supporting the bevel gear from the arm shaft. Every bearing allows a little misalignment for the shaft due to the tolerance of the bearing. Using additional bearing to support the bevel gear on the arm shaft will eliminate misalignment and reduce the gear vibration to minimum. This will make the power transmission system very robust. Implementing a flight controller into the quadcopter can be useful for increasing the degree of its stability and controlling the vehicle. It is also planned to transfer then to using a gas-powered engine and to test the performance of the vehicle again after making all these changes.

REFERENCES

[1] Global Upcoming Drone Applications. (2016, May 25). Retrieved January 27, 2018, from http://www.droneomega.com/drone-applications/

[2] Hottman, S. B., Hansen, K. R., & Berry, M. (2009). Literature review on detect, sense, and avoid technology for unmanned aircraft systems.

[3] Cutler, M., & How, J. (2012, August). Actuator constrained trajectory generation and control for variable-pitch quadrotors. In AIAA Guidance, Navigation, and Control Conference (p. 4777).

[4] Sheng, S., & Sun, C. (2016). Control and optimization of a variable-pitch quadrotor with minimum power consumption. Energies, 9(4), 232.

[5] Cutler, M., & How, J. P. (2015). Analysis and control of a variable-pitch quadrotor for agile flight. *Journal of Dynamic Systems, Measurement, and Control*, *137*(10), 101002.

[6] Cutler, M. J. (2012). *Design and control of an autonomous variable-pitch quadrotor helicopter* (Doctoral dissertation, Massachusetts Institute of Technology, Department of Aeronautics and Astronautics).

[7] Pretorius, A., & Boje, E. (2014). Design and modelling of a quadrotor helicopter with variable pitch rotors for aggressive manoeuvres. *IFAC Proceedings Volumes*, *47*(3), 12208-12213.

[8] Niermeyer, A., Gadekar, R., Duhoon, A., Kothari, M., Kadukar, S., Rane, L., & Suryavanshi, G. (2017). Design, development, and closed-loop flight-testing of single power plant variable pitch quadrotor unmanned air vehicle. ResearchGate

[9] Pang, T., Peng, K., Lin, F., & Chen, B. M. (2016, June). Towards long-endurance flight: Design and implementation of a variable-pitch gasoline-engine quadrotor. In *Control and Automation (ICCA), 2016 12th IEEE International Conference on* (pp. 767-772). IEEE.

[10] Radio Control Planes, Drones, Cars, FPV, Quadcopters and more. Retrieved January 27, 2018, from https://hobbyking.com/en_us/?

[11] G. d'Ambrosio and R. Navoni. Hg3 willy [video]. July 2011. (http://youtu. be/M4uXmekZk-4).

[12] Norouzi Ghazbi, S., Aghli, Y., Alimohammadi, M., & Akbari, A. A. (2016). QUADROTORS UNMANNED AERIAL VEHICLES: A REVIEW. *International Journal on Smart Sensing & Intelligent Systems*, *9*(1).

[13] DJI Phantom. Retrieved from https://www.dji.com

[14] History of Quadcopters and Multirotors. (n.d.). Retrieved February 27, 2018, from http://www.krossblade.com/history-of-quadcopters-and-multirotors/

[15] Roberto Navoni on August 28, 2010 at 2:08pm View Blog. (n.d.). HG3 the era of quad variable pitch has begun! Retrieved February 27, 2018, from https://diydrones.com/profiles/blogs/hg3-the-era-of-quad-variable

[16] Silas Van Natter on May 2, 2014 at 1:00pm View Blog. (n.d.). Gas Powered Single Engine Variable Pitch Quadcopter. Retrieved February 27, 2018, from https://diydrones.com/profiles/blogs/gas-powered-single-engine-variable-pitch-quadcopter

[17] S. W. (n.d.). Quadrotor System Modeling - Non-linear Equations of Motion. Retrieved February 27, 2018, from https://www.wilselby.com/research/arducopter/modeling/

[18] Daugherty, J., Strickland, C., & Burnap, A. (2014). *Gas-Powered Multi-Copter Final Report*. Oklahoma State University.

[19] Radio Control Planes, Drones, Cars, FPV, Quadcopters and more. (n.d.). Retrieved January 27, 2018, from https://hobbyking.com/en_us/?

[20] Adair, S., Grundamnn, R., Lan, J., & Lai, H. K. (2013). *MAE 4344 Muliti-Copter Design Final Report*. Oklahoma State University.

[21] Pfeifer Industries timing belts and timing belt pulleys. Retrieved February 28, 2018, from http://www.pfeiferindustries.com/

[22] HPC, E. (n.d.). Retrieved February 28, 2018, from http://www.hzpt.com/tech/fixshaft.htm

[23] Drela, M. Qprop User Guide. Retrieved March 02, 2018, from http://web.mit.edu/drela/Public/web/qprop/

[24] Liller, W. R. (2015). *The design of small propellers operating at low Reynolds numbers and associated experimental evaluation* (Doctoral dissertation).

[25] Hacker Motor USA brushless motors. Retrieved March 02, 2018, from https://hackermotorusa.com/

[26] I., J., & M. (2013, November 04). Brushless motor calculation. Retrieved March 02, 2018, from https://forum.openrov.com/t/brushless-motor-calculation/613

[27] Mechanical Properties of Carbon Fibre Composite Materials, Fibre / Epoxy resin . Retrieved March02, 2018, from http://www.performance-composites.com/carbonfibre/mechanicalproperties_2.asp

[28] Flight Mechanics of a Rotorcraft. (2011, June 12). Retrieved March 02, 2018, from http://rtime.felk.cvut.cz/helicopter/flight_mechanics_of_a_rotorcraft

[29] Bevel Gear. Retrieved March 02, 2018, from https://www.servocity.com/

[30] Belt Length Calculator | Distance Between Pulleys Calculator. Retrieved March 02, 2018, from https://sudenga.com/practical-applications/figuring-belt-lengths-and-distance-between-pulleys

[31] Deflection of Beams Study Notes for Mechanical Engineering. Retrieved March 02, 2018, from https://gradeup.co/deflection-of-beams-i-ae206f65-bea5-11e5-b01a-53c804be557a

[32] Budynas, R. G. (2016). *Shigley´s mechanical engineering design*. McGrae Hill.

[33] Keys, C., Kinkler, W., & Santiago, A. Composite Driveshaft.

[34] Schmid, S. R., Hamrock, B. J., & Jacobson, B. O. (2014). *Fundamentals of machine elements: SI version*. CRC Press.

[35] Design Aspects of Spur Gear. Retrieved March 02, 2018, from http://www.nptel.ac.in/

[36] Overload Factor. (2006, December 13). Retrieved March 02, 2018, from http://www.gearcalc.com/downloads/manual/manualse60.html

[37] Rolling bearings catalogue. Retrieved Mach 02, 2018, from

http://www.skf.com/binary/77-121486/SKF-rolling-bearings-catalogue.pdf

[38] Synchronous Timing Belts and Cables for Power Transmission Applications. Retrieved from http://www.sdp-si.com/products/Timing-Belts-and-Cables/index.php

[39] AT-Series Polyurethane Timing Belts - BRECOflex CO., LLC. (n.d.). Retrieved from https://www.brecoflex.com/products/timing-belts/at-series/

[40] McMaster-Carr. Retrieved from https://www.mcmaster.com/

[41] CopterControl/CC3D. Retrieved from

http://opwiki.readthedocs.io/en/latest/user_manual/cc3d/cc3d.html

[42] http://hobbycool.com/skyrc-helicopter-optical-tachometer/

[43] http://lwmeasurements.com/product/lss-400-large-shipping-scale/

[44] http://www.hpiracing.com/en/part/111595

APPENDICES

Qprop analysis on thrust, torque and power curve at 1000 rpm, 1500 rpm, 2000 rpm, 2500 rpm and 3000 rpm.

For rotor speed at 1000 rpm

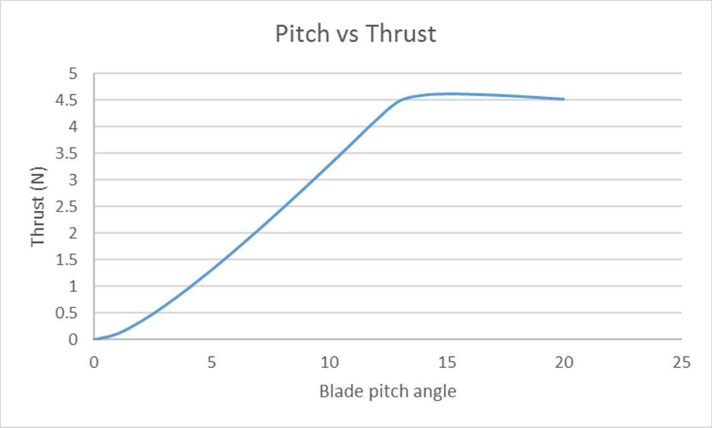

Figure 7. 1: Pitch angles vs. thrust at 1000 rpm by Qprop

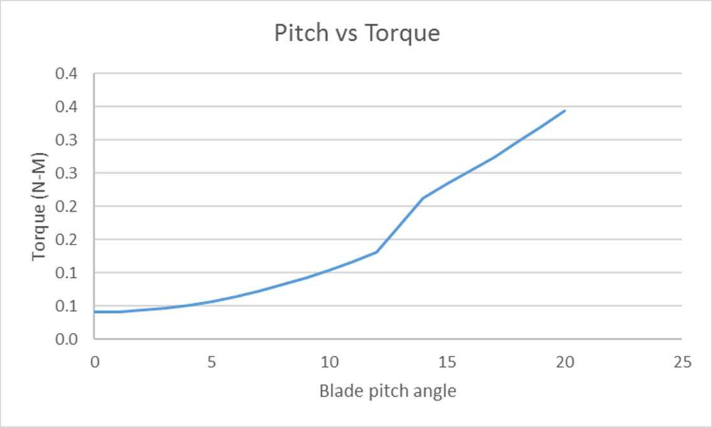

Figure 7. 2: Pitch angle vs. toruqe at 1000 rpm by Qprop

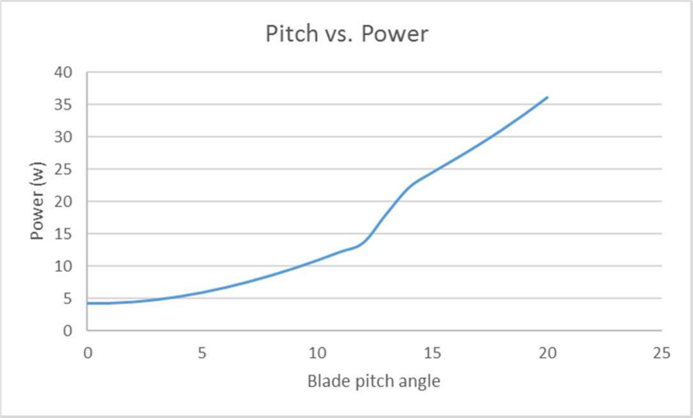

Figure 7. 3: Pitch angles vs power consumption at 1000 rpm by Qprop

For r otor speed at 1500 rpm

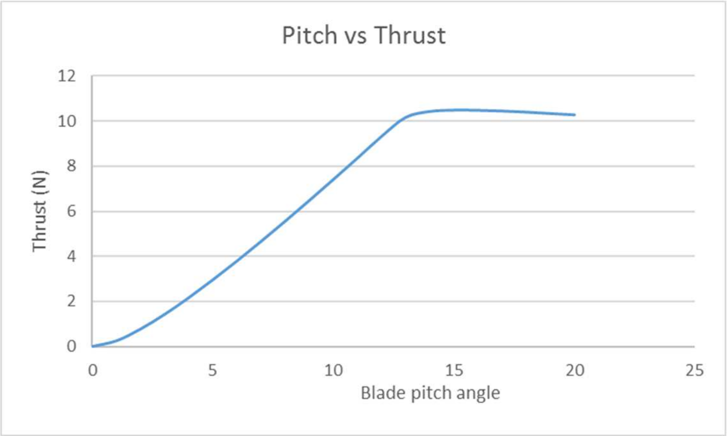

Figure 7. 4: Pitch angles vs. thrust at 1500 rpm by Qprop

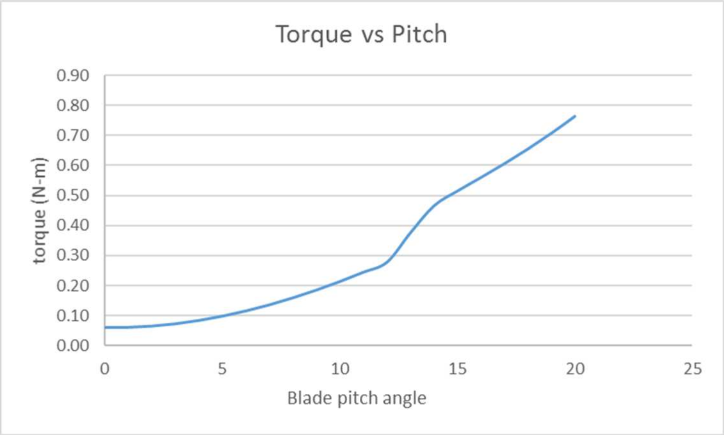

Figure 7. 5: Pitch angle vs. toruqe at 1500 rpm by Qprop

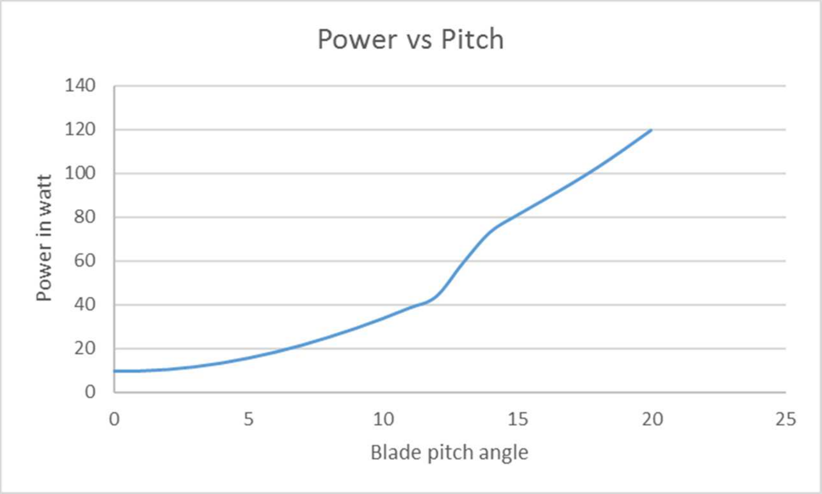

Figure 7. 6: Pitch angles vs power consumption at 1500 rpm by Qprop

For rotor speed at 2000 rpm

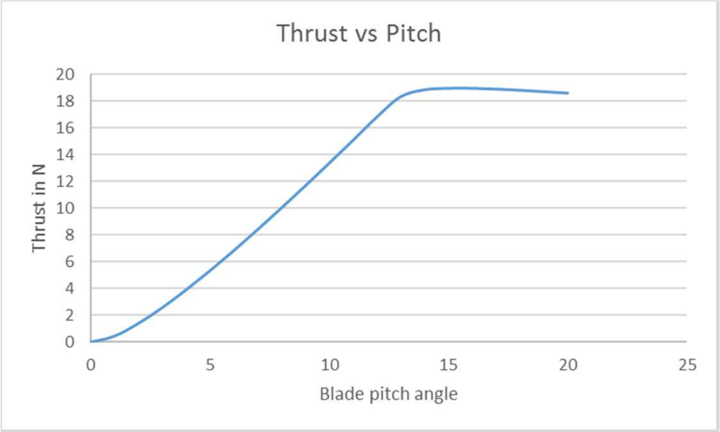

Figure 7. 7: Pitch angles vs. thrust at 2000 rpm by Qprop

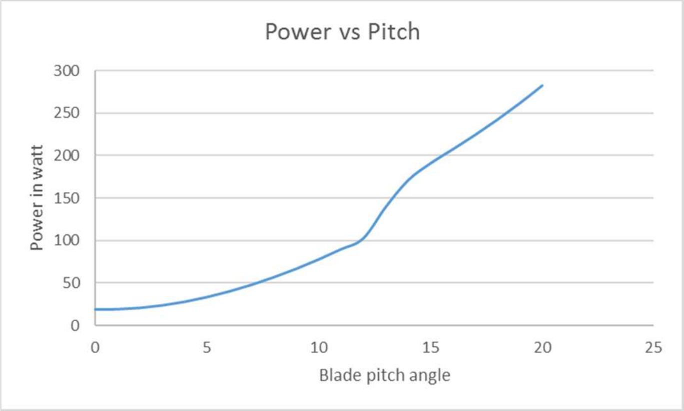

Figure 7. 8: Pitch angles vs power consumption at 2000 rpm by Qprop

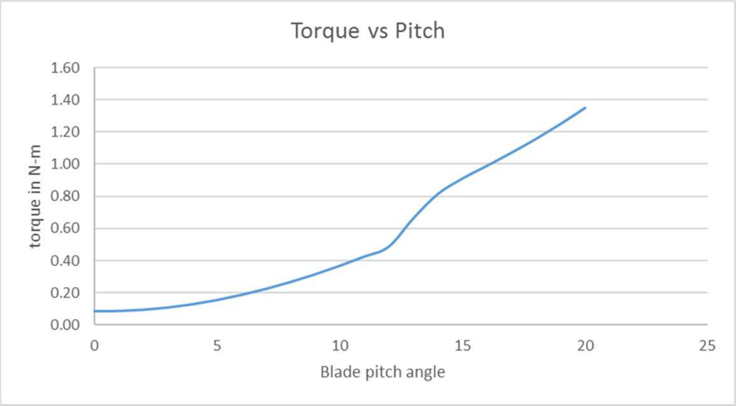

Figure 7. 9: Pitch angle vs. toruqe at 2000 rpm by Qprop

For rotor speed at 2500 rpm

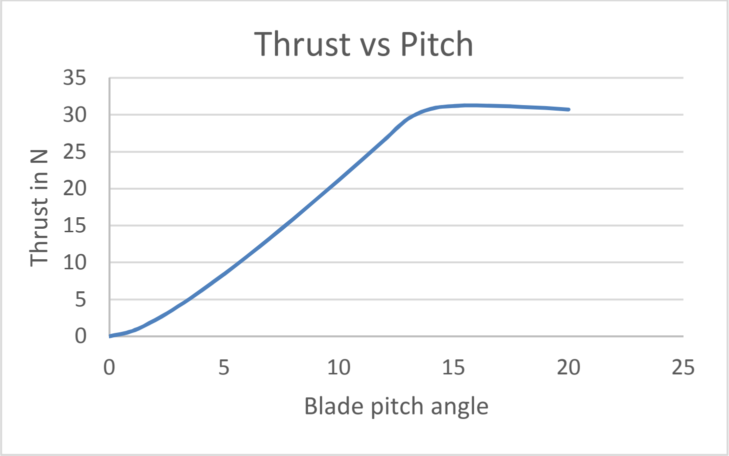

Figure 7. 10: Pitch angles vs. thrust at 2500 rpm by Qprop

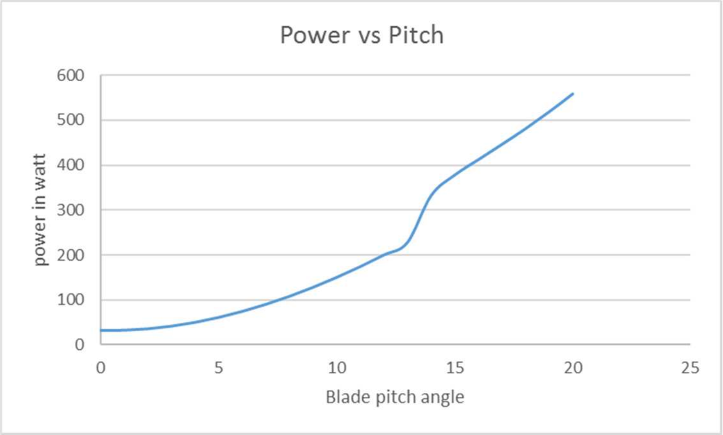

Figure 7. 11: Pitch angles vs power consumption at 2500 rpm by Qprop

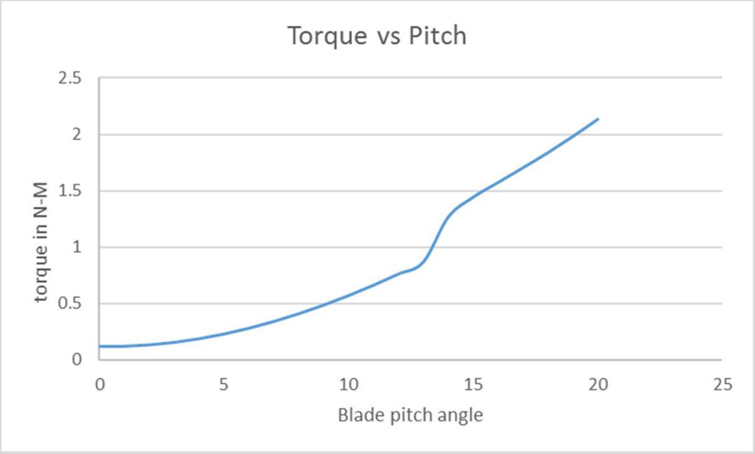

Figure 7. 12: Pitch angle vs. toruqe at 2500 rpm by Qprop

For rotor speed at 3000 rpm

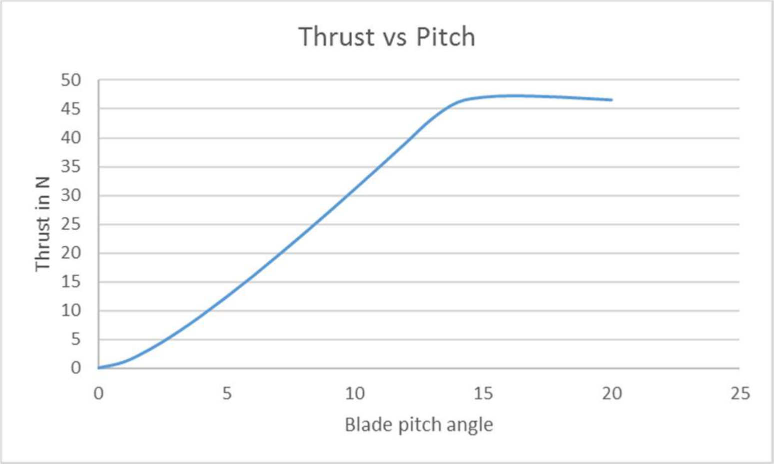

Figure 7. 13: Pitch angles vs. thrust at 3000 rpm by Qprop

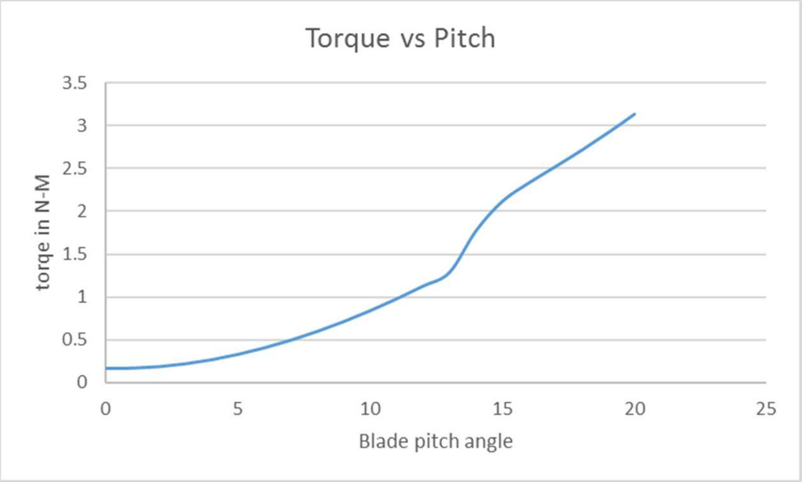

Figure 7. 14: Pitch angle vs. toruqe at 3000 rpm by Qprop

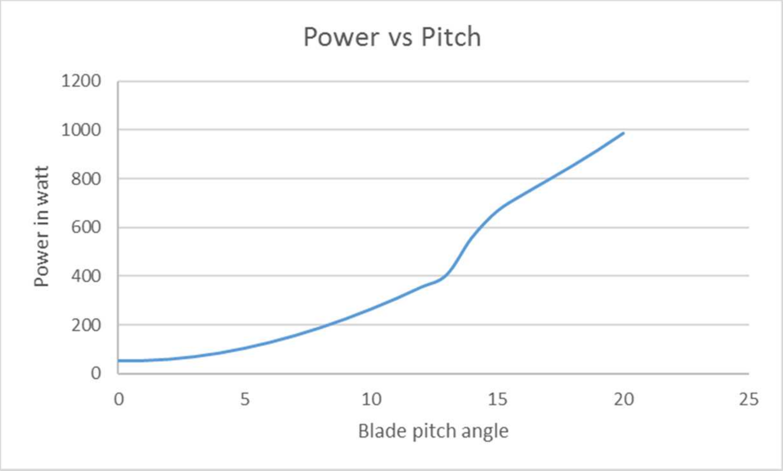

Figure 7. 15: Pitch angles vs power consumption at 3000 rpm by Qprop

The following graphs are based on the ESC data log from the actual thrust vs pitch tests. The graph shows the power consumption rate and rotor rpm at different blade pitch angles.

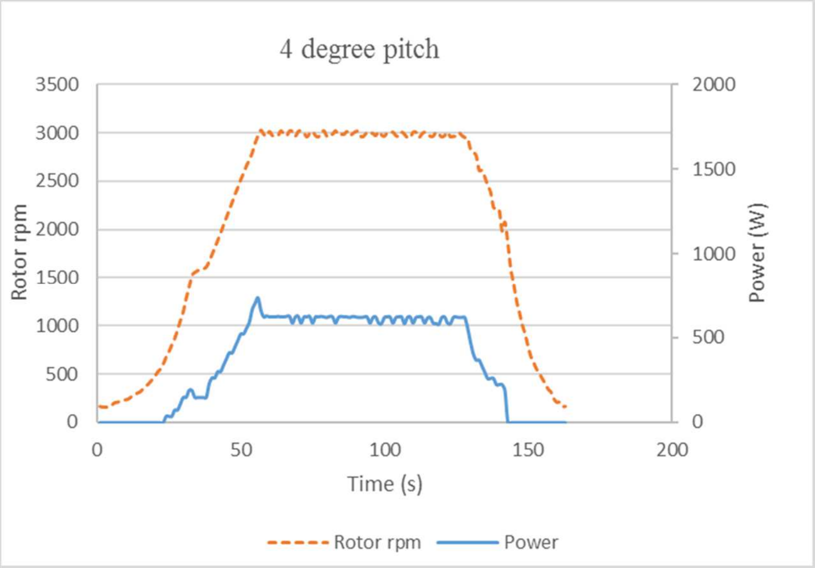

Figure 7. 16: Rotor speed vs. power consumption rate at 4 degree pitch

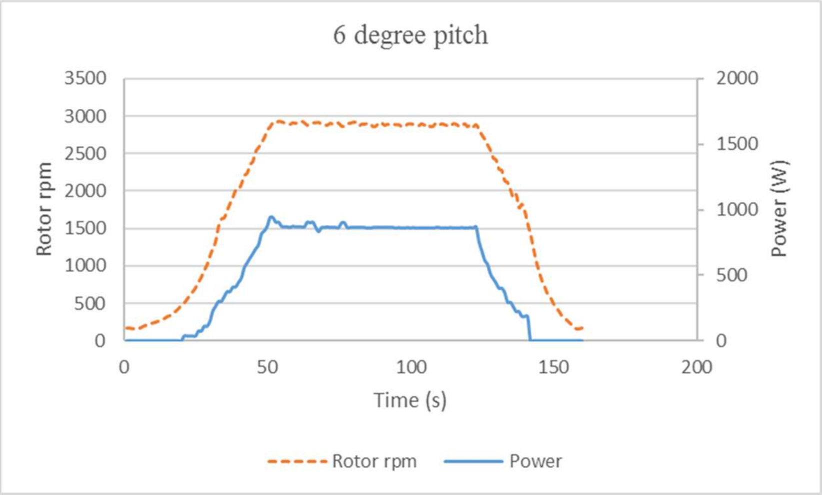

Figure 7. 17: Rotor speed vs. power consumption rate at 6 degree pitch

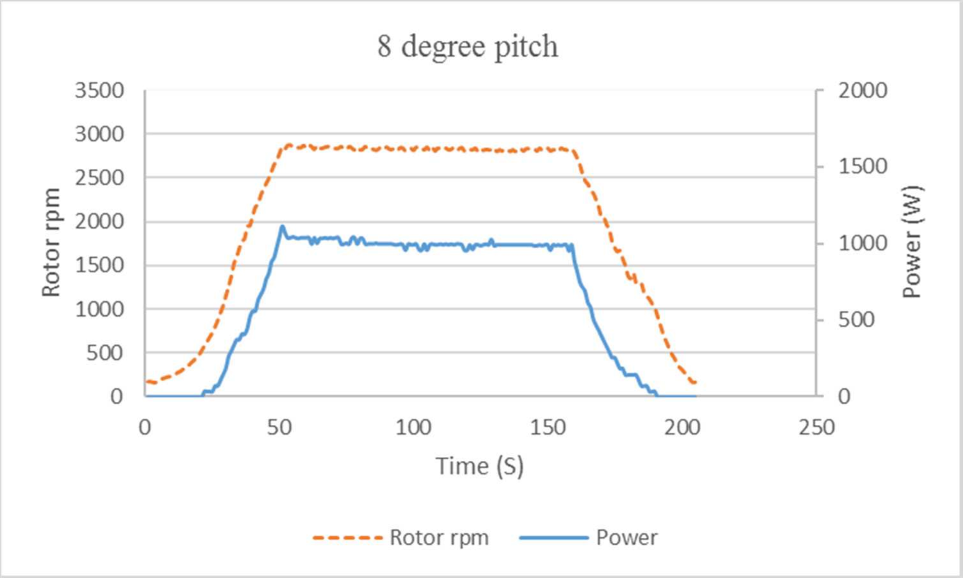

Figure 7. 18: Rotor speed vs. power consumption rate at 8 degree pitch

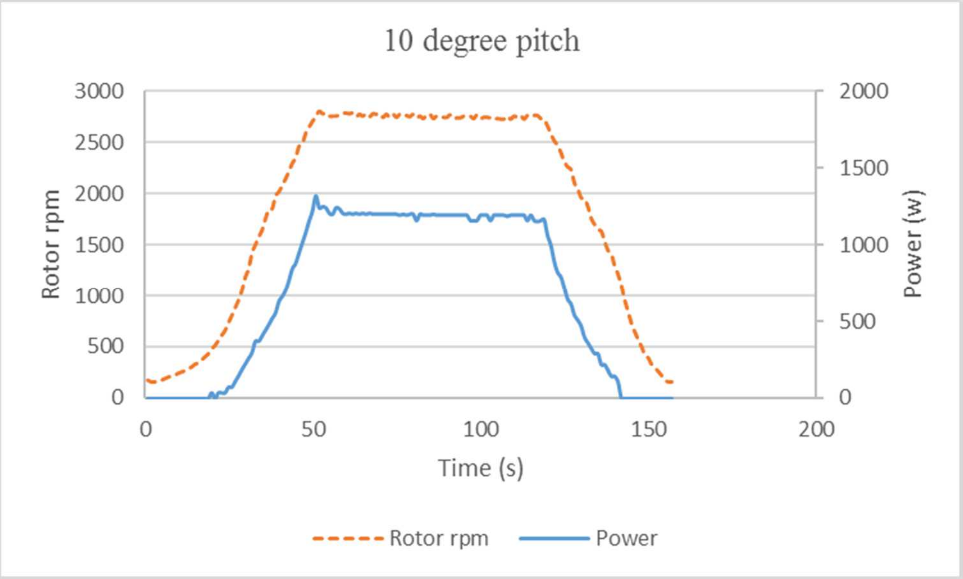

Figure 7. 19: Rotor speed vs. power consumption rate at 10 degree pitch

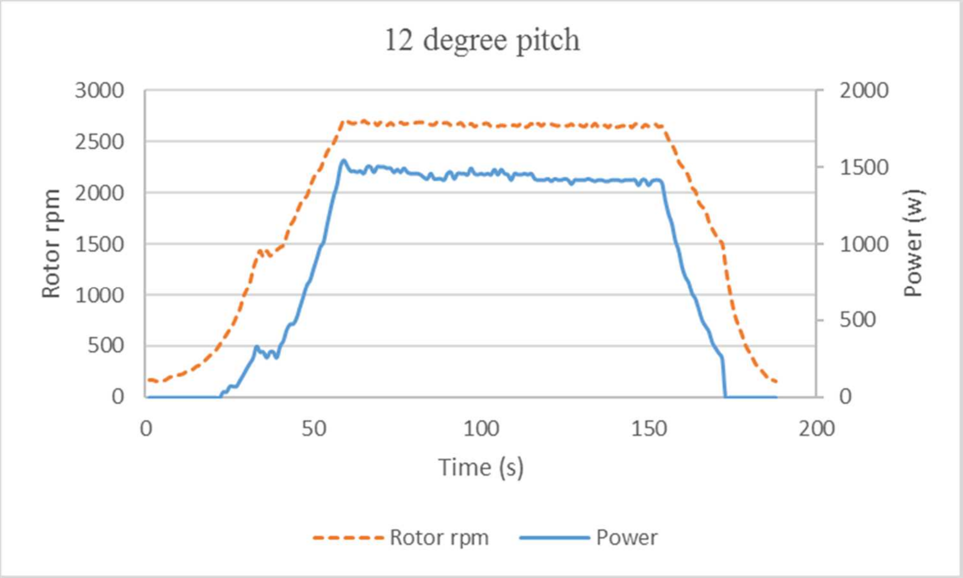

Figure 7. 20: Rotor speed vs. power consumption rate at 12 degree pitch

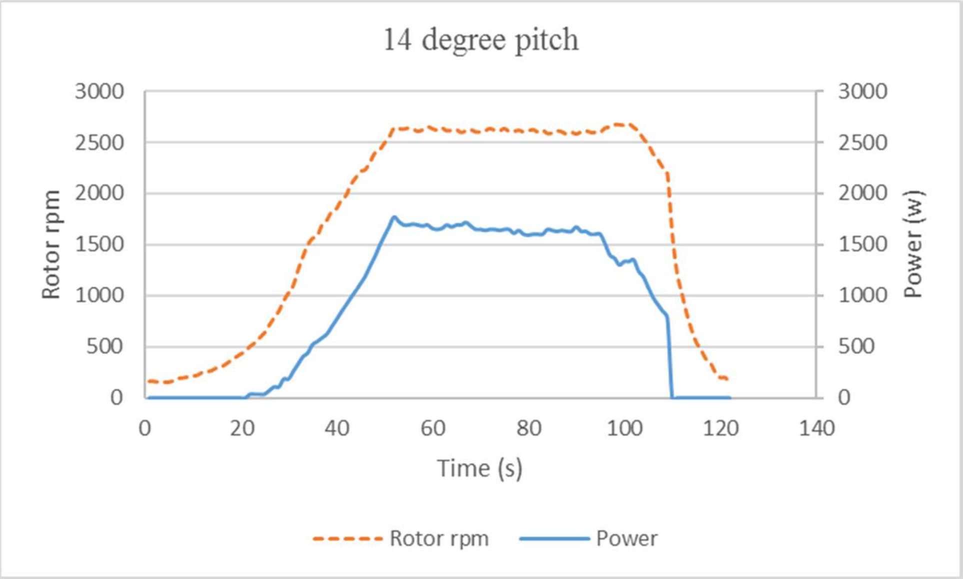

Figure 7. 21: Rotor speed vs. power consumption rate at 14 degree pitch

VITA

Xiaonan Wu

Candidate for the Degree of

Master of Science

Thesis: DESIGN AND DEVELOPMENT OF VARIABLE PITCH QUADCOPTER FOR LONG ENDURANCE FLIGHT

Major Field: Mechanical and Aerospace Engineering

Biographical:

Education:

Completed the requirements for the Master of Science in Mechanical and Aerospace Engineering at Oklahoma State University, Stillwater, Oklahoma in May, 2018

Completed the requirements for the Bachelor of Science in Aerospace Engineering at Oklahoma State University, Stillwater, Oklahoma in July, 2014